FLOW INDUCED POLYMER CHAIN EXTENSION AND ITS RELATION TO FIBROUS CRYSTALLIZATION

By M. R. MACKLEY and A. KELLER, F.R.S.
University of Bristol, H. H. Wills Physics Laboratory, Royal Fort, Tyndall Avenue, Bristol BS8 1TL, U.K.

(*Received* 4 *April* 1974)

[Plates 4–12]

CONTENTS

This work examines the effect that appreciable molecular extension has on the crystallization of long chain molecules. Elementary theoretical considerations presented indicate that to achieve high molecular extensions in solution a longitudinal velocity gradient of strain rate about $10^3\,s^{-1}$ is required. A method of generating such

a velocity gradient, involving flow between opposed jets, is reported and the nature of this flow pattern is examined and quantitatively analysed.

The behaviour of polyethylene–xylene solutions in the flow field is presented, notably birefringence observations and measurements indicate that a high degree of molecular alinement can be achieved in specific localized areas of the flow field; also concentration effects are observed which are discussed in terms of entanglement concepts. The effect chain alinement has on crystallization is examined in detail, in particular the 'shish kebab' morphology of the crystals so produced is examined in relation to the hydrodynamic conditions in which they were grown.

1. Introduction

The present work originates from the study of the crystallization of chain type macromolecules from solution. It was found that chain extension as induced by flow can have specific consequences on the crystallization behaviour of the macromolecules.

In quiescent conditions polyethylene in xylene crystallizes in the form of a suspension of thin lamellar platelets (figure 1, plate 4), which are of uniform thickness in the range 10–20 nm and contain the long molecules in a folded configuration (see Keller 1968, for a review). For crystallization of this type to take place within a permissible time, a supercooling of at least 20 °C is required. However, crystallization at lower supercoolings can be achieved by simply stirring the solution sufficiently vigorously to ensure that some form of turbulent flow is present. In this case a fibrous aggregate appears attached to the stirrer which has a predominance of high molecular mass material (Pennings & Kiel 1965). Closer examination by electron microscopy reveals a 'shish kebab' type structure (figure 2, plate 4) consisting essentially of a fine central thread of crystalline extended, or partially extended chain material onto which chain folded platelets are regularly attached as shown diagrammatically in figure 3.

Unfortunately the complexity of turbulent flow makes it difficult to establish exactly how the shish kebab (in particular the chain extended component) is formed.

The work of Pennings, van der Mark & Booij (1970), who used a simple Couette apparatus, led to the discovery that when flow between the inner rotating cylinder and the stationary outer cylinder was simple shear, fibrous nucleation could not be induced; however with the onset of 'Taylor Vortices' (Taylor 1934), fibrous crystallization did take place. Pennings *et al.* (1970) concluded that induction of fibrous crystallization was associated with the presence of chain extending longitudinal velocity gradients which were present between each counter-rotating vortex (shown in section in figure 4, plate 4), from experiments carried out in our laboratory.

Starting from this point, the work presented in § 2 of this paper sets out the theoretical criteria affecting chain extension of long molecules in both transverse and longitudinal velocity gradients. An experimental system for producing longitudinal velocity gradients of sufficient magnitude to theoretically extend chains fully is introduced in § 3 and examined in detail in § 5. The results observed for a polyethylene–xylene system are presented in §§ 4, 6 and 7. Finally in § 8 the fibrous crystal structures are examined in relation to the flow field in which they were produced.

2. On the flow induced elongation of macromolecules

(*a*) *On velocity gradients*

The special chain extending behaviour of longitudinal velocity gradients as opposed to transverse velocity gradients was indicated by Ziabicki (1959), Peterlin (1966), Pennings *et al.* (1970),

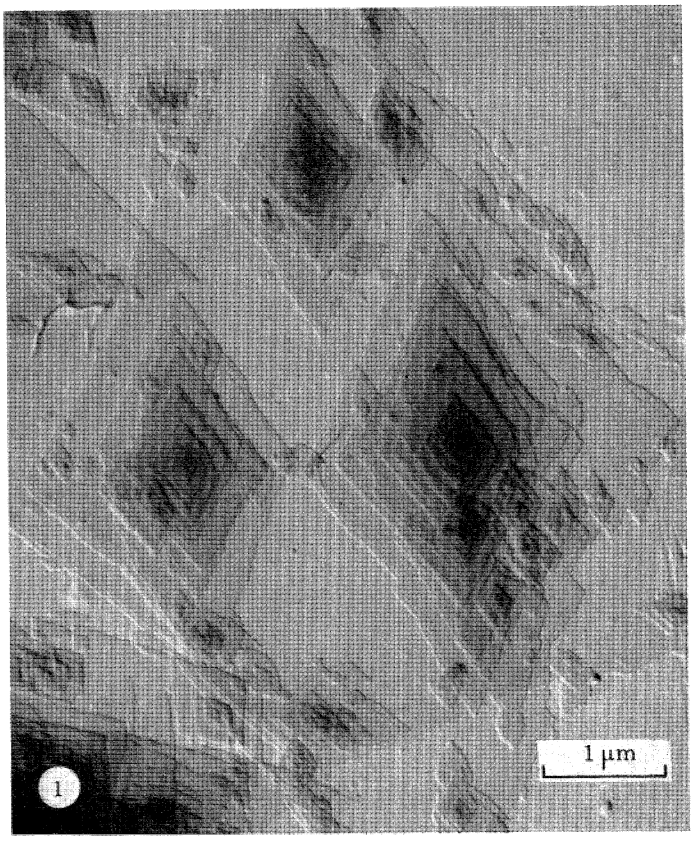

FIGURE 1. Typical chain folded crystal (Keller 1958).

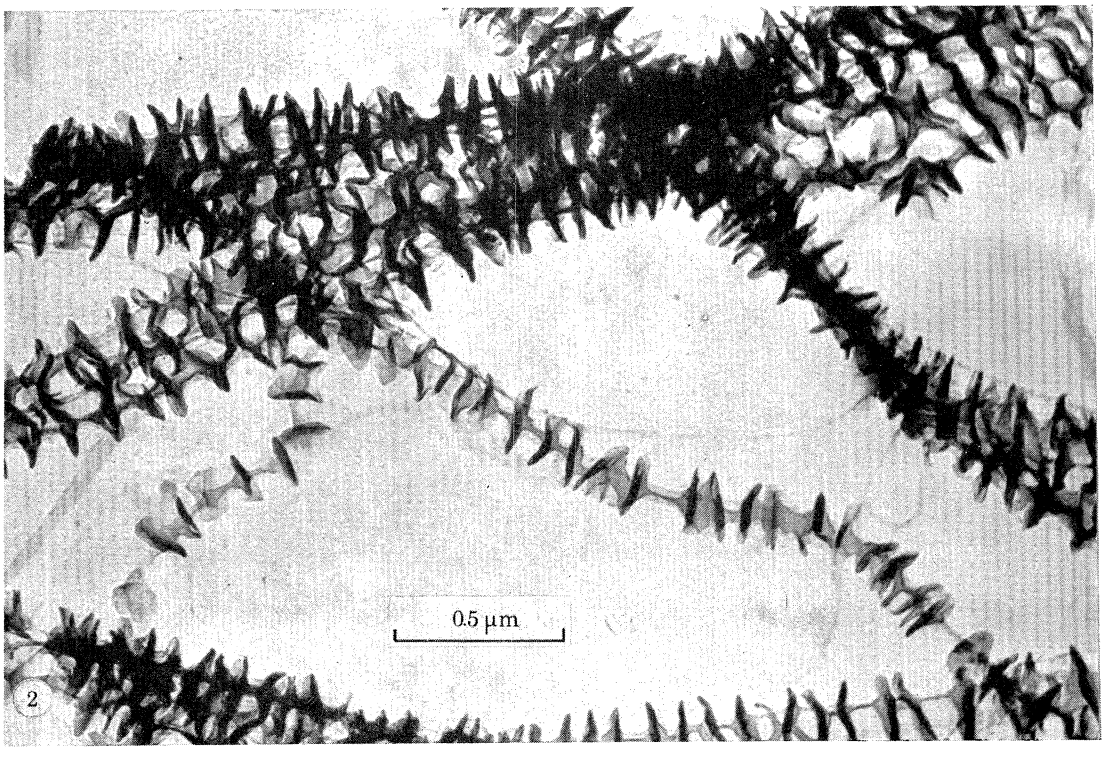

FIGURE 2. A standard shish kebab (after Pennings 1966).

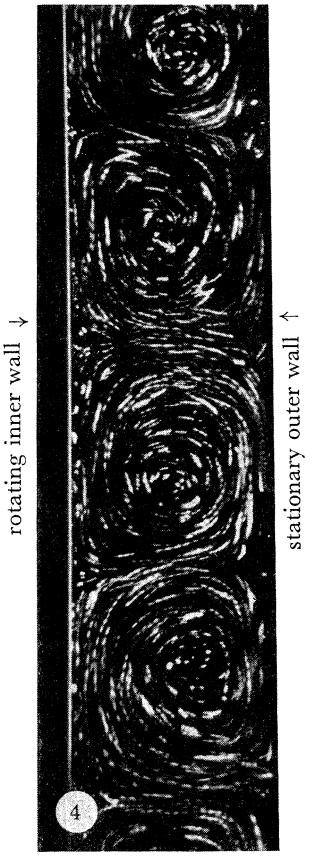

FIGURE 4. Sectional view of Taylor vortices illuminated by a planar radial light beam. (Gap between cylinders, 1 cm.)

(*Facing p.* 30)

Frank (1970) and briefly discussed in the preliminary publication (Frank, Keller & Mackley 1971).

As shown by Frank (1970) the velocity gradient $\dot{e}_{ij} = \partial V_j/\partial r_i$, where V is the velocity at position r, forms a tensor which may be separated into symmetric and antisymmetric parts

$$a_{ij} = \tfrac{1}{2}(\dot{e}_{ij} + \dot{e}_{ji}), \quad \omega_{ij} = \tfrac{1}{2}(\dot{e}_{ij} - \dot{e}_{ji})$$

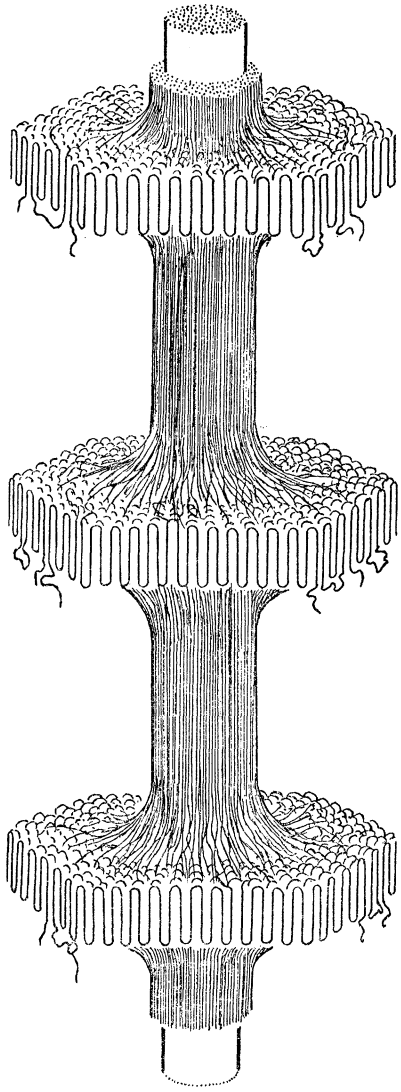

FIGURE 3. Model of shish kebab structure (after Pennings, van der Mark & Kiel (1970)).

thus $\dot{e}_{ij} = (a_{ij} + \omega_{ij})$. The symmetric part a_{ij} represents a strain rate and the antisymmetric ω_{ij} represents a rotation rate. Longitudinal velocity gradients, for example uniaxial extension contain only symmetric terms, hence $\omega_{ij} = 0$ and the flow is non-rotational. In contrast, for transverse velocity gradients ω_{ij} is non-zero. It is a consequence of this rotational element ω in the flow that prevents high molecular extensions in transverse velocity gradients.

(*b*) *Molecular theories*

(i) *Basic molecular concepts*

In formulating the problem molecules were assumed to be independent of one another. The introduction of entanglements to the analysis produces both physical and mathematical difficulties beyond the scope of this work. In some results to be given later the assumption of molecular independence is not strictly valid, however it was considered that at moderate concentrations (typically 1 %) these results were still meaningful.

An individual molecule can be conveniently characterized by its end-to-end vector $\boldsymbol{h}$, or in view of thermal motion, the root mean square of this quantity defined by $\langle h^2\rangle^{\frac{1}{2}}$. If h_0 refers to the r.m.s. value for the unperturbed state then molecular extension can be defined by

$$\epsilon = (\langle h^2\rangle^{\frac{1}{2}} - h_0)/h_0, \tag{2.1}$$

where h_0 can be expressed to varying approximations. We shall use one allowing for fixed C—C—C bond angle α (C ≡ carbon atom) but otherwise allowing unhindered rotation around C—C bonds. Then

$$h_0^2 = b^2 N \cot^2 \tfrac{1}{2}\alpha, \tag{2.2}$$

where N denotes the number of repeat units and b the bond length. The fully extended chain length is $h_{\text{ext}} = Nb\cos\frac{1}{2}\alpha$ which defines the maximum achievable extension $\epsilon_{\max} = N^{\frac{1}{2}}\sin\frac{1}{2}\alpha$. (For $N = 10^6$ and $\alpha = 70.5°$, $\epsilon_{\max} = 580$.) Considering the dumb-bell (or chain shot) model, the molecular interaction terms for the whole chain are replaced by two terms acting only at the ends of the molecule; a centre directed elastic force and a viscous frictional force. The entropic elastic force (Treloar 1949) may be given by $F_1 = -K\boldsymbol{h}$ where,

$$K = (3kT/Nb^2)\tan^2\tfrac{1}{2}\alpha, \tag{2.3}$$

where T is the temperature and k Boltzmann constant. The frictional term can be introduced as a diffusion constant D, or a friction coefficient term f: the two being related by $D = kT/f$. Assuming Stokes' equation the frictional force F_2 is given by $\boldsymbol{F}_2 = f\boldsymbol{u}$ where $\boldsymbol{u}$ is the average velocity. Two models to determine f are considered. In the 'free draining model' the viscous forces are assumed to act on the molecule leaving the solvent unaffected when moving through it. Assuming the molecule to be a series of beads connected by frictionless couplings the friction coefficient can be determined assuming the friction coefficient of one bead to be $6\pi\eta_0 r$ where r is one quarter the segment length and η_0 the solvent viscosity; then

$$f_{\text{f.d.}} = \tfrac{3}{2}\pi\eta_0 bN. \tag{2.4}$$

In the 'non-free draining' model it is assumed the solvent is trapped in the region of the molecule and dragged along with the same velocity as the molecule. This can be visualized by replacing the molecule by a sphere equal to h_0 and considering its frictional effect; then

$$f_{\text{n.f.d.}} = 6\pi\eta_0 b\cot\tfrac{1}{2}\alpha N^{\frac{1}{2}}. \tag{2.5}$$

The effect of the combined elastic and frictional forces can be visualized by stretching a single dumb-bell molecule, releasing it and following its subsequent behaviour. The extension at any time, t, will be governed by the force-equilibrium equation, where the frictional drag force is balanced by the elastic retraction. The extension at any subsequent time t is given by

$$\left.\begin{aligned} \epsilon &= \epsilon_0 \mathrm{e}^{-t/\tau}, \\ \tau &= f/k. \end{aligned}\right\} \tag{2.6}$$

where

Thus to a first approximation the extension will decay exponentially with a characteristic relaxation time τ.

(ii) *Chain extension in velocity gradients*

The analysis of Hermans (1944) and Peterlin (1967) for transverse velocity gradients and those of Ziabicki (1949) and Peterlin (1966) for longitudinal velocity gradients will be given in outline. Another theory although formulated in a different way leads essentially to similar results (Hlavacek & Seyer 1971).

By considering an ensemble of dumb-bell molecules and fixing one end of each molecule at the origin, the probability function $\psi(\boldsymbol{h})$ can be obtained for the other end. With no external hydrodynamic interaction, the equilibrium probability function of the chain end is obtained from the equation

$$-(K/f)\,\boldsymbol{h}\psi - D\,\mathrm{grad}\,\psi = 0. \tag{2.7}$$

The normalized solution is

$$\psi(\boldsymbol{h}) = \left(\frac{3}{2h_0^2\pi}\right)^{\frac{3}{2}} \exp - \left(\frac{3}{2h_0^2}h^2\right), \tag{2.8}$$

and $\langle h^2\rangle^{\frac{1}{2}} = h_0$. When considering a transverse velocity gradient of the form $V = \dot{\epsilon}(x_2, 0, 0)$ an additional term must be introduced into the equation to account for the external hydrodynamic velocity gradient

$$\mathrm{div}\,(V\psi - (K/f)\,\boldsymbol{h}\psi - D\,\mathrm{grad}\,\psi) = 0. \tag{2.9}$$

In writing this equation it is assumed the applied velocity gradient is unaffected by the presence of the molecules, which cannot strictly be true, although probably a reasonable approximation. The solution of the above equation for the transverse velocity gradient is

$$\psi(h) = \frac{(3/2\pi h_0^2)^{\frac{3}{2}}}{(1+\frac{1}{4}\beta^2)^{\frac{1}{2}}} \exp - \frac{(3/2h_0^2)}{(1+\frac{1}{4}\beta^2)}\left((1+\tfrac{1}{2}\beta^2)\,x_1^2 + x_2^2 + (1+\tfrac{1}{4}\beta^2)\,x_3^2\right), \tag{2.10}$$

where $\beta = \dot{\epsilon}\tau$ and $\tau = f/K$.

The second moment of the distribution function is given by

$$\langle h^2\rangle = \langle x_1^2 + x_2^2 + x_3^2\rangle = h_0^2(1+\tfrac{1}{6}\beta^2), \tag{2.11}$$

leading to ϵ_{T} the extension in a transverse velocity gradient;

$$\epsilon_{\mathrm{T}} = (1+\tfrac{1}{6}\beta^2)^{\frac{1}{2}} - 1. \tag{2.12}$$

In a similar way the molecular extension for uniaxial extension is obtained by substituting the velocity components

$$V = \dot{\epsilon}(x_1, -\tfrac{1}{2}x_2, -\tfrac{1}{2}x_3)$$

into the diffusion equation, giving

$$\langle h^2\rangle = h_0^2\left(\frac{(1+\frac{1}{2}\beta)}{(1-\beta)\,(1+\frac{1}{2}\beta)}\right),$$

$$\epsilon_{\mathrm{L}} = \left(\frac{2-\beta}{(1-\beta)\,(2+\beta)}\right)^{\frac{1}{2}} - 1. \tag{2.13}$$

The extensions for the two velocity gradients are plotted as a function of β in figure 5. The essential point is that for small β, the extension of the molecule for both velocity gradients is small and increases linearly with increasing $\ln\beta$ up to about $\beta = 10^{-1}$; then in the case of the longitudinal velocity gradient with increasing β the extension rapidly exceeds unity and becomes

infinite at $\beta = 1$. In the case of the transverse velocity gradient the average molecular extension increases only slowly and becomes infinite for $\beta = \infty$. In practice infinite extensions are impossible because the molecule is of finite length, the fully straightened chain is identified with infinity for the purpose of this analysis.

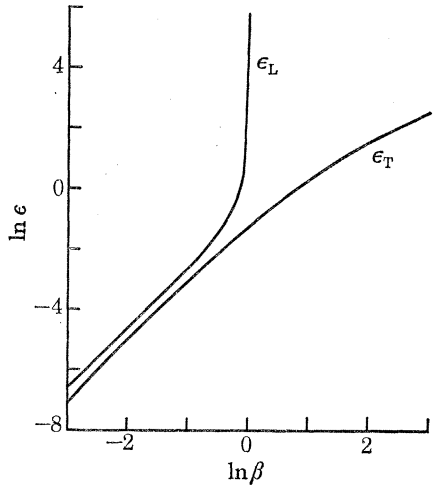

FIGURE 5. Graph of molecular extension plotted as a function of β where $\beta = \dot{\epsilon}\tau$.

The relaxation time given by $\tau = f/K$ for the two molecular models are given by combining equations (2.3), (2.4), (2.5), and (2.6).

Free draining

$$\tau_{\text{f.d.}} = \tfrac{1}{2}\pi \frac{\eta_0 b^3}{KT} \cot^2 \tfrac{1}{2}\alpha N^2. \tag{2.14}$$

Non-free draining

$$\tau_{\text{n.f.d.}} = \frac{2\pi\eta_0 b^3}{KT} \cot^{\frac{5}{2}} \tfrac{1}{2}\alpha N^{\frac{3}{2}}. \tag{2.15}$$

These are plotted as functions of molecular mass in figure 6 for the polyethylene–xylene system with parameters given by

$$\eta_0 = 0.5\,\text{mPa s}, \quad T = 400\,\text{K}, \quad b = 0.154\,\text{nm},$$

$$\cot^2 \tfrac{1}{2}\alpha = 2, \quad M = 14N, \quad k = 1.38 \times 10^{-23}\,\text{J/K}.$$

These two curves represent possible extreme values for the relaxation time. The geometric mean, τ_m, of these two curves is also plotted on figure 6 and will be used as a representative single value for τ for a given molecular mass.

The dependence of molecular extension on molecular mass becomes apparent on the substitution of τ_m into (2.13). The molecular extension predicted by the Peterlin equation for uniaxial extension is shown in figure 7.

Because the extension increases dramatically from a small value to infinity in the region $\dot{\epsilon}\tau = 1$, it is justifiable to say that for $\dot{\epsilon}\tau \geqslant 1$ the molecules are fully extended and when $\dot{\epsilon}\tau < 1$ the molecules are essentially unaffected by the velocity gradient. This can be related to a critical molecular mass M_c below which chain extension is negligible and above which it is complete. For polyethylene–xylene

$$M_c = (1.1 \times 10^{14}/\dot{\epsilon})^{\frac{4}{7}}.$$

For $\dot{e} = 1\,s^{-1}$, $M_c \approx 10^8$ which for a normal polyethylene would mean that only an infinitesimal fraction of the high molecular mass material would be extended. However for a strain rate of $10^3\,s^{-1}$, $M_c \approx 2.0 \times 10^6$; this would mean that a small but possibly significant proportion of the material would be fully alined for a typical polyethylene where $\bar{M}$ is in the region 10^5.

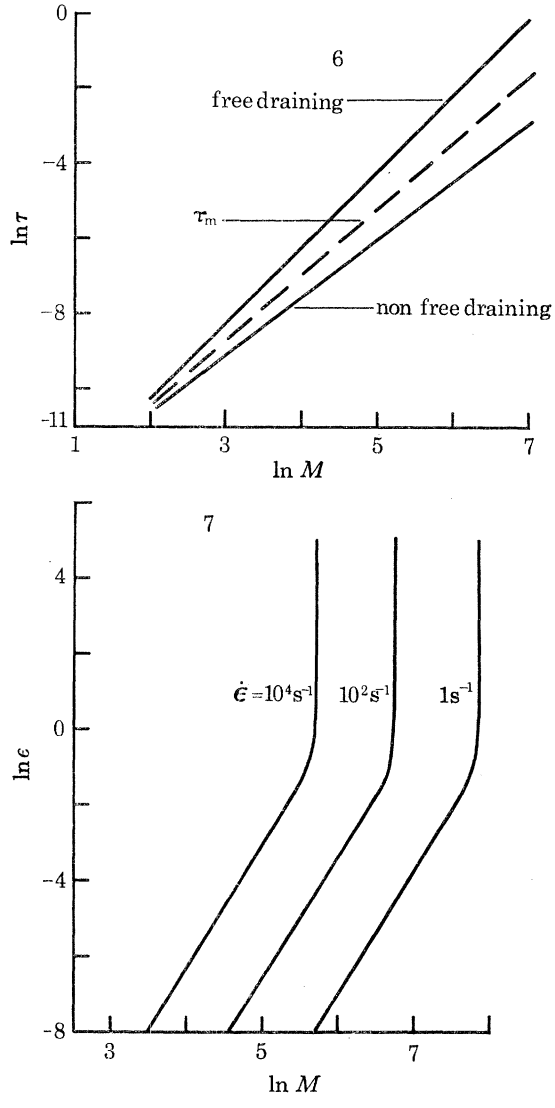

FIGURE 6. (Above,) Graph of relaxation time τ plotted as a function of molecular mass.
FIGURE 7. (Below) Graph of extension of molecule plotted as a function of molecular mass for three selected strain rates.

3. EXPERIMENTAL REALIZATION

(*a*) *Principles*

The most favourable conditions required to induce chain extension and hence presumably fibrous nucleation in a non-turbulent flow system can be summarized as follows. A flow field with a longitudinal velocity gradient is essential and the magnitude of the velocity gradient according to the previous analysis should not be less than about $10^3\,s^{-1}$. Further, the molecules

should remain in the elongational velocity field for as long a time as possible. Methods used in the past for generating longitudinal velocity gradients include Taylor vortices (Pennings *et al.* 1970), fibre spinning (Katayama, Amano & Nakamara 1968), axially oscillating plungers (McHugh & Schultz (1973), flow through sharp edge orifices and four-roll mills (Metzner & Metzner 1970).

It was first proposed by Frank *et al.* (1971) to use mutually opposed orifices (in this case jets) to generate longitudinal velocity gradients. The flow system, shown schematically in figure 8, must have a point of zero velocity at the centre of symmetry of the system. Thus for the case where fluid is forced out of the jets, fluid elements entering the system along the symmetry axis experience a longitudinal velocity gradient in the form of a uniaxial compression along and near the symmetry axis and symmetry plane of the system given by the strain rate tensor

$$\dot{\epsilon}_{ij} = \dot{\epsilon} \begin{bmatrix} -1 & 0 & 0 \\ 0 & \frac{1}{2} & 0 \\ 0 & 0 & \frac{1}{2} \end{bmatrix}.$$

For the reverse flow where fluid is sucked into the jets, fluid elements entering the system on the symmetry plane experience a longitudinal velocity gradient in the form of uniaxial extension on both the symmetry plane and the symmetry axis given by the strain rate tensor;

$$\dot{\epsilon}_{ij} = \dot{\epsilon} \begin{bmatrix} 1 & 0 & 0 \\ 0 & -\frac{1}{2} & 0 \\ 0 & 0 & -\frac{1}{2} \end{bmatrix}.$$

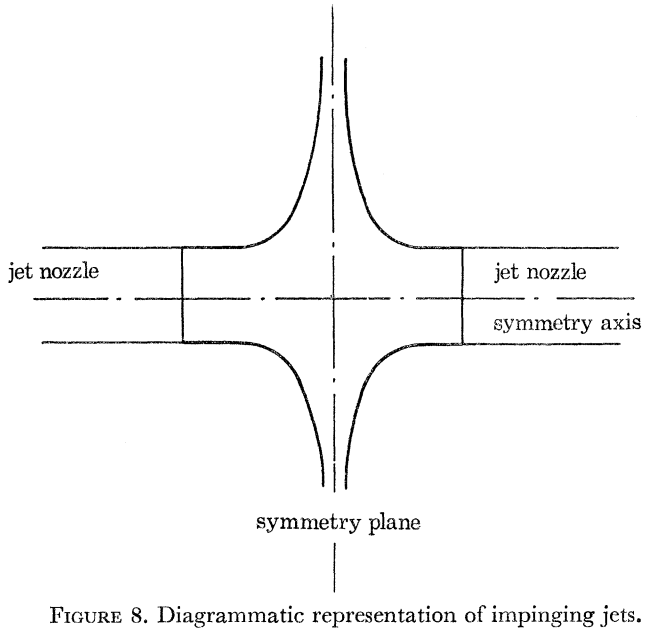

FIGURE 8. Diagrammatic representation of impinging jets.

It is not possible by symmetry arguments alone to express precisely the nature of the velocity gradient away from the symmetry axis and plane.

If the two jets have a velocity of V and a jet separation of d, the velocity along the axis falls from V to zero in a distance of $\frac{1}{2}d$, thus to a first approximation assuming the velocity change to be uniform, the velocity gradient along the axis will be $2V/d$. For a jet velocity of 1 m/s and a jet separation of 1 mm the longitudinal velocity gradient along the symmetry axis would be

$2 \times 10^3\ s^{-1}$. As there is a point of zero velocity at the centre of symmetry the time of passage of fluid elements along the symmetry plane and axis should in principle be infinite. This would optimize any chance of nucleation.

(*b*) *Apparatus*

Experiments embodying the principle of opposed jets were carried out with the apparatus described previously (Frank *et al.* 1971) and shown again in figure 9. The jets and reservoirs were immersed in polymer solution and the whole system maintained at any chosen temperature. Stainless steel hypodermic needles were used for the jets, typically of internal diameter 1 mm. By applying an excess pressure of nitrogen to the reservoir tubes polymer solution was forced out of the jets which could produce the impinging jet flow (blow case). The reverse flow, where

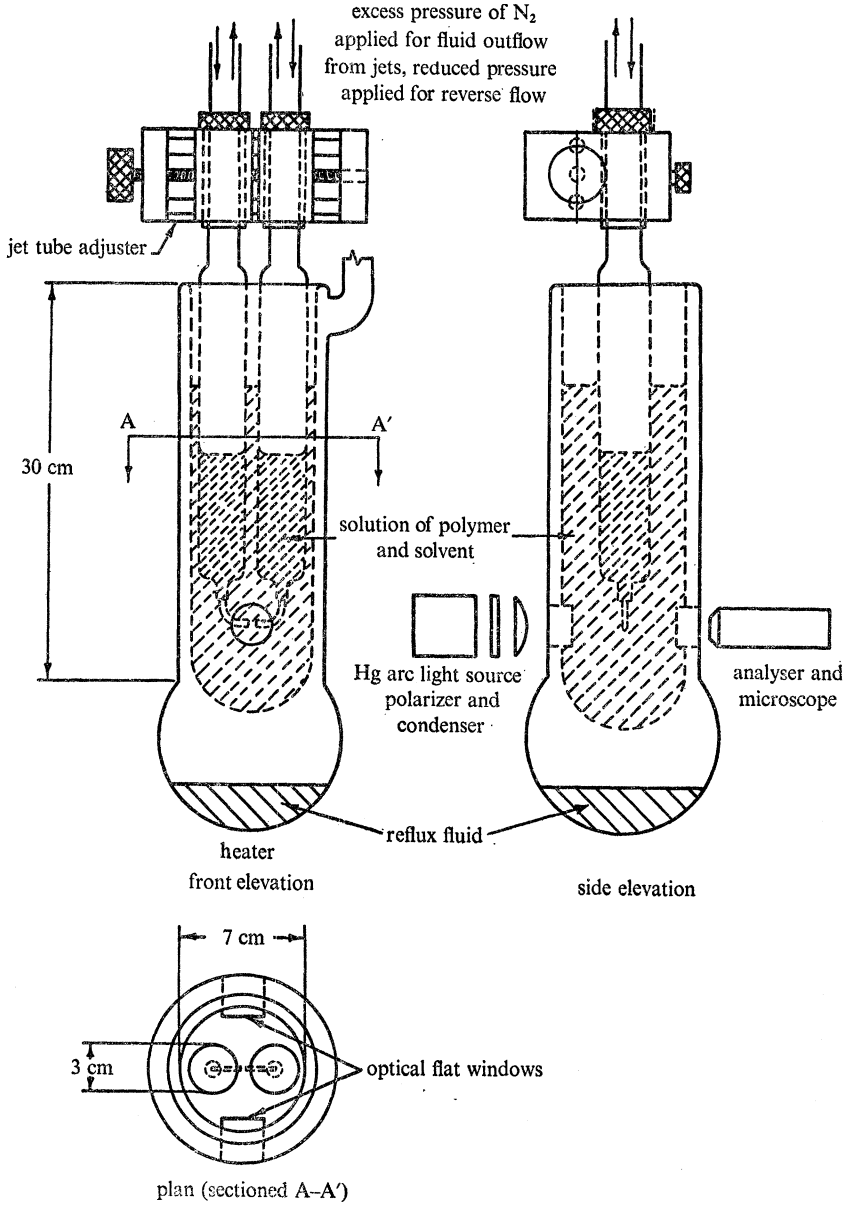

FIGURE 9. Diagram of essential features used in impinging jet experiment.

polymer was sucked into the jets could be achieved by applying a reduced pressure (suction case). The desired rate of flow for either direction could be conveniently obtained by controlling the pressure in the reservoirs. The magnitude of the jet velocity through the jets was obtained by observing the rate of movement of the solution in the reservoir, which could be related to the nozzle velocity. It was found that alinement of the jets was critical and suitable adjustors had to be incorporated into the design. Also a polarizing microscope was introduced into the system so that *in situ* observations could be made of the regions between the jets.

(*c*) *Materials*

High density polyethylene in xylene solution was used throughout. The polyethylene was of two kinds, Rigidex type 2 (Rt2) and Hostalen GUR. These corresponded to an average and to an exceptionally high molecular mass with respective mass average molecular masses of 2×10^5 and about 10^7. The difference in behaviour between these will serve to define the trend with changing molecular mass in §§ 6–8. In some cases a small amount of *N*-phenyl-2-naphthylamine was added to the solution to inhibit oxidative degradation.

4. Basic observations

Phenomena observed optically in the opposed jet region were (*a*) reversible, confined to the duration of flow and (*b*) irreversible, persisting after cessation of flow. These occurred respectively above and below a critical temperature $T_{c,\max}$. It has become clear that permanent crystallization is involved in the irreversible phenomenon.

(*a*) *Reversible birefringence*

The basic observation is a highly localized birefringence observed between the jets as shown in figures 10 and 11, plate 5, where the polaroids are crossed at 45° to the symmetry axis of the

---

Description of plate 5

Figures 10–13. Photographs illustrating localized birefringence observed for a 3 % Rt2 solution at 125 °C.

Figure 10. Suction with polars crossed at 45°.

Figure 11. Blowing with polars crossed at 45°.

Figure 12. Suction with polars crossed at 0° and 90°.

Figure 13. Blowing with polars crossed at 0° and 90°.

Figures 14–17. Oblique view observations of birefringence seen for a 3 % Rt2 solution at 125 °C.

Figure 14. Suction with polars crossed at 45°.

Figure 15. Blowing with polars crossed at 45°.

Figure 16. Suction bright field photograph.

Figure 17. Blowing bright field photograph.

Figures 18–23. The change in birefringence with vertical jet displacement.

Figure 18. Exact alinement: sucking.

Figure 19. Small vertical displacement: sucking.

Figure 20. Large vertical displacement: sucking.

Figure 21. Exact alinement: blowing.

Figure 22. Small vertical displacement: blowing.

Figure 23. Large vertical displacement: blowing.

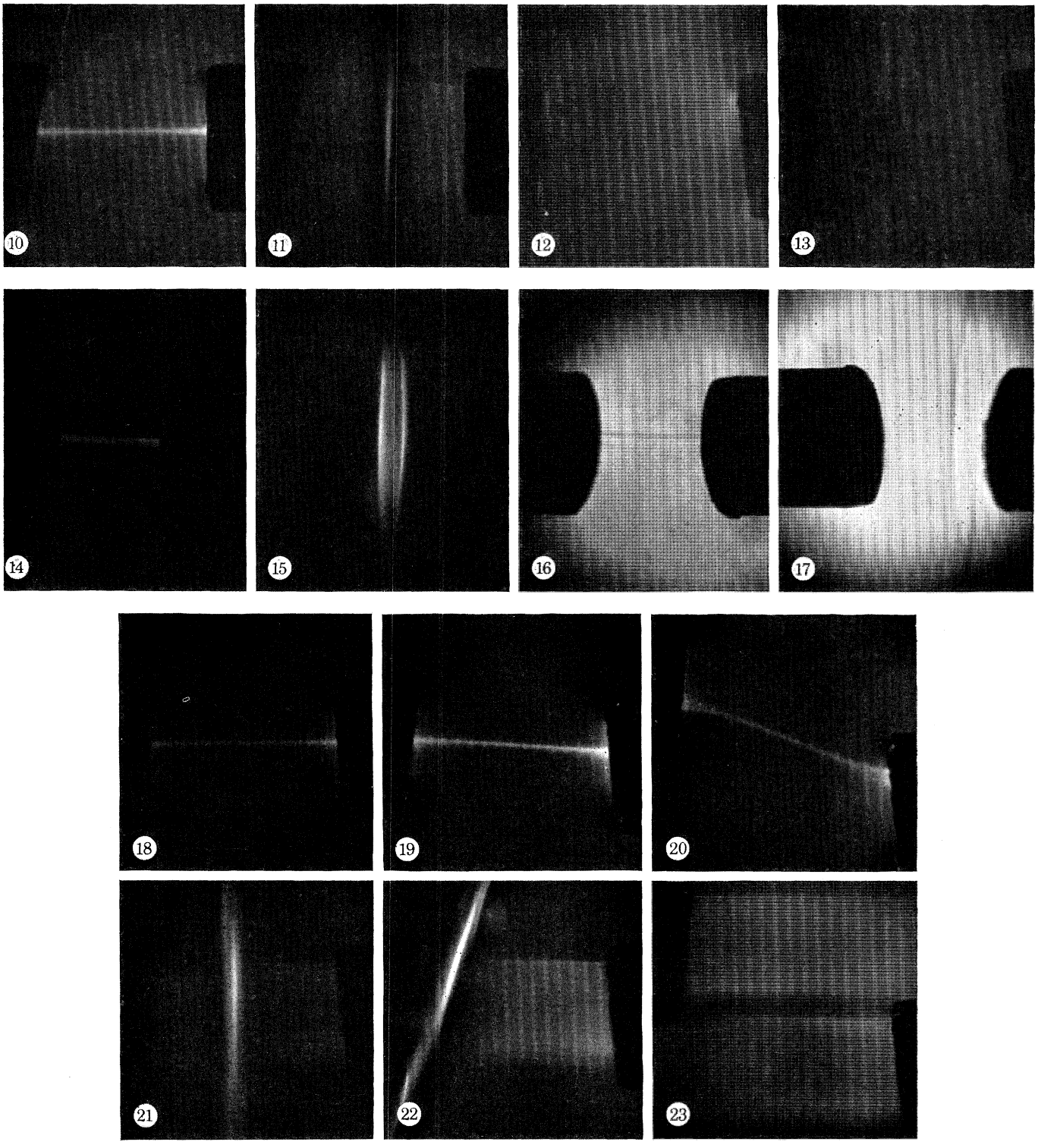

FIGURES 10–23. For description see opposite.

Facing p. 38)

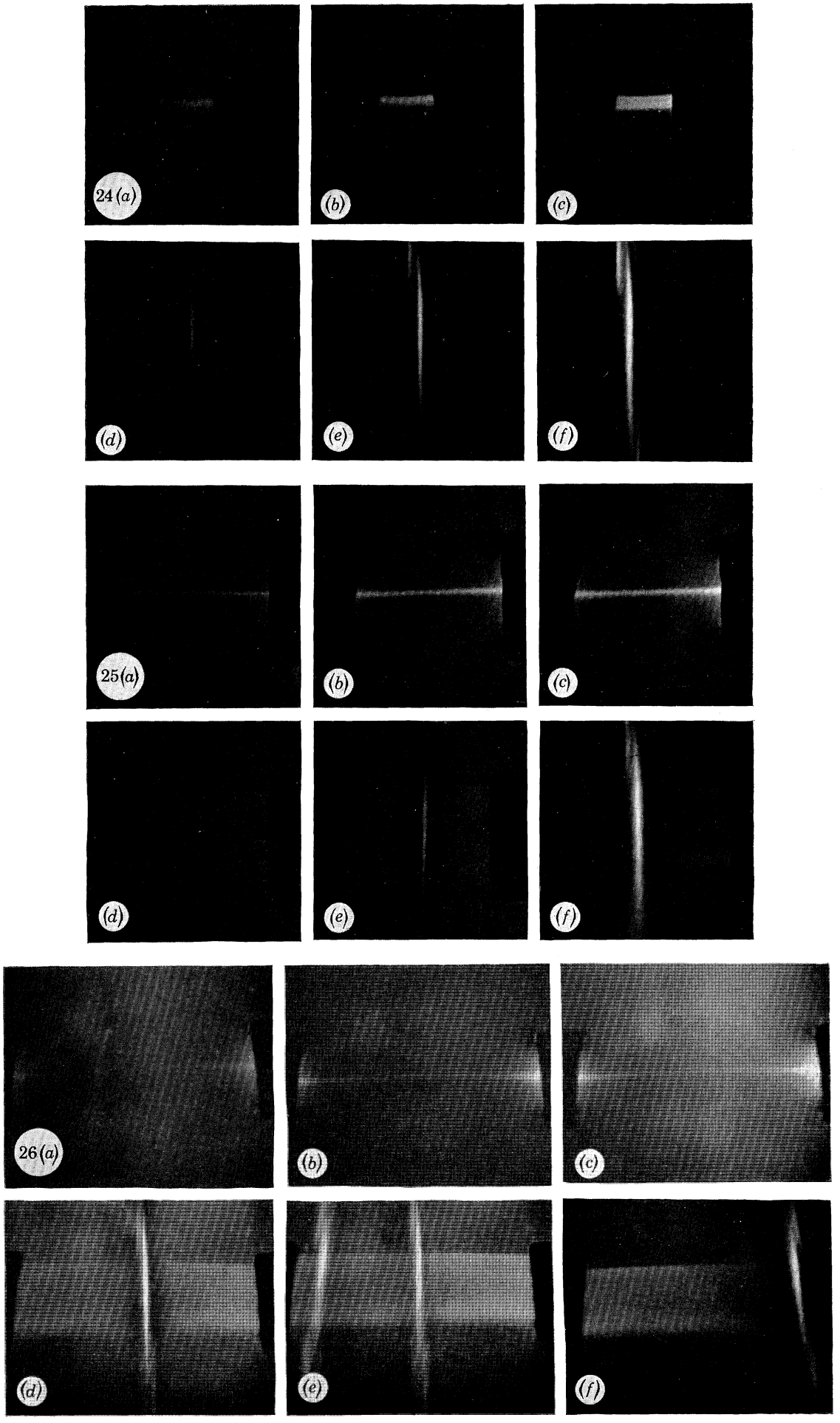

FIGURES 24–26. The development of birefringence for increasing jet velocity and jet separation. See table 1 for details.

jets. Both photographs were taken at 125 °C, well above the dissolution temperature for a 3 % solution of Rigidex type 2.

For the 'suction case' shown in figure 10 a uniform birefringence was observed localized near the symmetry axis. In the 'blow case' shown in figure 11 the localized birefringence was along the symmetry plane of the system. The situation for identical hydrodynamic and photographic conditions but with crossed polaroids parallel and perpendicular to the symmetry axis is shown in figures 12 and 13, plate 5. In the case of suction, figure 12, a very weak intensification is seen at the four corners of the jet nozzles. In the case of blowing (figure 13) four symmetrical vertical areas of weak intensification can be seen adjacent to the symmetry plane. The magnitude of the intensification is considerably less than that observed for the polars in the 45° position.

The birefringence observed can only be due to flow induced molecular alinement. Further comparison of figures 10–13 reveal that far the largest part of this orientation corresponds to molecular alinement parallel or perpendicular to the symmetry axis. By introducing a first order wave plate it was established that for the 'sucking' case the slow axis (the molecular chain axis) was parallel to the symmetry axis and for the 'blowing' case the slow axis was parallel to the symmetry plane, which in the edge on view in figure 11 gives rise to a resultant which is vertical in that photograph. The birefrinence effects described here were quite general provided a critical value of the concentration was exceeded (see later).

By viewing the jets obliquely it has become apparent that the case of suction is a simpler flow system to examine. Figures 14 and 15, plate 5, are photographs taken with the polars crossed at 45° and figures 16 and 17, plate 5, are the corresponding photographs in unpolarized light. In the case of suction shown in figures 14 and 16 the birefringence and bright field contrast can be immediately identified with a cylindrical birefringence area along the symmetry axis. For the blow case the edge on photographs of figure 11 suggested that a birefringent disk was being viewed from the side, however the oblique photographs of figures 15 and 17 show that it is a birefringent ring. Observations by means of a first order plate indicated that the slow axis was circumferential around the ring. In addition the birefringence of the ring shown in figure 15 reduces and eventually disappears at the upper and lower extremities of the ring. This is again consistent with circumferential orientation. A weak birefringence can be seen in figure 15 in the centre of the ring.

By vertically displacing one jet with respect to the other, the symmetry of the flow field between the jets could be modified. This feature is clearly shown in figures 18–23, plate 5. Figures 18–20 show the progressive displacements of jets for the case of sucking. Even for large jet displacements the birefringence persists along the displaced symmetry axis. For 'blowing' shown in figures 21–23 with the progressive increase in jet displacement the birefringence is lost along the symmetry plane. These pictures illustrate a general tendency that in suction the strong localized birefringence was insensitive to jet alinement hence it could be readily achieved, while more demanding critical alinement was needed for the 'blowing case'.

For a given jet separation a minimum jet velocity was required before any birefringence could be seen. With increasing jet velocity the intensity of the birefringence increased. The localized birefringence could be seen for jet separations ranging from about 0.5–5 mm, the largest jet separation the apparatus could achieve. Table 1 gives the details of figures 24–26, plate 6, which illustrate these effects.

It can be seen in figures 26*e* and 26*f* that for large jet separations the instabilities experienced in the 'blowing' mode become apparent. In figure 26*e* which was an eight second exposure, the area in which the jets impinge has taken up two distinct positions. The central birefringent line is

the normal position; however during the photographic exposure the area where the jets impinge has moved from the centre to a position just in front of one of the jets. For high exit velocities shown in figure 26*f* the impinging area is seen solely in one position near one of the jets. An additional feature for large jet separations is that for the sucking case the birefringence is no longer uniform along the symmetry axis as shown in figures 26*a–c*.

TABLE 1. DATA ON PHOTOGRAPHS IN FIGURES 24–26

(Observations made with polars crossed at 45°.)

	sucking			blowing		
velocity, V ...	V_{min}	V_{int}	V_{max}	V_{min}	V_{int}	V_{max}
jet separation, S_j/mm						
0.75	24*a*	24*b*	24*c*	24*d*	24*e*	24*f*
2.0	25*a*	25*b*	25*c*	25*d*	25*e*	25*f*
3.2	26*a*	26*b*	26*c*	26*d*	26*e*	26*f*

From these general observations it is proposed that flow induced molecular orientation occurs where areas of high longitudinal velocity gradients are present. In addition, areas away from the symmetry axis and plane show little or no molecular orientation. It is suspected that they are regions containing transverse velocity gradients where the molecular orientation is suppressed by the rotational nature of the flow field in accord with the theoretical predictions of § 2.

(*b*) *Permanent crystallization*

Below a certain critical temperature ($T_{c,max}$) the effects produced by flow were irreversible and were obviously associated with permanent crystallization. This took place with all concentrations investigated, namely 0.01–5 % for both 'suction' and 'blow' cases. In both cases crystallization generally occurred in regions where the localized birefringence was previously observed at higher temperatures, i.e. above $T_{c,max}$.

DESCRIPTION OF PLATE 7

FIGURES 27–41. Polars crossed at 45°.

FIGURE 27. Crystallization during suction. 3 % Rt2 solution T_c = 107 °C, $\dot{\epsilon} = 1.5 \times 10^3\ s^{-1}$.

FIGURE 28. As figure 27, after flow.

FIGURE 29. Crystallization during suction. 3 % Rt2 solution, T_c = 107 °C, $\dot{\epsilon} = 2.5 \times 10^3\ s^{-1}$.

FIGURE 30. As figure 29, after flow.

FIGURE 31. Crystallization during suction. 3 % Rt2 solution, T_c = 106 °C.

FIGURE 32. As figure 31, after flow.

FIGURE 33. Crystallization during suction. 3 % Rt2 solution, T_c = 106 °C, $\dot{\epsilon} = 2.0 \times 10^3\ s^{-1}$.

FIGURE 34. As figure 33, no flow.

FIGURE 35. Crystallization observed after flow. 5 % solution, T_c = 108 °C.

FIGURE 36. Crystallization during suction. 3 % Rt2 solution, T_c = 100 °C, $\dot{\epsilon} = 2.3 \times 10^3\ s^{-1}$.

FIGURE 37. As figure 36, after flow.

FIGURE 38. Crystal deposit which has blocked on jet.

FIGURE 39. As figure 38 after jets have been separated showing deposit extends into jets.

FIGURE 40. Crystallization during blowing. 5 % Rt2, T_c = 103 °C.

FIGURE 41. Partially collapsed crystal ring remaining after flow for conditions described in figure 40.

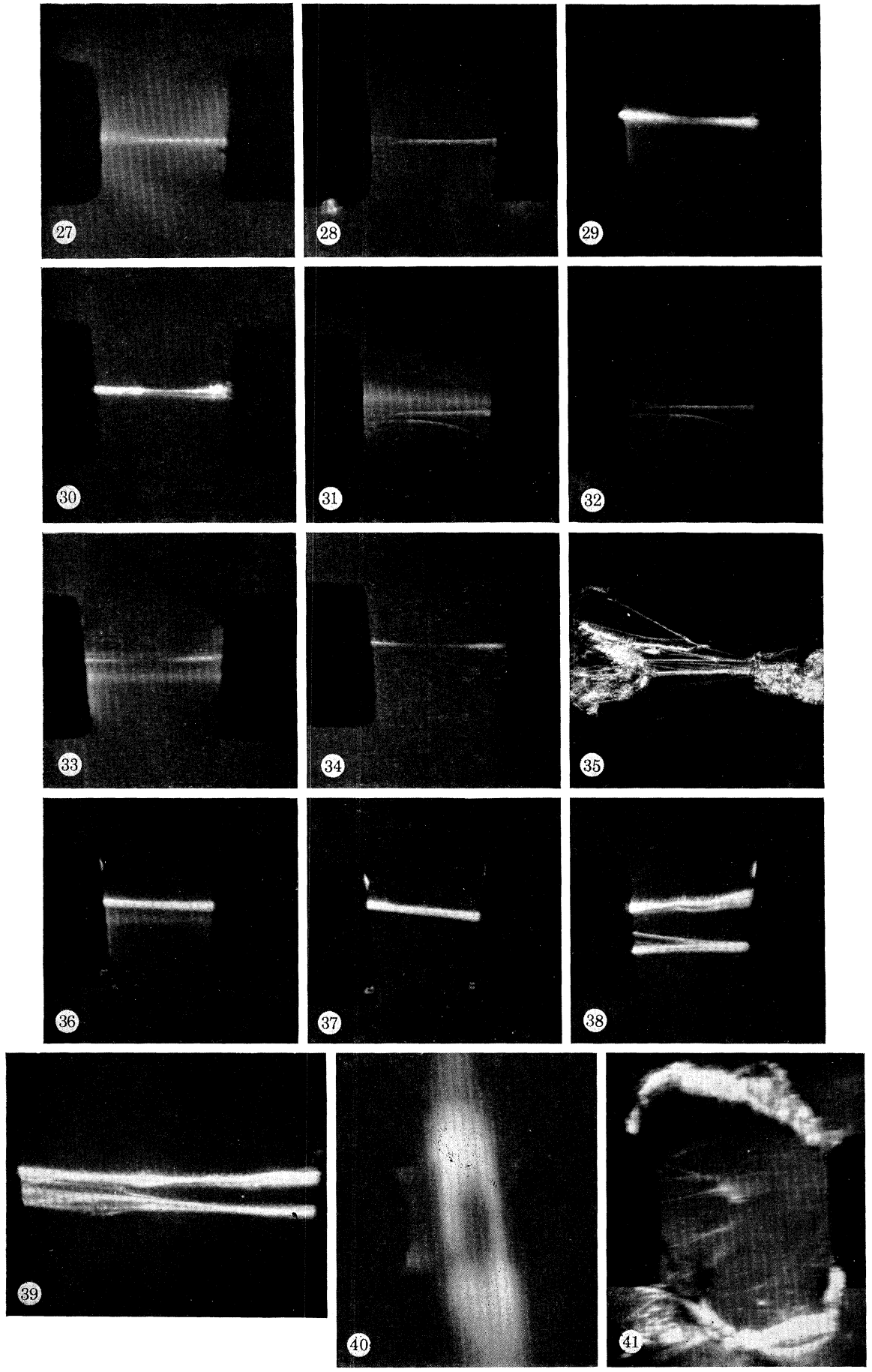

FIGURES 27–41. For description see opposite.

(*Facing p.* 40)

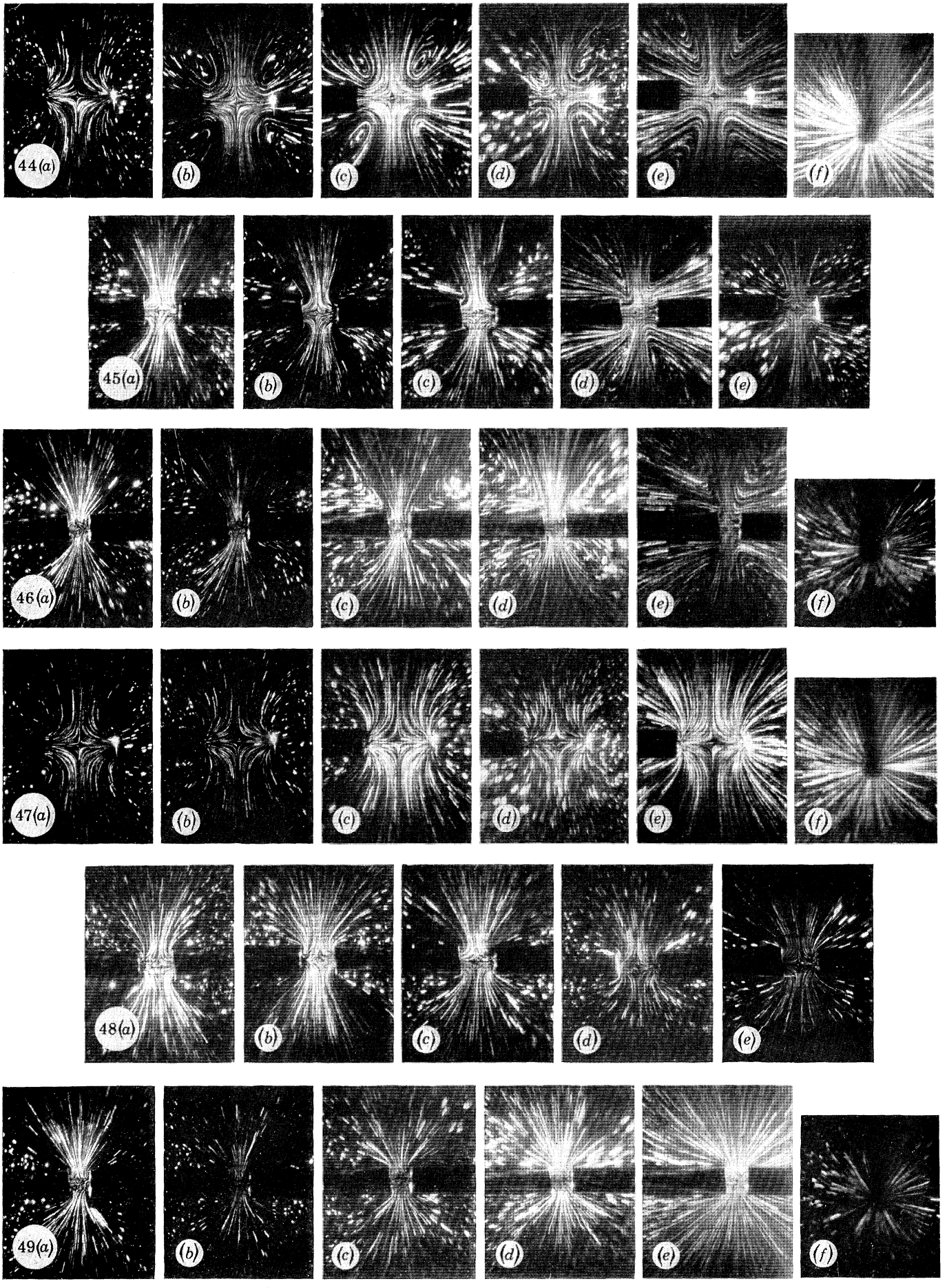

FIGURES 44–46. Streamline photographs for case of blowing (see table 2).

FIGURES 47–49. Streamline photographs for case of suction (see table 3).

In the case of sucking the development of crystal deposits is shown in figures 27–39, plate 7. The pertinent features are the areas over which the crystallization occurs and the form this takes.

The time that flow could be maintained before the reservoirs filled with polymer solution depended on the jet entry velocity and size of the jets; typical values ranged from 10 s to 2 min. During this time, if the temperature of the solution was below $T_{c,max}$ and the flow rate into the jets was sufficiently great, it was possible to induce fibrous crystallization between the jets. A birefringence localized to the region of the symmetry axis was seen as shown in figure 27 for a 3 % solution of Rigidex type 2 at a crystallization temperature (T_c) of 107 °C. After a period of time, which was dependent on both hydrodynamic and crystallization conditions and normally of the order of a few seconds, independent, or groups of, fine microscopic fibres were seen to develop within the birefringent region also visible in larger versions of figure 27. On the cessation of flow the birefringence disappeared and the fibres remained bridged between the jets (figure 28).

Figures 27 and 28 were taken for the minimum flow rate at which crystallization could be induced at that particular T_c. If the flow rate was increased the onset of crystallization occurred more readily and the amount of crystal deposit that could be obtained before the reservoirs were completely filled also increased. Figure 29 shows the crystal deposit for an increased flow rate at $T_c = 107$ °C. In this case the birefringence is practically obscured by the size of the deposit. By the time the picture was taken (figure 30) the crystal deposit remaining bridged the jets after flow had terminated. The deposit consists of an aggregation of the individual fine fibrils of the type seen in figure 27. Each fibril appears to have a length of about 1 mm. As far as a characteristic diameter can be defined at this low resolution this is in the range of 50 μm.

In some cases the fibrils were seen to migrate away from the central area where they usually develop otherwise, as shown in figures 31 and 32. The displacement in figure 31 has arisen during flow. Figure 33 shows a crystal deposit situated away from the birefringent area and figure 34 the deposit after flow has been terminated. In this case it is noticeable that the central region is thinner and less birefringent than the regions near both jets. The amount of crystal deposit achieved increases with concentration and/or supercooling. Figure 35 shows a crystal deposit from a 5 % solution of Rigidex type 2 at 108 °C. Figures 36 and 37 show crystal deposits formed and observed at $T_c = 100$ °C, for a 3 % solution. In figure 36 taken during crystallization the crystal deposit can be seen to be developing in the central region; however in addition at each edge of the jet entrance there is a birefringence intensification seen also in figure 37 taken when flow has terminated. This suggests an additional area in which crystals may accumulate.

In figure 38 a crystal was sufficiently large to block the flow in one of the jets. By increasing the jet separation after flow has stopped, it can be seen that the deposit extends into the jets (figure 39).

If the concentration is below a critical value, no birefringence is seen, nevertheless crystallization appears to proceed in a similar manner although with decreasing concentration there is progressive decrease in the amount of crystal deposit obtained for a given set of hydrodynamic and crystallization conditions.

In the case of blowing, crystallization developed in birefringent areas on the symmetry plane of the system as shown in the oblique view in figure 40. On the cessation of flow the crystal deposit would either disperse into the solution or remain partially collapsed between jets (figure 41). Here the crystal deposit has the form of a ring in which fibrous crystals with typical dimensions of a few millimetres in length and about 0.1 mm in diameter can be distinguished. In the blow case when crystal deposits develop the flow pattern invariably becomes unstable with the tendency to disperse the crystal aggregate within the solution. When the solution concentration

was very low (0.1 %) no birefringence or crystal deposit could be seen along the symmetry plane during the flow: however on the cessation of flow, individual crystal fibres would sometimes become deposited onto the regions of the jet nozzles and grow from this position.

5. Examination of flow field

(*a*) *Experimental*

A model suspension was prepared where the individual scattering particles could be made visible against a dark background when illuminated by a planar beam of light. The velocity of the particles in any particular region of the flow field could be determined from photographs of the particle tracks taken during flow, by dividing the track length of the particles by the shutter speed of the camera. The streamlines of the flow field were obtained from photographs with exposures which were longer than the time needed for the particles to traverse the field of view.

The model fluid was a 7 : 2 mixture of glycerol and water which gave an equivalent viscosity to a 5 % solution of polyethylene in xylene at 125 °C. Hostalen GUR polyethylene powder as supplied was found to provide convenient scattering particles when suspended in this fluid. The optic arrangement used is shown in figures 42 and 43. Experiments were carried out with both Newtonian liquids and solutions containing water soluble polymers. No obvious difference in the general nature of the streamlines could be found for either case.

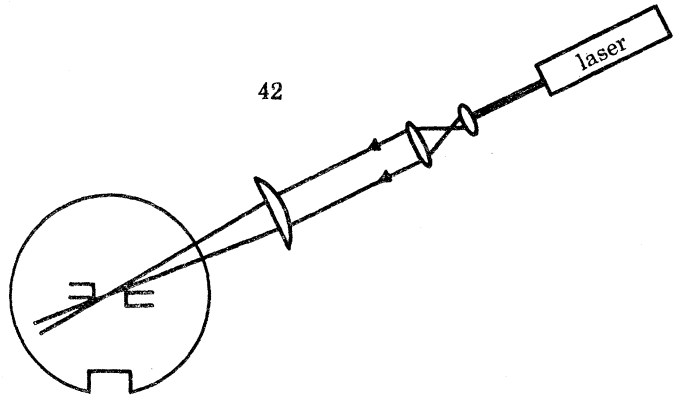

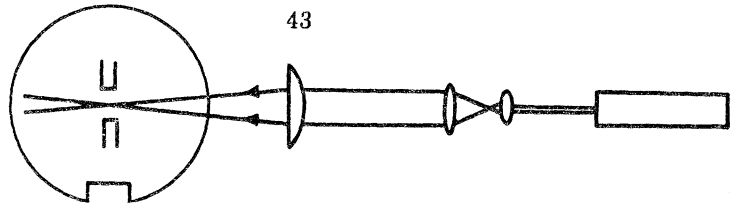

Figures 42 and 43. Optical arrangements used in particle track photography.

Figure 42. 'Face on' observation.

Figure 43. 'End on' observation.

(*b*) *Streamlines*

Figures 44–46, plate 8, relate to streamline photographs taken for the case of blowing. There are essentially two variables which will affect the hydrodynamic flow field, namely the jet exit velocity and the magnitude of the jet separation. Table 2 details the photographs shown.

The 3.5 mm jet separation series show the streamlines in greatest clarity. For smaller jet separations the light beam impinges on the jet edges giving rise to diffuse scattering which illuminates a larger area than the planar beam alone. In this situation some of the streamlines coming towards the camera are observed with the result that the flow pattern becomes less clear.

It can be seen that there is a remarkable degree of symmetry for all exit velocities and jet separations; thus satisfying the requirements for longitudinal velocity gradients to be present along the symmetry axis and plane of the system. In some of the streamline photographs the central region is devoid of any particle tracks; however in other photographs shown clearly in figures 44*a* and *c* a single bright spot is seen in the exact centre. The particle there must have remained stationary in the centre of symmetry of the flow field for at least the duration of the exposure which for the 'face on' streamline photographs was $\frac{1}{4}$ s. These observations confirm that an area of low, and at the centre zero, velocity must exist at the centre of symmetry of the system.

TABLE 2. DATA ON PHOTOGRAPHS IN FIGURES 44–46

	'face on' observation					'end on' observation	
jet exit velocity (volumetric)/m s^{-1} ...	0.14	0.35	0.6	0.9	1.5	0.35	1.5
jet separation/mm							
3.5	44*a*	44*b*	44*c*	44*d*	44*e*	44*f*	—
2	45*a*	45*b*	45*c*	45*d*	45*e*	—	—
1	46*a*	46*b*	46*c*	46*d*	46*e*	—	46*f*

In figure 44*f* the jets are viewed 'end on' along the symmetry axis of the system. The radial symmetry of the flow field is apparent which again satisfies the required symmetry conditions. The effect of increasing the jet exit velocity is shown in figures 44*a–e*. For very low jet exit velocities, figure 44*a*, the flow field appears relatively simple. As soon as fluid elements leave the jet entrances they tend to splay outwards. A small increase in jet velocity (figure 44*b*) noticeably changes the flow field. Here the fluid elements tend to remain collimated for a short distance after leaving the jets before splaying starts. In addition vortices develop in the corners of the photographs; here fluid from a region outside the jets is being swept round by the jet flow. With increasing jet exit velocity the jet collimation and vorticity become even greater as shown in figures 44*e*, 45*e* and 46*e*. In figure 44*e* the jet collimation continues to within a distance approximately equal to the jet radius away from the symmetry plane; also the vortex velocity must be approaching that of the impinging fluid, as the vortex streamlines appear continuous immediately adjacent to the impinging fluid.

Figures 47–49, plate 8, are streamline photographs taken for the case of suction. Table 3 details the individual figures.

The arguments discussed for blowing concerning symmetry and the zero velocity at the centre of the flow field are equally applicable to sucking. Both the high symmetry and stationary central particles are visible in this series of photographs. However, similarity of the two fields breaks down when comparing the contours of the streamlines away from the symmetry axis and plane. In the case of suction no collimation or vorticity is seen to develop with increasing jet entry velocity. In fact the streamlines for the two extreme velocity cases in figures 48*a* and *e* look very similar. In these cases fluid elements are being pulled into the jets through a large range of angles. Only for the lowest velocity tested for each case (figures 49*a* and 44*a*) do the two flow patterns appear similar.

The streamlines were also examined for the case of misalinement (figure 50, plate 9). The details of the streamline observations made for misalined jets are given in table 4. The most striking observation is that a small misalinement for blowing destroys the symmetry of the flow field, whereas for suction the symmetry is maintained even for very large jet displacements. In addition, the sensitivity with which alinement is required for blowing is clearly contrasted with the coarse adjustment sufficient to produce a symmetrical flow pattern for sucking. This is completely consistent with the response of the birefringence to misalinement observed in the polymer solutions.

TABLE 3. DATA ON PHOTOGRAPHS IN FIGURES 47–49

	'face on' observation					'end on' observation	
jet exit velocity (volumetric)/m s^{-1} ...	0.14	0.35	0.6	0.9	1.5		
jet separation/mm							
3.5	47*a*	47*b*	47*c*	47*d*	47*e*	47*f*	—
2	48*a*	48*b*	48*c*	48*d*	48*e*	—	—
1	49*a*	49*b*	49*c*	49*d*	49*e*	—	49*f*

TABLE 4. DATA ON PHOTOGRAPHS IN FIGURE 50

(Jet exit velocity = 1.5 m/s; jet separation = 3.5 mm.)

	figure	
misalinement	blow	suck
none	50*a*	50*f*
small vertical displacement	50*b*	50*g*
large vertical displacement	50*c*	50*h*
small horizontal displacement by rotation	50*d*	50*i*
large horizontal displacement by rotation	50*e*	50*j*

(*c*) *Point velocities*

The success of measuring point velocities was limited; however sufficient information was obtained to characterize the velocity gradients to the accuracy required for the interpretation of the birefringence effects in the polymer solutions.

Particle track photographs for the blowing case are shown in figure 51, plate 9, with the corresponding details given in table 5. It is apparent for the same hydrodynamic conditions the track length of the particles is dependent on the time of the exposure. There was not complete correlation for velocities measured at different shutter speeds. This was attributed to four factors, namely: the shutter speeds were accurate to within only 10 %; particle positions were not completely reproducible on successive photographs; with increasing track length the particle experienced varying velocities along the particle track and, for long track lengths it was more probable that the track would leave the illuminated area and thereby go partly unobserved.

TABLE 5. DATA ON PHOTOGRAPHS IN FIGURE 51

(Jet separation = 3.5 mm; jet internal diameter = 1.0 mm; jet exit velocity = 0.25 m/s.)

	figure			
shutter speed/s ...	$\frac{1}{125}$	$\frac{1}{60}$	$\frac{1}{30}$	$\frac{1}{8}$
observation				
face on	51*a*	51*b*	51*c*	51*d*
end on	51*e*	51*f*	51*g*	51*h*

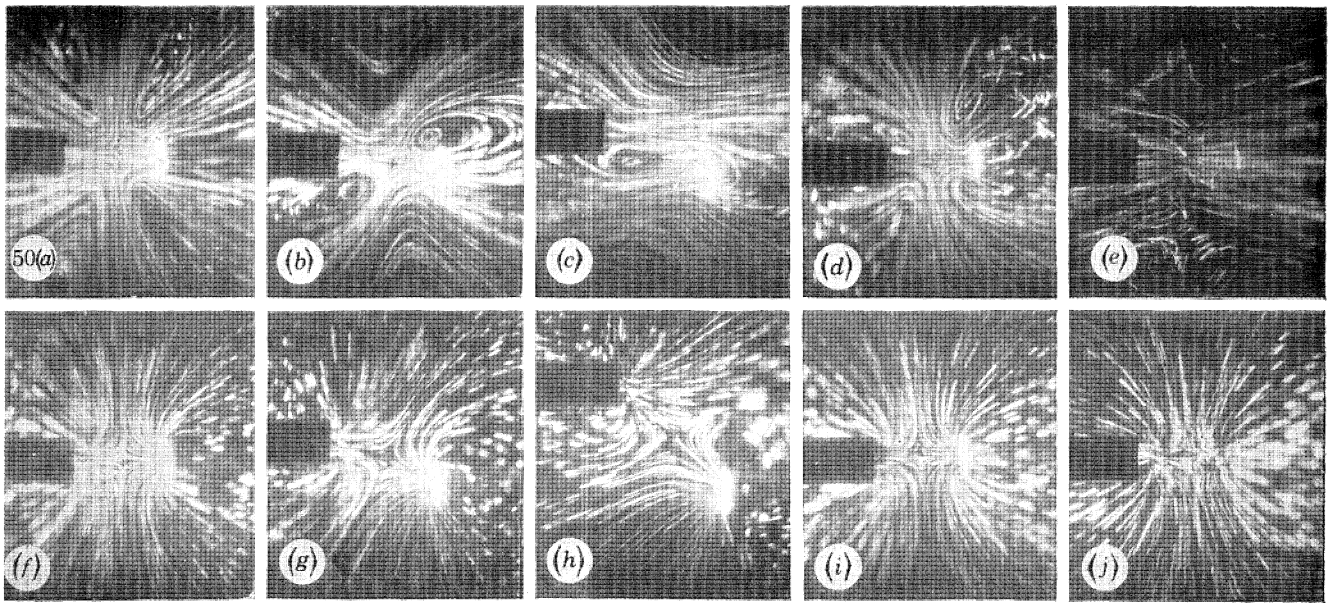

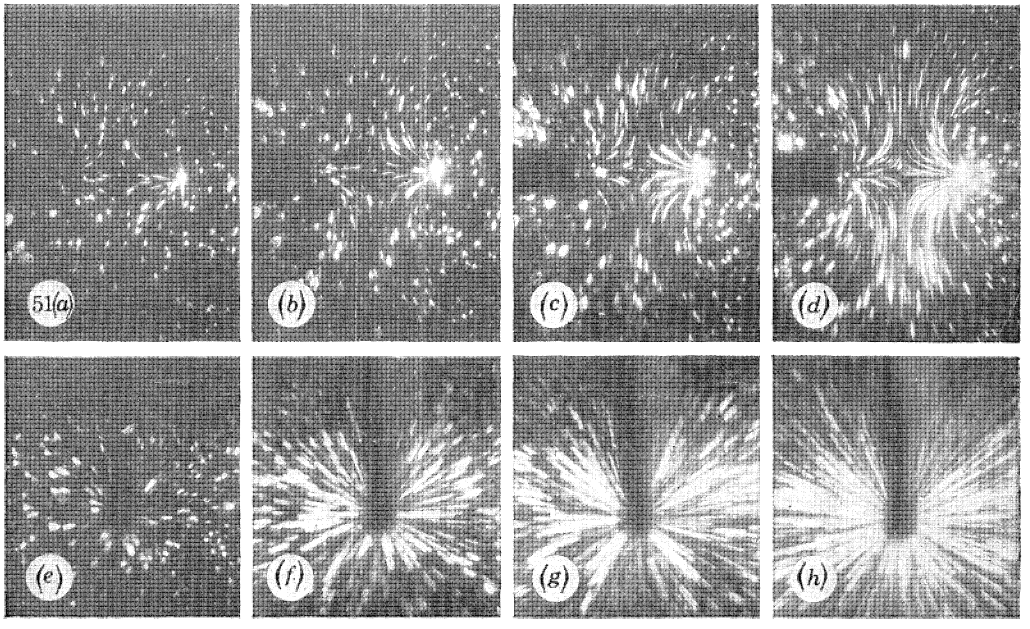

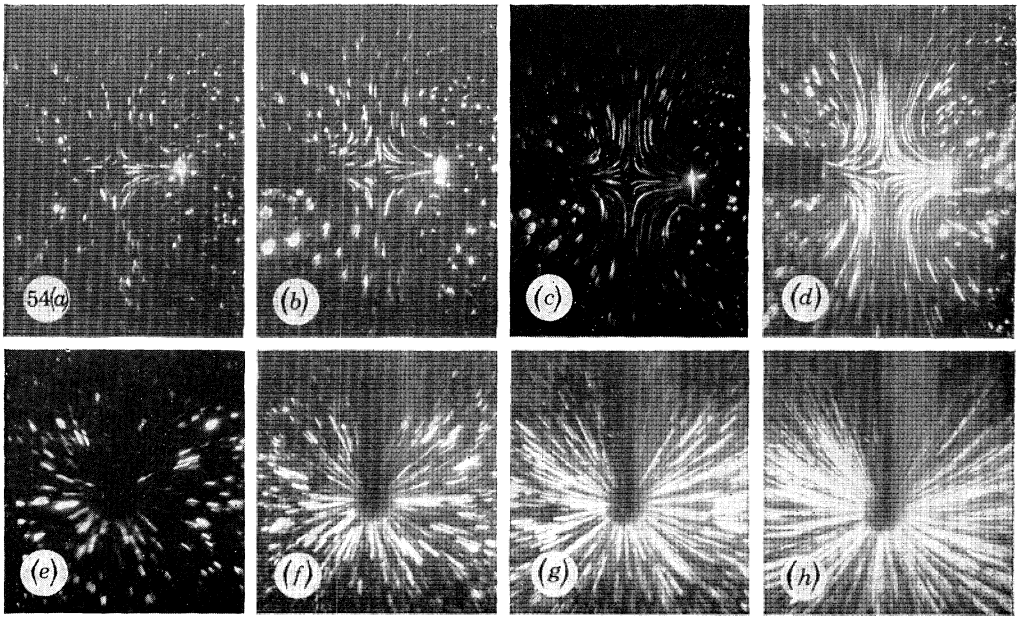

FIGURE 50. Photographs showing the effect of misalinement for sucking and blowing (see table 4).

FIGURE 51. Point velocity photographs for the case of blowing (see table 5).

FIGURE 54. Point velocity photographs for the case of sucking (see table 6).

(*Facing p.* 44)

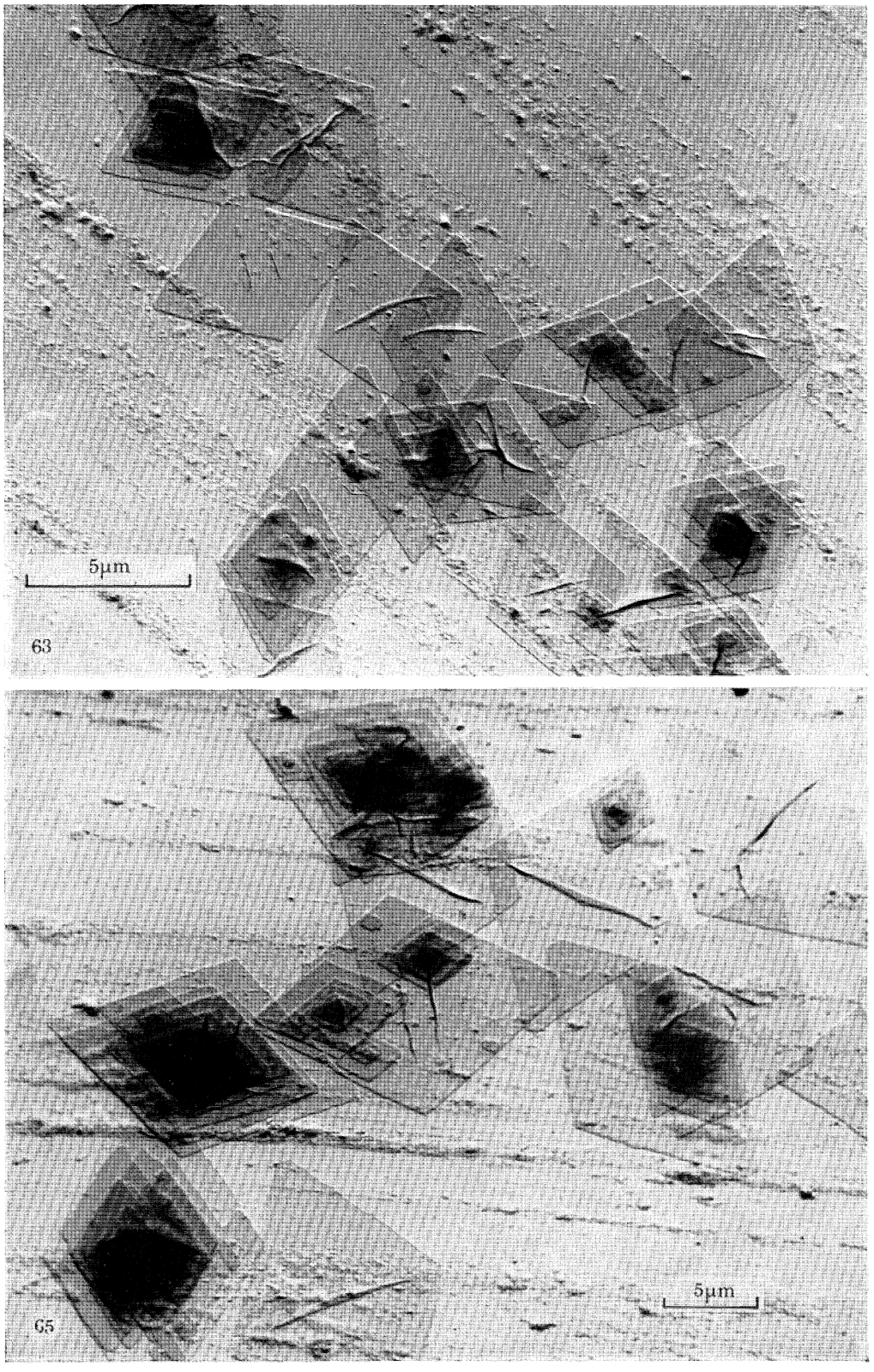

FIGURE 63. Electron micrograph of seeded single crystals; T_c = 100 °C.

FIGURE 65. Electron micrograph of seeded single crystals; T_c = 100 °C. Starting solution had been degraded for 2 h without antioxidant.

These factors make the 'face on' track velocity measurements unreliable. Even so from a large number of photographs of the type shown in figures 51 *a–d* certain positive conclusions could be made concerning the velocity distribution. These are

(1) The velocity distribution out of the jets was of an approximate parabolic form for all jet exit velocities.

(2) For the collimated regions of flow, where the fluid leaves the jets, the velocity distribution does not change.

(3) The velocity along the symmetry axis appears to remain uniform until a distance of about $\frac{1}{2}r$ away from the centre of symmetry, where r equals the jet radius.

End-on observations of the form shown in figures 51 *e–h* gave more reproducible results from which the radial velocity on the symmetry plane could be mapped. Measurements were taken for a given radius by averaging particle track velocities for four different shutter speeds and averaging over the whole circular section. The results are shown in figure 52.

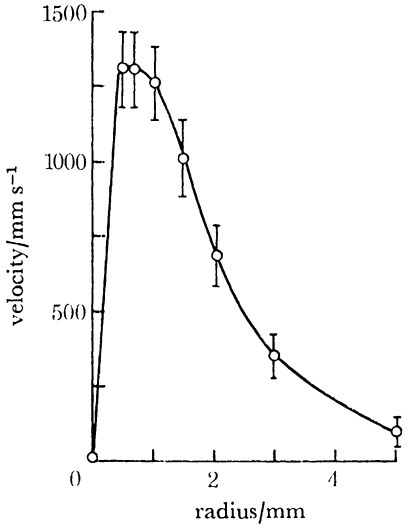

FIGURE 52. Graph of velocity profile along the symmetry plane for the case of blowing.

Within the experimental error the form of the curve remained similar for all jet velocities and jet separations; they only differ in the relative magnitudes of the velocities. The jets obscure observations in the region $r = 0$ to $r =$ external radius of jets. However, as it has been established that the velocity at the centre must be zero; this point has been added to the present graph and the full velocity profile obtained by the joining of this point to the experimental points beyond $r =$ external radius of jet.

By making simple assumptions it is possible to determine the three principal strain rates on the symmetry plane. Assuming cylindrical symmetry about the symmetry axis, the principal strain rates are: $\dot{\epsilon}_{rr}$, , strain rate in radial direction; $\dot{\epsilon}_{xx}$, strain rate parallel to symmetry axis; $\dot{\epsilon}_{\theta\theta}$, strain rate in circumferential direction. We have $\dot{\epsilon}_{rr} = \partial V_r/\partial r$; $\dot{\epsilon}_{00} = (1/r)V_r$; $\dot{\epsilon}_{xx}$ is obtained from the relation: $\dot{\epsilon}_{xx} + \dot{\epsilon}_{rr} + \dot{\epsilon}_{00} = 0$.

By using the values for the radial velocities in figure 52 the three principal strain rates were plotted as a function of the radius in figure 53. It can be seen in the region marked A in figure 53 that $\dot{\epsilon}_{rr}$ and $\dot{\epsilon}_{00}$ are both positive and of comparable magnitude. $\dot{\epsilon}_{xx}$ is negative. This is therefore a region of axial compression. In region B, $\dot{\epsilon}_{rr}$ becomes negative while $\dot{\epsilon}_{00}$ remains positive and

$\dot{\epsilon}_{xx}$ negative. This region is therefore one of axial extension, where fluid elements are being extended in a circumferential direction. In region C all strain rates become small with a resulting small axial compression developing.

This result can explain qualitatively the observed birefringence phenomena for polymer solutions for the case of blowing. In the central region a weak birefringence was seen: this is consistent with a region of axial compression where a planar molecular orientation would be expected. With increasing radius the axial compression changes to a circumferential axial extension. In this region the molecules should become alined in a circumferential direction to form a birefringent ring. This again is consistent with experimental observations. The birefringent ring is at a radius of about 1.5 mm. This is in agreement with the strain rate analysis according to which the region of maximum circumferential axial extension is at a similar radius (figure 53). The above results refer to the symmetry plane; the more complex situation in other localities was not analysed further.

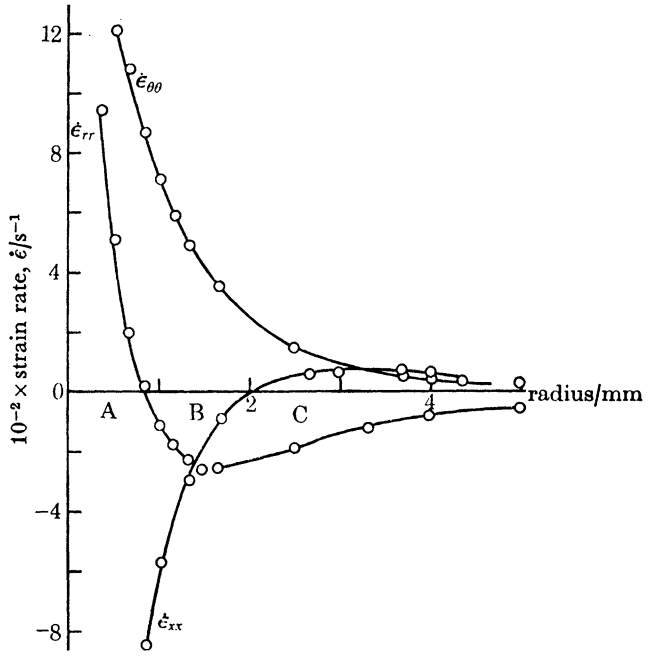

FIGURE 53. Graph of strain rates on the symmetry plane for the case of blowing.

TABLE 6. DATA ON PHOTOGRAPHS IN FIGURE 54

(Jet separation = 3.5 mm; jet internal diameter = 1.0 mm; jet exit velocity = 0.25 m/s.)

shutter speeds	$\frac{1}{125}$	$\frac{1}{60}$	$\frac{1}{30}$	$\frac{1}{8}$
observation	figure			
face on	54*a*	54*b*	54*c*	54*d*
end on	54*e*	54*f*	54*g*	54*h*

Particle track photographs for the sucking case are shown in figure 54, plate 9, with the corresponding details given in table 6, from which the following definitive conclusions could be made.

(1) The jet velocity was uniform across the diameter of the jet nozzles.

(2) The value of the entry velocity was equal to the volumetric velocity in the jet calculated from the rate of rise of the fluid level in the reservoir tube.

(3) The velocity at the centre of symmetry was zero and appeared to increase uniformly from the symmetry centre to each jet entrance, for jet separations up to 2.5 mm.

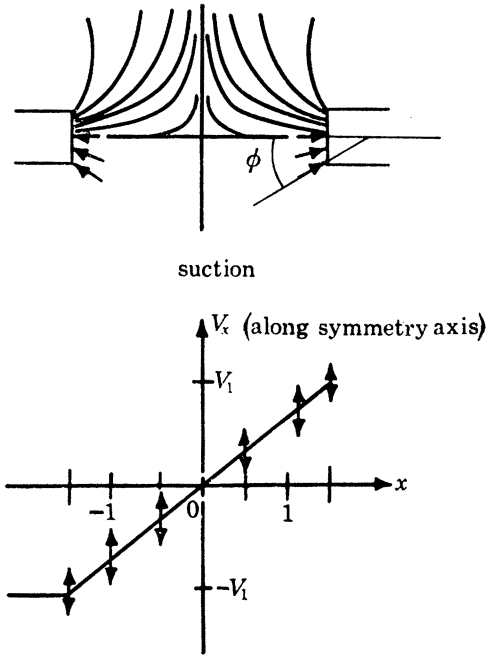

FIGURE 55. Diagrammatic summary of flow field for sucking case.

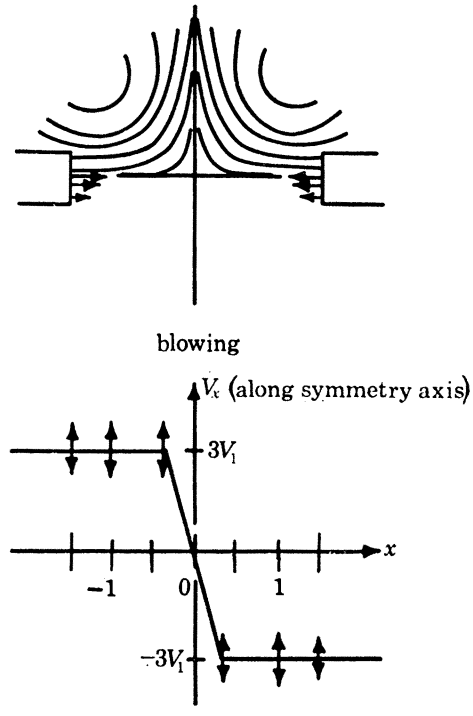

FIGURE 56. Diagrammatic summary of flow field for blowing case.

(*d*) *Mathematical representation*

The experimental details of the flow fields for sucking and blowing are summarized diagrammatically in figures 55 and 56 respectively.

Three attempts were made to fit model streamline and velocity profiles with observed data, they are summarized as follows:

(i) Uniaxial extension and compression.

(ii) Impinging stream flow of limiting axial velocity.

(iii) Representation of flow field by two point sinks for suction case.

(i) *Uniaxial extension and compression*

The velocities in the cylindrical symmetry case of uniaxial compression are given by

$$V_x = -\dot{\epsilon}x,$$

where $\dot{\epsilon}$ is the applied velocity gradient, and

$$V_r = \tfrac{1}{2}\dot{\epsilon}r.$$

Uniaxial extension would merely reverse the signs of the above equations. The stream function θ for these two cases is given by Loitsyanski (1966) as

$$\theta = \tfrac{1}{2}\dot{\epsilon} \times r^2.$$

Both velocities and streamlines are plotted in figure 57 for the case of uniaxial compression. With the direction of flow reversed these curves would be unrealistic for the case of sucking because in this situation the streamlines were 'pulled into the jets' from all points outside the jets; in this representation all streamlines originate from the symmetry plane. The predicted flow pattern bears a closer resemblance to the blow case, although here it has the serious weakness in that the velocity along the symmetry axis increases uniformly and indefinitely. To overcome this problem a second approach was examined.

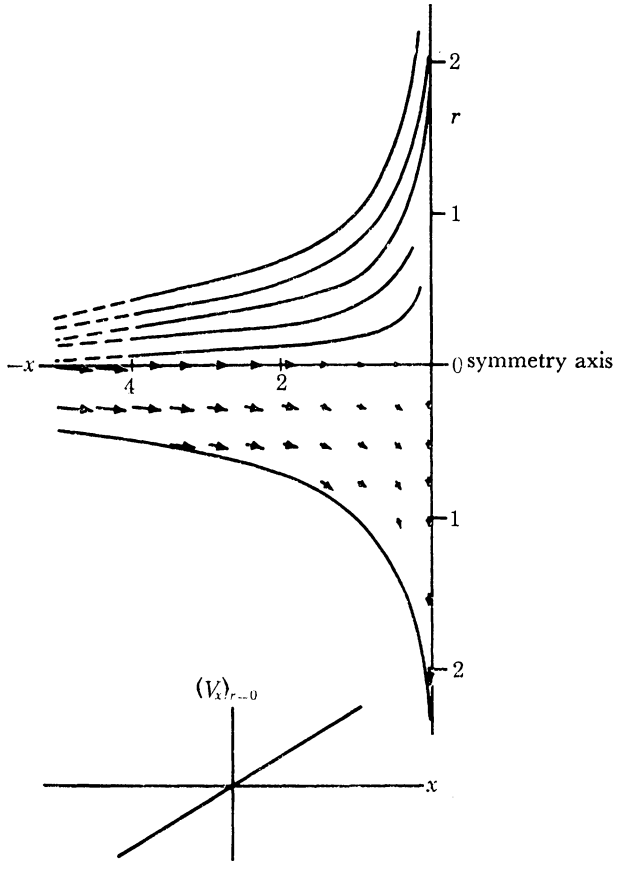

FIGURE 57. Diagram of flow field for uniaxial compression.

(ii) *Impinging stream flow of limiting axial velocity*

In this analysis an expansion method proposed again by Loitsyanski (1966) was used which enabled the velocity at any point $V(xr)$ to be obtained numerically provided the axial velocity $V(x)$ was known. For the case of impinging jet streams and an axial velocity profile given by

$$V_x = \frac{1}{2\pi^{\frac{1}{2}}} \int_0^x e^{-\frac{1}{2}x^2} dx$$

the velocities and stream function were obtained and are plotted in figure 58. Again these streamlines are most appropriate to the blow case. In this formulation $\partial V_r/\partial x$ has a finite value everywhere except on the symmetry axis and plane; thus longitudinal velocity gradients only exist on their own in these regions. In addition the magnitude of the longitudinal velocity gradient on the symmetry axis is only appreciable in the region of the symmetry centre. Thus the longitudinal velocity gradient is limited to the symmetry centre and symmetry plane. Flow birefringence for

the polymer solution was seen limited to these regions supporting the concept that molecular orientation only occurs in the regions of longitudinal velocity gradients.

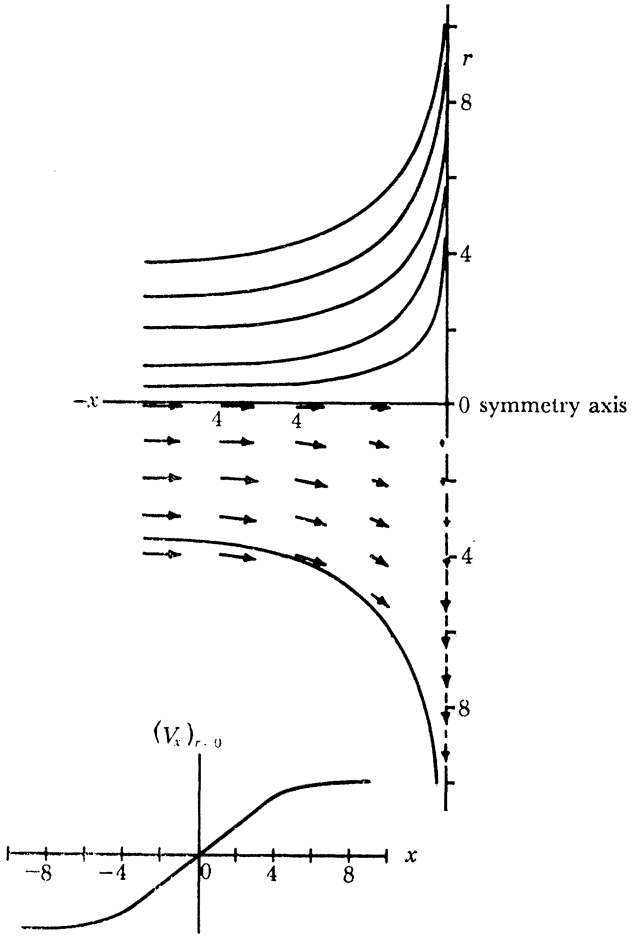

FIGURE 58. Diagram of the flow field predicted by Loitsyanski taking axial velocity to be an e.r.f. function.

(iii) *Representation of flow by two point sinks for suction case*

The velocity at a position r away from a single 'point sink' is given by: $V_r = b/r^2$ where b is a constant. By considering two sources a distance $2a$ apart it is possible to determine by simple geometry V_x and V_r. The resultant velocities are shown together with the streamlines in figure 59. It can be seen that the forms of the streamlines are in good agreement with the experimental streamlines shown in figure 55 for the case of suction; the streamlines are not realistic for the blowing case.

V_x and V_r are given analytically by the expressions

$$V_x = b\left\{\frac{(a-x)}{[(a-x)^2+r^2]^{\frac{3}{2}}} - \frac{(a-x)}{[(a+x)^2+r^2]^{\frac{3}{2}}}\right\}, \tag{5.1}$$

$$V_r = -b\left\{\frac{r}{[(a-x)^2+r^2]^{\frac{3}{2}}} + \frac{r}{[(a+x)^2+r^2]^{\frac{3}{2}}}\right\}. \tag{5.2}$$

By differentiating these expressions the various strain rates are determined. Again it was found that the only areas free from any rotational components, namely $\partial V_x/\partial r$ and $\partial V_r/\partial x$, were the symmetry axis and symmetry plane which were areas of uniaxial extension.

The value of the extensional strain rate in these regions is given by

$$(\dot{\epsilon}_{xx})_{r=0} = b\left\{\frac{2}{(a-x)^3}+\frac{2}{(a+x)^3}\right\}, \tag{5.3}$$

$$(\dot{\epsilon}_{xx})_{x=0} = b\left\{\frac{6a^2}{(a^2+r^2)^{\frac{5}{2}}}-\frac{2}{(a^2+r^2)^{\frac{3}{2}}}\right\}. \tag{5.4}$$

For values of r less than $\frac{1}{2}a$ the magnitude of the strain rate on the symmetry plane is comparable to that along the symmetry axis. This result is surprising because with a polymer solution molecular orientation was visible as a birefringence along the symmetry axis, but was not seen on the symmetry plane except at $x = 0, r = 0$, i.e. where the symmetry axis intersects the symmetry plane.

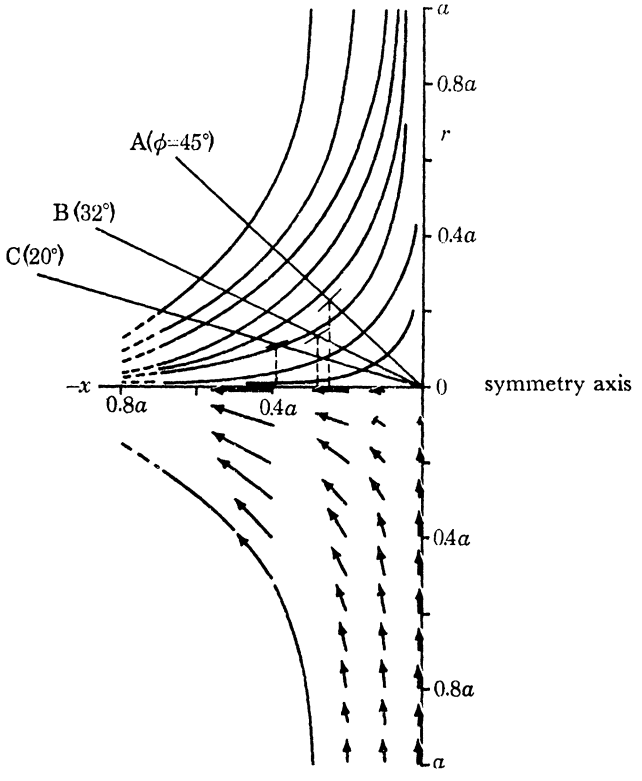

FIGURE 59. Diagram of flow field produced by two point sinks.

If the increase in velocity between the centre and the jet was linear the velocity gradient along the length of the axis would be constant and of a magnitude

$$\dot{\epsilon}_1 = V_1/D, \tag{5.5}$$

where D is the distance of the jet from the centre of symmetry and V_1 the velocity of entry. From the previous theoretical analysis the strain rate at the centre of the symmetry axis is given by equating r to zero in equation (5.4)

$$(\dot{\epsilon})_{x=0} = 4b/a^3. \tag{5.6}$$

By using equation (5.1) with the information $(V_{xx})_{x=0,\,r=0} = V_1$ and substituting in (5.6)

$$(\dot{\epsilon})_{x=0} = \frac{V_1}{D}\left(\frac{(C-1)^2(C+1)^2}{C^4}\right),$$

where $C = a/D$. For increasing values of C, $(\dot{\epsilon})_{x=0}$ approaches the value of $\dot{\epsilon}_1$.

A suitable value of C must be chosen to fit the experimental observations. This necessitates fixing the position of the jet entrance with respect to the flow lines shown in figure 55. Experimentally streamline photographs were taken for three values of D (D = 0.5, 1.0 and 1.75 mm) with jets of jet radii d = 0.5 mm. Thus the position of the inside edge of the jet must lie somewhere on the lines OA, OB, OC shown in figure 59 given by $r = (d/D)\,x$ for each respective value of D.

The angle of entry, ϕ, of the streamlines at the inner edge of the jet, shown in figure 55, was measured for each jet separation. The exact position of the inner edge of the jet was then obtained for each jet separation by moving along the respective line drawn in figure 59 until the measured angle ϕ corresponded to the tangent of one of the streamlines. By using this method the following values of C were obtained for the three jet separations

$$D = 0.5\,\text{mm}, \quad C = 4.0, \quad D = 1.0\,\text{mm}, \quad C = 3.6; \quad D = 1.75\,\text{mm}, \quad C = 2.5.$$

The accuracy of the results is poor owing to the uncertainty in the measurements of ϕ, however the results are still significant.

Within experimental error the first two measurements of the value of C are the same. Taking C as 3.8

$$(\dot{\epsilon})_{x=0} = 0.86(V_1/D).$$

This is very close to $\dot{\epsilon}_1$ given by equation (5.5). In addition for this value of C, $\dot{\epsilon}$ does not change appreciably over the length of the symmetry axis given by equation (5.3).

For the larger jet separation

$$(\dot{\epsilon})_{x=0} = 0.62(V_1/D).$$

This is nearly a factor of two lower than $\dot{\epsilon}_1$, also the strain rate can no longer be considered as being uniform along the length of the symmetry axis.

These results are consistent with the observed behaviour for polymer solutions for the case of suction. For small jet separations the birefringence was uniform but for the largest jet separations examined it was seen to increase towards the jet entrances.

In conclusion, this mathematical representation seems to represent the experimentally observed flow field moderately well and its predictions are consistent with the observed behaviour of macromolecules in the flow field, with the exception that theoretically a region of uniaxial extension is predicted on both the symmetry plane and axis while experimentally it is only observed along the symmetry axis.

(*e*) *Conclusions*

The correlation of the properties of the flow discussed in this section with the molecular behaviour of a polymer solution are summarized below.

(1) *Symmetry.* The existence of high symmetry and a region of zero velocity at the centre of symmetry was established. According to the arguments in § 3, this is a sufficient requirement for longitudinal velocity gradients to exist on the symmetry axis and plane. If the velocity gradient is of a sufficient magnitude molecular orientation would be expected in these regions. For polymer solutions localized molecular orientation was seen along the symmetry axis for suction jets and symmetry plane for blow jets.

(2) *Blow jets.* From an analysis of the velocity distribution on the symmetry plane it was established that the central region was an area of uniaxial compression. Further away from the symmetry centre an area of circumferential uniaxial extension existed. This is consistent with the form of the birefringence seen on blowing, namely, a weak central birefringence area bounded by a circumferentially oriented birefringent ring.

It was also found that with increasing jet exit velocity a vortex motion from fluid outside the jets developed. This seems to coincide with the appearance of birefringent wings seen when large jet exit velocities were used for polymer solutions.

(3) *Suction jets.* It was established that the axial velocity increased continuously between the centre of symmetry and the jet entrance, thus a positive extensional strain rate would exist in this region. This is consistent with the birefringence localized along the whole length of the symmetry axis.

(4) *Misalinement.* With misalinement the symmetry of the flow was maintained for 'suction jets' and destroyed for 'blow jets'. This coincides with the persistence of birefringence for sucking and the total loss of intensification of birefringence for blowing when the jets are misalined.

(5) *Mathematical model of flow.* A reasonable matching of observed streamlines with theoretical models could be achieved for both flow systems. Further matching of point velocities would be necessary for an exact solution.

6. Parameters affecting fibrous nucleation

The maximum temperature at which crystallization can be observed ($T_{c,max}$) is a useful measure of the ability of the system to nucleate fibrous crystals. Favourable molecular and hydrodynamic conditions correspond to high $T_{c,max}$ and vice versa. In this section the experimental variables influencing $T_{c,max}$ will be explored. The suck jet case was used throughout as here the flow field was simpler than for blowing and hence the strain rate could be reliably estimated in the region where the molecular elongation took place. The materials were, Rigidex type 2 and Hostalen GUR.

The solutions were prepared in the normal way in the required concentration. Because of difficulty in dissolving, concentrations beyond 1.5 % were not used in the case of Hostalen GUR. Unless specifically stated otherwise, 1.0 % of antioxidant *N*-phenyl-2-naphthylamine was added to the solution. In the various experiments to follow the solutions were cooled from 115 °C at a rate of less than 0.25 °C/min. At every half a degree, fluid was sucked into the jets at a specified velocity for a period of 15 s. The temperature was progressively dropped until a permanent crystal deposit could be seen remaining between the jets after flow which then defines $T_{c,max}$ under the circumstance in question. The deposit could be dissolved by reheating the solution to 125 °C, after which a new experiment could be performed.

(*a*) *Strain rate dependence*

A fixed concentration was chosen, 3 % in the case of Rigidex 2 and 1.5 % in the case of Hostalen GUR. It was established in § 5 that for jet separations less than 2 mm the strain rate along the symmetry axis was very nearly equal to

$$\dot{\epsilon} = V/D = 2V/S_j,$$

where V is the jet entry velocity and S_j is the jet separation. The present experiments were carried out for $S_j = 1.5\,\text{mm}$ consequently the above expression could be used.

Figure 60 reveals that $T_{c,\max}$ is affected by both the strain rate and the molecular mass. For a given material $T_{c,\max}$ increases with strain rate to a limiting value. The effect of the molecular mass is twofold. First, the minimum strain rate required to crystallize at any temperature is lower for higher molecular masses. Secondly, the limiting $T_{c,\max}$ that can be reached is larger for the high molecular mass material; it is 112 °C for the Hostalen GUR (the highest which we could achieve throughout this work) and 108 °C for Rigidex 2. Both these effects are consistent with the increased facility of the higher molecular mass material to form fibrous crystals.

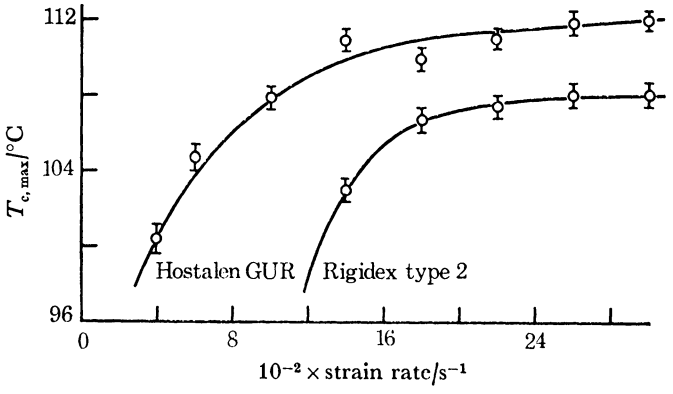

FIGURE 60. Graph of $T_{c,\max}$ against strain rate.

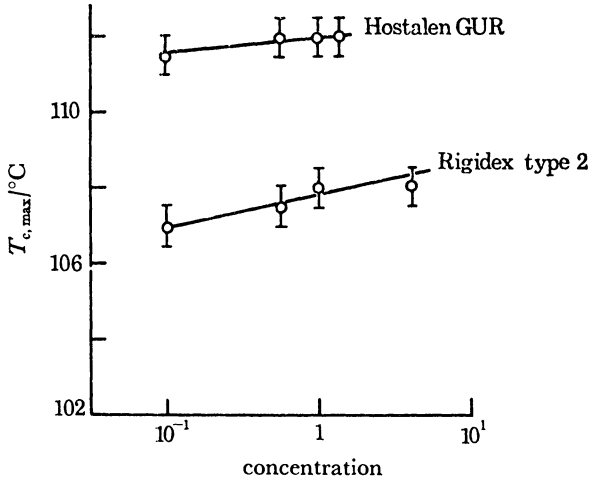

FIGURE 61. Graph of $T_{c,\max}$ against concentration.

(*b*) *Concentration dependence*

The results are shown in figure 61, for a jet entry velocity of 1.5 m/s. They indicate that there is very little concentration dependence of the crystallization phenomena. However, the maximum temperature at which crystallization is observed is higher by 4 °C for the higher molecular mass material.

(*c*) *Molecular mass dependence*

It was noticed that for a polymer solution containing no antioxidant $T_{c,max}$ was highly dependent on the time that the solution was held at an elevated temperature. A reduction in $T_{c,max}$ of up to 8 °C could be simply achieved by storing the solution at elevated temperatures for a period of the order of 5 h. As this effect was not observed for solutions that did contain antioxidant it was assumed the effect of oxidation on the polymer molecules was causing the reduction in the ability to form fibrous crystals. If oxidative scission of the molecules takes place at random, the probability that a molecule is cut is directly proportional to the molecular mass of the molecule. Thus the longer molecules will be more susceptible to degradation. To test this, changes in the molecular mass involving the highest end of the distribution, possibly beyond 10^6, would need to be assessed. Gel permeation chromatography records the full distribution, but becomes unreliable beyond molecular mass of 10^6. A specific method for characterizing the ultimate high end of the molecular mass distribution of a crystallizable polymer is provided by the 'self-seeding' technique of Blundell, Keller & Kovacs (1966). Its application for molecular mass characterization is described by Blundell & Keller (1968).

The essentials are as follows: by slowly heating suspensions of polymer crystals above the clearing point tiny crystal residues consisting of the highest molecular mass fraction of the polymer persist. After rapid quenching to an appropriate supercooling these residues will nucleate single crystal growth. The resulting suspension will consist of crystals which are all of uniform size as they all started growing simultaneously. The number of these crystals will correspond to the number of nuclei from which they have originated and thus provide a measure of the amount of highest molecular mass fraction in the starting material. This number can be readily ascertained from the size of the uniform crystals. The absolute magnitude of the number of nuclei is sensitive to several variables involved in the seeding process. However, if these are standardized changes in the high molecular mass content of the distribution can be assessed with unusual sensitivity.

The degradation experiment was conducted in two stages

(1) The ascertaining of the dependence of the $T_{c,max}$ as a function of storage time, and the collection of sample solutions for seeding.

(2) The self seeding of the sample solutions and the measurement of the number of nuclei present.

The first part of the experiment was carried out in the following manner. Two 2 % solutions of Rigidex type 2 were prepared, one with, the other without antioxidant. In what follows the two solutions were subjected to similar treatments and used in identical experiments. $T_{c,max}$ was determined in the usual way for a jet separation of 1.5 mm and for suction velocity of 1.5 m/s. The crystals formed in the course of this determination were dissolved by raising the temperature of the whole bath to 125 °C, and the solution was stored at this temperature for specified time intervals in order to induce the suspected oxidative degradation. To promote such degradation every half minute the apparatus was cycled by emptying and then filling the reservoirs at a volumetric jet velocity of 1.5 m/s. Samples of the solution were obtained after $\frac{3}{4}$, $2\frac{1}{2}$, 5 and 7 h and subsequent maximum crystallization temperatures were obtained after $2\frac{1}{2}$, 5 and 7 h by means of the procedure described above. The dependence of the maximum observed crystallization temperature on degradation time is shown in figure 62. For solutions containing antioxidant the depression of $T_{c,max}$ was small, if present at all. For the solution containing no antioxidant the depression of $T_{c,max}$ was appreciable and increased with increasing degradation time.

The second part of the experiment was carried out as follows

(1) Each sample obtained from the last experiment was filtered and, where necessary, the deposit was washed thoroughly in acetone to remove the antioxidant.

(2) After drying *in vacuo*, 60 ml of 0.001 % (polymer–xylene) solutions were prepared for each sample and then crystallized for 24 h at 80 °C. (This was carried out to ensure the starting morphology of all the samples was the same.)

(3) 20 ml of each sample was then seeded by placing the sample tubes in a temperature bath held at 80 °C and then slowly raising the temperature of the bath at an average rate of 4° C/h to a seeding temperature of 100 °C. When the seeding temperature was reached the bath was maintained at that temperature for a further hour. (At this temperature only the high molecular mass nuclei persist, the remainder of the material dissolves.)

(4) After maintaining the solutions at the seeding temperature for 1 h the test tubes were removed from the temperature bath and quickly put in another maintained at 80 °C. The samples were kept at this temperature for a further 24 h to allow complete crystallization of all the polymer to take place.

(5) The size of the seeded crystals was obtained by spraying the crystal suspension onto carbon-coated grids and measuring the dimensions of the crystals from micrographs of the crystals on the grids. Typical micrographs of the form shown in figure 63, plate 10, were obtained.

It can be seen in figure 63 that the crystals are all of the same dimensions confirming that they are self seeded.

If N is the number of nuclei per gram of polymer and m the mass of each crystal then $Nm = 1$ and since $m_c = \rho dA$ (where ρ is the density of crystal, d the thickness of crystal and A the area of crystal) then

$$N = 1/\rho dA. \tag{6.1}$$

for $T_c = 80\,^{\circ}\mathrm{C}$, $d = 12.5\,\mathrm{nm}$ and $\rho = 1.00\,\mathrm{g\,cm^3}$. Thus a measure of the area of the seeded crystal will give a direct measure of the number of nuclei per gram present.

The results of the number of nuclei present as a function of degradation time is shown in figure 64. The form of the curves is closely similar to those shown in figure 62 for the dependence of $T_{c,\max}$ on degradation time. It can be seen in figure 64 that without antioxidant the number of seeds decreased with increasing degradation time. This is a reflexion on the size of the seeded crystals becoming larger which is shown in figures 63 and 65, plate 10. Figure 63 corresponds to zero degradation time and figure 65 to material stored hot for 2 h. The area of the crystals from the latter is by a factor of 1.6 greater.

When antioxidant is present the number of seeds, and consequently the amount of high molecular mass material remains unchanged. This indicates that there is no appreciable degradation effect. In the absence of antioxidants degradation effects are observed. The number of seeds, and consequently the amount of high molecular mass material, decreases noticeably with increasing degradation time. The degradation must be a consequence of oxidation and not due to mechanical effects because no degradation is seen when antioxidant is introduced into the solution.

The ability to obtain fibrous crystallization is reflected in the amount of high molecular mass material present. When there is a reduction in the latter, there is a corresponding reduction in the maximum temperature at which fibrous crystallization can be detected. It follows from the nature of the self seeding test that changes in the highest end of the distribution are involved. These

observations confirm and supplement those of the earlier sections that the formation of fibrous crystallization is highly dependent on the molecular mass of the molecules. The greater the molecular mass the greater the ability to nucleate fibrous crystallization.

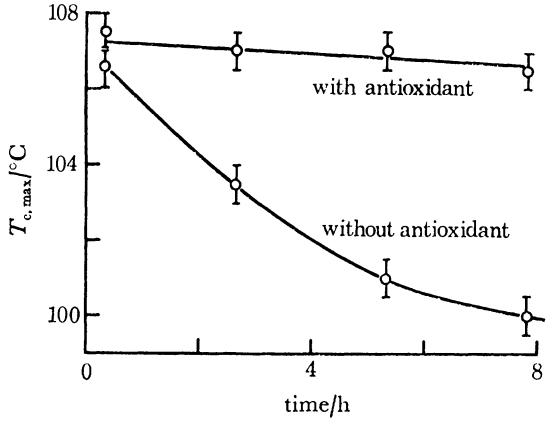

FIGURE 62. Graph of $T_{c,max}$ against degradation time.

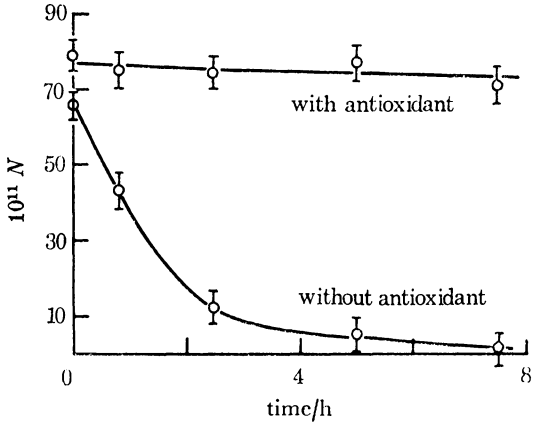

FIGURE 64. Graph of number of seeds, N, against degradation time.

7. MAGNITUDE OF FLOW BIREFRINGENCE

Here the magnitude of the birefringence seen at temperatures where crystallization does not occur, i.e. above $T_{c,max}$, will be examined and its dependence on the major variables of the system established.

Again the simpler sucking jet experiment was used. For the determination of the birefringence from the retardation actually measured the thickness of the birefringent feature needs to be known. In view of the cylindrical symmetry of the flow field it seemed reasonable to assume that the birefringent strip seen along the symmetry axis was cylindrical in cross section, in which case the maximum thickness of the birefringent area can then be equated to the observed width of the birefringent strip seen. The birefringence is then given by

$$\Delta = R/d_1, \tag{7.1}$$

where R is the maximum retardation measured in the birefringent area and d_1 the width of the birefringent strip. R was calculated from a rotatable quartz compensator introduced between polars crossed in the 45° position. Illumination was provided from a mercury arc lamp by using the 546 nm spectral line.

The conditions for measuring birefringence were not ideal because the polarized light beam had to travel through the reflux bath containing a fairly high concentration of polymer and through several glass walls all of which cause a deterioration in extinction conditions. In addition most measurements had to be taken in a period of about 30 s and in some cases less time, owing to the limited duration of the flow. Both these restrictions reduced the accuracy of the retardation measurements. The measurement of d_1 introduced a further inaccuracy because of the indefiniteness of the exact position of the edge where the retardation became vanishingly small.

(*a*) *Strain rate dependence*

The detailed studies on the effect of strain rate were carried out on a 2 % Rigidex type 2 solution containing antioxidant maintained at 125 °C. The strain rate was taken as defined by $\dot{\epsilon} = 2V/S_j$. It was varied both by altering the exit velocity (V) and the jet separation (S_j). For the apparatus used there was a limit on the maximum velocity at which the fluid can be sucked into the jets, which limited the maximum strain rate which could be achieved, this maximum value being lower for larger jet separations in accordance with the above relation. This will be apparent from the results in figure 66.

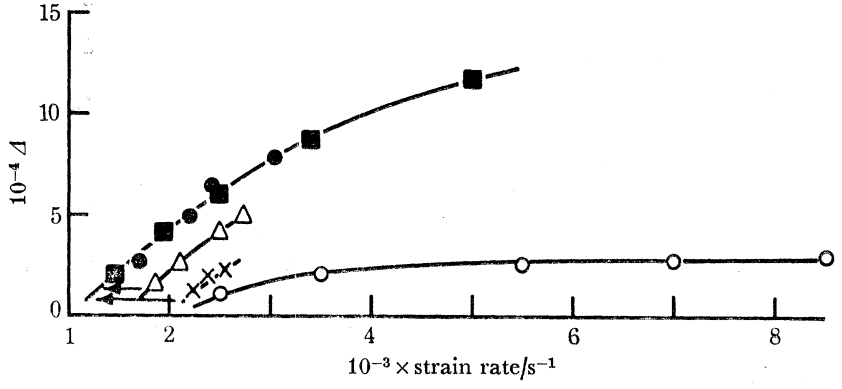

FIGURE 66. Graph of birefringence against strain rate for different jet separations.
○, S_j = 0.7 mm; ■, S_j = 1.4 mm; ●, S_j = 2.0 mm; △, S_j = 2.9 mm; ×, S_j = 3.5 mm.

The birefringence was measured at the centre of symmetry of the flow field. Each measurement was obtained from the average of six retardation measurements three taken on either side of the compensator zero. The width of the birefringent area was measured from photographs.

The results are shown in figure 66. They reveal immediately that the birefringence is highly strain rate dependent. Above a minimum strain rate the birefringence increases with increasing applied strain rate.

From the curves in figure 66 a jet separation effect is apparent. For S_j of 1.4 and 2.00 mm the points lie on the same curve, however for other jet separations the points are on independent curves. By a horizontal displacement to the left it is possible to fit the curves with S_j = 2.9 and 3.5 onto the 1.4 and 2.00 mm curve. The 0.7 curve appears to bear little relation to any of the others.

It would appear that when S_j becomes very small, as in the 0.7 mm case, the flow field between the jets no longer is of the same form as for the wider jet separations. This is acceptable, because

when the jets are close the effects of the jet walls outside the jet entrance would be anticipated to introduce shearing into the flow field and consequently reduce the elongational efficiency and hence birefringence of the system.

The results of the larger jet separations are consistent with the theoretical analysis in § 5. Thus for $S_j = 2$ mm the approximation that the strain rate was given by the equation $\dot{\epsilon} = 2V/S_j$ seems to be valid. With increasing S_j this value was an overestimation of the strain rate at the symmetry centre. For S_j of 3.5 mm the strain rate was reduced by a factor of 1.6 as a shift of this magnitude would bring these points along the 3.5 mm curve into better agreement with those corresponding to $S_j = 1.4$ and 2.00 mm. Similarly a smaller shift of the 2.9 mm jet separation points would bring these also into coincidence. In this way a master curve is obtained which is independent of jet separation. Figure 66 indicates that the birefringence tends to a saturation value with strain rate. It would have been desirable to obtain some higher strain rate values to establish this point. There are two limitations to this. First, the results shown in figure 66 indicate that with much reduced jet separation the nature of the flow field and consequently its ability to aline molecules are affected and secondly, if higher velocities than already used are achieved, turbulence sets in.

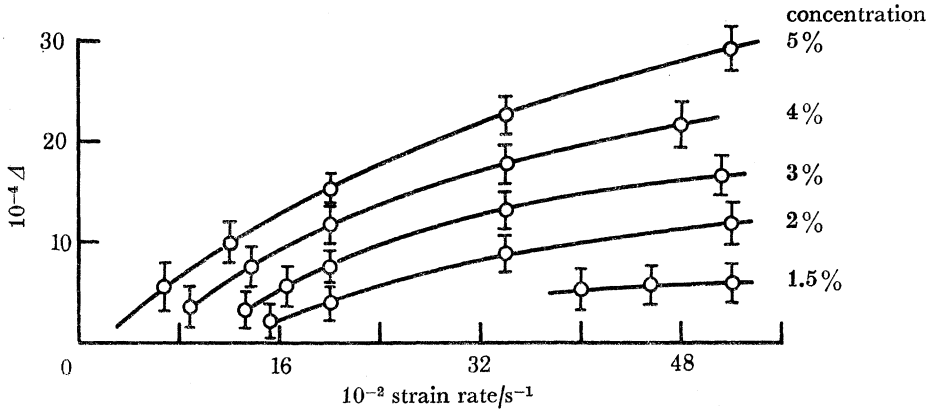

FIGURE 67. Graph of birefringence against strain rate for different concentrations.

(b) Concentration dependence

The birefringence for a series of different concentrations of Rigidex type 2 was measured as a function of strain rate. The temperature was maintained at 125 °C and a fixed jet separation of 1.5 mm chosen. All solutions contained antioxidant.

The resulting birefringence against strain rate curves (figure 67) are all of the same form levelling off towards a limiting maximum value which is in itself an increasing function of concentration, in fact from 2 % upwards is closely proportional to concentration. This indicates that the molecules are in a corresponding state of alinement in the different dilutions.

The above proportionality, however, does not hold for concentrations below 2 %. In fact the birefringence decreases abruptly when going from 2 to 1 % concentration and around 1 % there if no observable effect left. This abrupt change suggested that the birefringence phenomenon was associated with a cooperative molecular effect. Such a cooperative effect could take place at a critical concentration, in other words by entanglements. Below the critical concentration the molecules would be essentially independent of one another and thus from previous arguments only the very high molecular mass molecules could be extended giving insufficient alined material to exhibit any flow birefringence. In the region of the critical concentration some of the molecules

would become interlocked which could have important consequences for the molecular elongation.

If two or more molecules become physically interlocked as envisaged at around the critical concentration the relaxation time of the coupled molecules would be expected to be greater than the relaxation times of either of the individuals. As molecular elongation is essentially dependent on the product $\dot{\epsilon}\tau$, in a system containing entangled molecules a greater percentage of the molecules will become extended and thus the possibility of observing any flow birefringence will be correspondingly increased.

A simple estimate of the critical concentration of monomolecular length molecules can be made.

Assume each molecule occupies a sphere of radius r, then each molecule occupies a volume

$$V_i = \tfrac{4}{3}\pi r_i^3.$$

The probability that any point in unit volume is not occupied by the ith molecule is $(1-V_i)$. The probability that a point is not occupied by any molecule is

$$P = \Pi^n(1-V_i),$$

where there are n molecules in unit volume of solution. Now

$$\ln P = \ln \Pi^n(1-V_i) = \sum^n \ln(1-V_i) \approx -\sum^n V_i.$$

The limit of freedom from entanglements may be taken roughly as $P = 1/e$, thus,

$$1 = \sum^n V_i = \tfrac{4}{3}n\pi r_i^3.$$

Let c be the concentration in $\mathrm{g\,cm^{-3}}$. Thus in $1\,\mathrm{cm^3}$ there are $cA/M = n$ molecules where A is the Avogadro number and M the molecular mass of polymer. Substituting for n gives

$$c = \frac{3}{4}\frac{M}{Ar_i^3}.$$

Because the critical concentration depends on the third power of the equivalent sphere radius it is important that a realistic value is chosen. In this analysis we let r_i be equal to half the r.m.s. end-to-end distance h_0 given in § 2, equation (2.2), then

$$c = \frac{3}{4}\frac{M}{A(\frac{1}{2}bN^{\frac{1}{2}}\cot\frac{1}{2}\alpha)^3}.$$

For polyethylene: $N = \frac{1}{14}M$, $b = 0.154\,\mathrm{nm}$, $\cot^2\frac{1}{2}\alpha = 2$.

Thus for a monodisperse polyethylene where $M = 2\times10^5$, $c = 1.2\times10^{-2}\,\mathrm{g\,cm^{-3}}$ assuming $\rho = 1\,\mathrm{g\,cm^{-3}}$ then $c = 1.2\,\%$, which is the same order of magnitude observed for the experimentally observed Rigidex type 2 critical concentration. Similarly a molecular mass of 10^7 would give $c = 3\times10^{-3}\,\mathrm{g\,cm^{-3}}$ ($c = 0.3\,\%$) corresponding to Hostalen GUR where birefringence was seen for a 0.1 % concentration solution and not observed for a 0.01 % solution.

(*c*) *Assessment of maximum chain alinement*

From the refractive index measurements of Bunn & Daubeny (1954) for crystals of hatchetitte ($C_{36}H_{74}$) it is possible to calculate the maximum birefringence anticipated from 100 % crystalline and perfectly alined polyethylene with the additivity of bond polarizabilities and the Lorentz–

Lorenz relation assumed as applicable and with the density of polyethylene known. Taking the density of 100 % crystalline polyethylene as $1.000\,g\,cm^{-3}$ the maximum birefringence is

$$\Delta = 0.064.$$

The presence of imperfect orientation, amorphous contributions and form birefringence in bulk polyethylene make it impossible to directly check this value. Assuming it to be correct and making the assumptions that this birefringence corresponds to the 100 % concentration solution and in addition that the birefringence (for lower concentration solutions) is proportional to the concentration, the birefringence for a c % concentration with all the molecules perfectly alined will be

$$\Delta = 6.4 \times 10^{-4} c.$$

This value is to be compared with the observed maximum experimental birefringence values in figure 68. It can be read off directly that beyond $c = 2$ % this corresponds closely to the theoretical maximum. With the implicit assumption that the concentration in the birefringent regions is identical to that for the overall solution this result leads to the important conclusion that the chains have been fully alined, illustrating the chain extending efficiency of the jet flow.

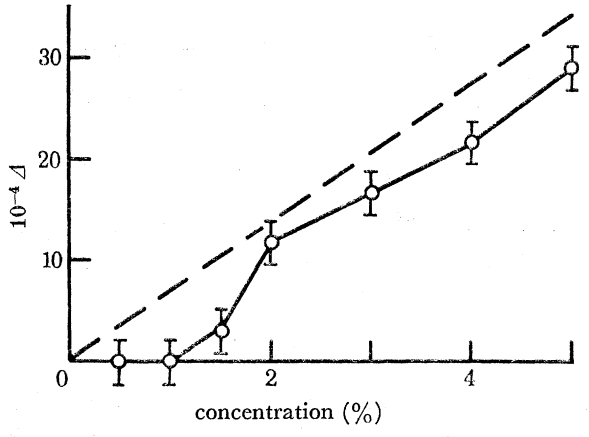

FIGURE 68. Graph of observed birefringence with concentration.

The postulate of complete, or nearly complete, chain alinement clearly relies on the correctness of the polarizability figures. There is no absolute certainty as regards these figures, in fact values notably different from those used also feature in the literature. We believe nevertheless that the values of Bunn & Daubeny (1954) are the most realistic. The alternative bond polarizability figures published by Denbigh (1940) and discussed by Volkenstein (1963) from depolarization data in the gas phase differ from those of Bunn & Daubeny (1954) mainly by assigning a very low value for the transverse polarizability of the C—C bond. Denbigh's figures would give a theoretical birefringence of 0.37 for perfectly alined polyethylene crystals which seems unrealistic when compared with the observed value of 0.059 for $C_{56}H_{74}$.

In any event the mere existence of a saturation value of a limiting Δ is equivalent to the existence of a limiting degree of orientation. It would be difficult to envisage this to be anything else but the fully alined chain. By plausibility argument alone no intermediate state of elongation is expected to correspond to the limiting state which accordingly should be the fully alined chain.

(*d*) *Temperature dependence*

The variation of the observed birefringence with temperature is shown in figure 69. Two strain rates were chosen for a 2 % Rigidex type 2 solution containing antioxidant. The jet separation was maintained at 1.5 mm. As seen the birefringence is practically unaffected by variations in temperature. The small effect that can be discerned corresponds to a linear increase in the birefringence with decreasing temperature.

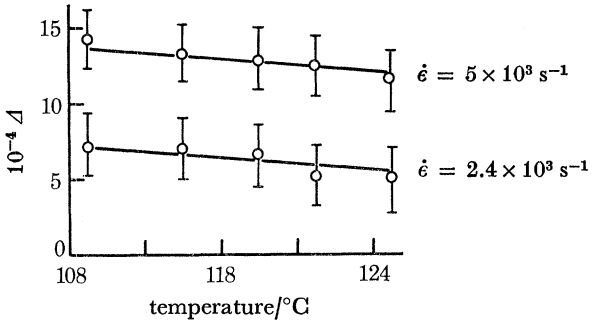

FIGURE 69. Graph of birefringence against temperature.

(*e*) *The effect of degradation*

The effect of oxidative degradation on the birefringence was examined following the analogous studies relating to the crystallization behaviour in § 6. The material was Rigidex type 2 in 2 % solution containing no antioxidant. The birefringence itself was measured at 125 °C.

The results displayed by figure 70 show that the birefringence changes only very slightly with storage time at high temperature in contrast to the crystallization behaviour in § 6. It appears therefore that the birefringence is insensitive to changes in the high end tail of the molecular mass distribution contrary to what has been observed for the formation of fibrous crystals.

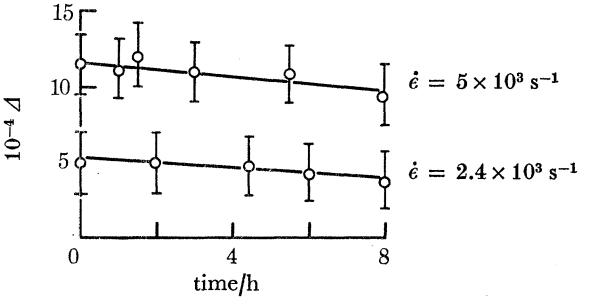

FIGURE 70. Graph of birefringence against degradation time.

A final important point must be considered when the crystallization phenomena observed in § 6 are reconciled with the observed birefringence of this chapter. Both the birefringence (above $T_{c,max}$) and the crystallization phenomena depend on molecular weight. Nevertheless there is a notable difference in the way the two are affected. The birefringence relies on the average molecular mass, while crystal nucleation is in addition sensitively affected by the longest molecules in the distribution. As shown in § 7, under conditions when by the birefringence evidence the chains are fully alined, minute reductions in the highest end of the molecular mass

distribution markedly reduces the ability to crystallize during flow while the birefringence as measured above $T_{c,max}$ remains unaffected corresponding to complete chain alinement. This immediately implies that chain alinement as diagnosed by birefringence is not an adequate criterion for defining conditions of crystallization. A possible explanation of this result is that chains of differing molecular weights are not all quite equally alined, the birefringence evidence notwithstanding. In molecular terms the straightening of the chains will occur by cooperative rotations around C—C bonds leading finally to an all-*trans* chain configuration (*ttt*... sequence). In reality such all-*trans* sequences may establish themselves along limited chain portions first, separated by regions of mixed *trans* and *gauche* (*g*) sequences, a variety of such sequences being parellel to each other and to the flow lines. This would then give rise to kinks in the otherwise straight chain. For example, the simplest kink of this kind would be a ---*tttgtḡttt*--- sequence: another more complex one termed a jog (Pechhold 1971) is ---*tttgtttḡtts*. The birefringence would not be markedly affected by an occasional kink or jog of this kind yet the perfection of the crystal, if such portion became incorporated in it, would, hence the tendency towards crystallization would be reduced.

Clearly the statistical theory of rubber elasticity cannot be applied any longer at this high degree of chain extension. The pulling out of kinks of the kind in question will involve cooperative movement of whole large chain portions and will thus require larger forces than aligning the statistical segments in the equivalent random chain as defined by the single force constant K in equation (2.3). Further, the force required will increase as the number of kinks is reduced. As longer molecules will experience increasing extensional forces in a longitudinal velocity gradient they should contain fewer residual kinks and jogs than the shorter chains, even when by birefringence evidence both may appear to be fully extended. The increased facility of the longest chains to form crystals will then follow.

8. Morphology

(*a*) *Experimental*

Samples for electronmicroscopy were collected by passing carbon coated grids between the jets after crystallization had taken place. Special efforts were made to remove all solute so that the grids should contain only crystals formed at the high temperature and under the action of flow and that no additional solute material should precipitate during subsequent cooling. A thimble, volume about 5 cm^3, was placed into the crystallizing bath before the experiment. After the temperature had stabilized crystallization was produced by jet flow in the usual manner. After collecting the precipitate the grids were placed into the glass thimble. Both grid and thimble were kept submerged in the hot xylene during this manipulation. The thimble containing the grid was rapidly transferred into pure xylene held at the same temperature. The content of this second bath was repeatedly exchanged with a new fresh xylene until the liquid could not contain more

---

Description of plate 11

Figure 71. Electron micrograph of shisk kebabs observed from a sample crystallized during suction at T_c = 103 °C from a 1.5 % solution of Rigidex type 2. Sample had been washed at 103 °C.

Figure 72. Enlarged view of figure 73.

Figure 73. Electron micrograph of shish kebabs observed for a sample crystallized under identical conditions to the sample in figure 73. The material is Hostalen GUR.

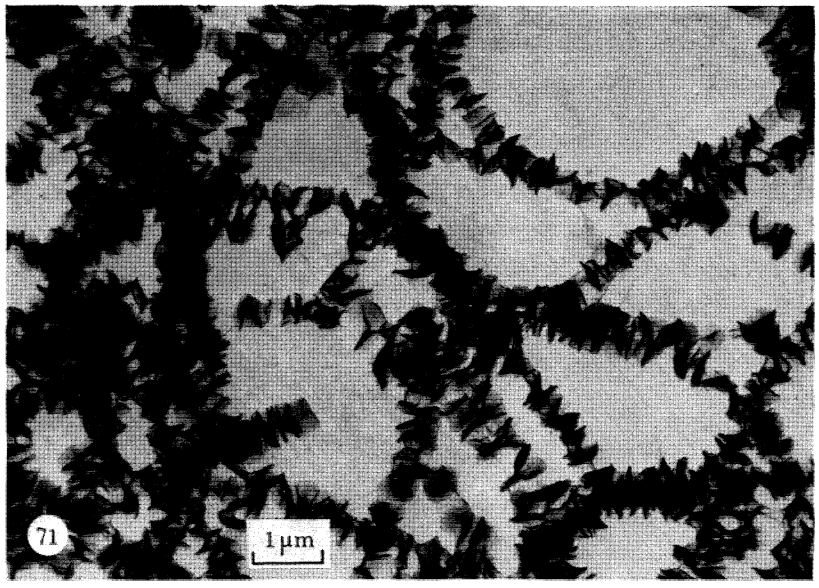

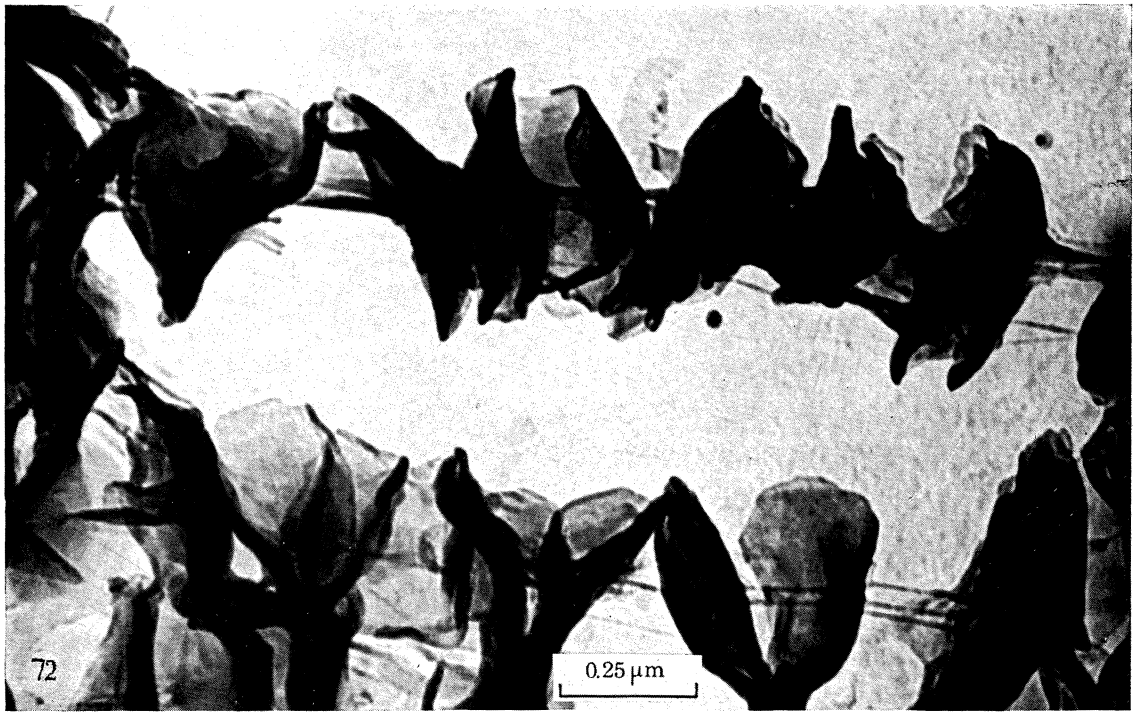

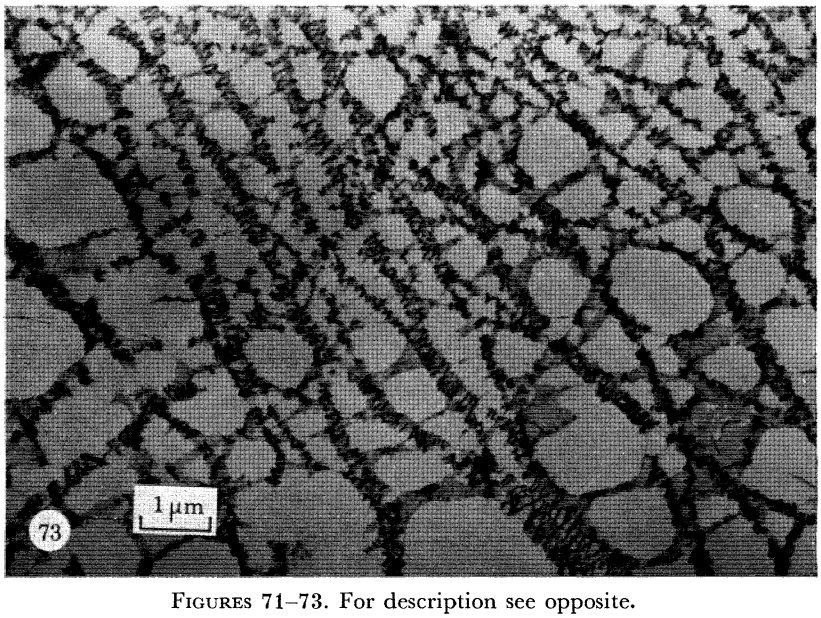

FIGURES 71–73. For description see opposite.

Facing p. 62

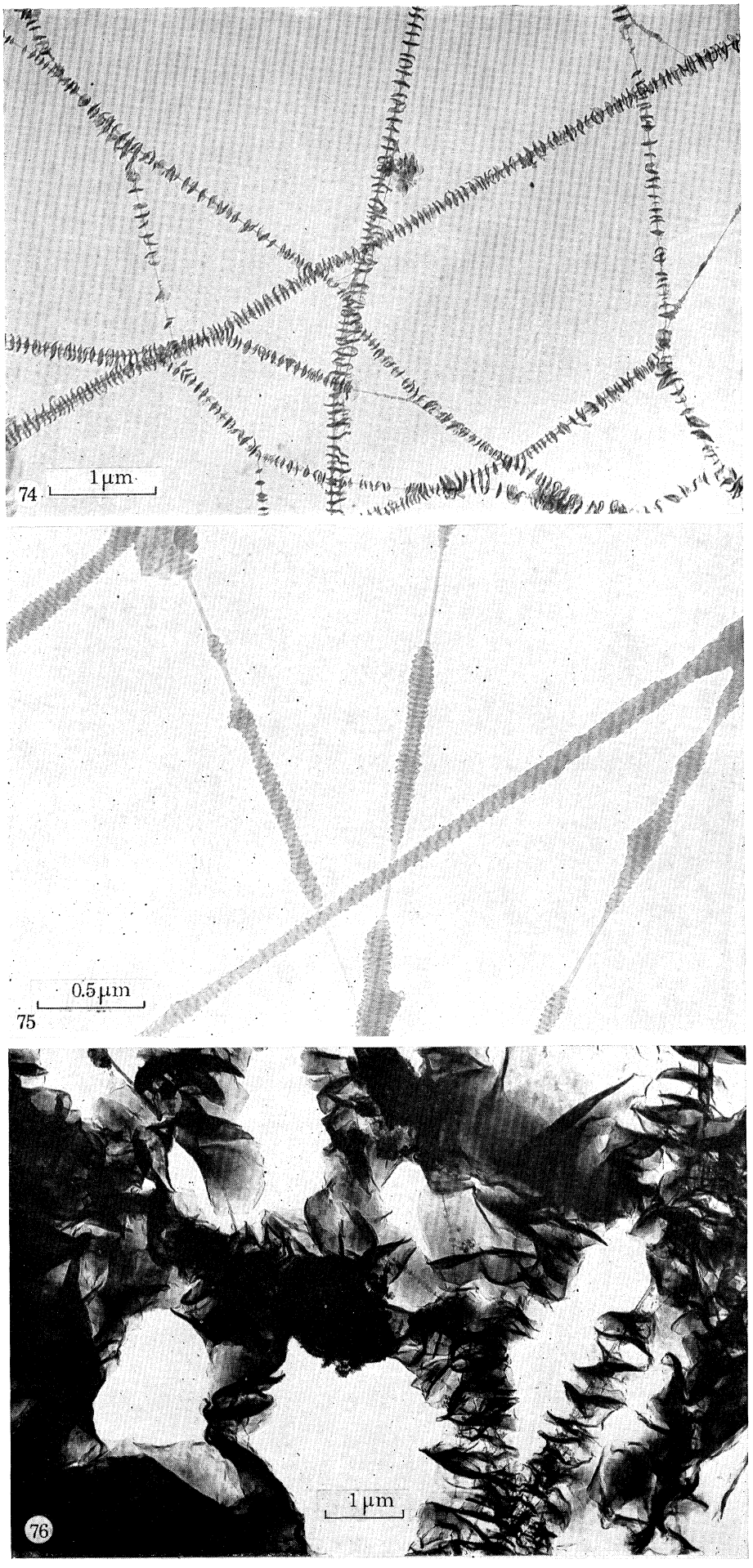

FIGURES 74–76. For description see opposite.

than 0.01 % of the xylene originally transferred from the crystallizing bath. It was considered that at this stage the solute material had been reduced to negligible proportions.

The crystals used for morphological studies were obtained under the following conditions. Crystallization temperature was 103 °C, solution concentration 1.5 %. The jets were operated in the sucking mode with a jet separation of 2 mm and jet entry velocity of 0.9 m/s. As seen in figure 67 the birefringence produced by these flow conditions, i.e. above the temperature where crystallization sets in, is close to the maximum achievable value and by the argument laid out in § 7 corresponds to that of the fully alined chain. Figures 71 and 73, plate 11, show the crystals for Rigidex and Hostalen respectively. Figure 72, plate 11, is an enlarged area of figure 71.

The most conspicuous feature in figures 71 and 73 is the distinct fibre-platelet combination. Clearly we have a fibrous backbone with platelets strung along them. The platelets are more prominent in figure 71, while conversely there is more material in the backbone fibre in figure 73. This is the characteristic shish-kebab morphology. In many places connective veils first observed by Keller & Machin (1967) are also discernible as shown by the enlarged detail of figure 74, plate 12.

The method described above enabled the linking of the results on chain alinement with the resulting morphology and hence is the principal one in the context of the present section. In morphological work for its own sake, however, it has some practical disadvantages. The process of crystal collection is an ill defined procedure and 'dispersed' samples are obtained by chance. For this reason a more convenient method was designed for further work on the morphology.

A fine grid is mounted edgewise on a cylindrical stirrer in such a way that the liquid has to pass through the meshes as the stirrer rotates. When immersed in a solution of polyethylene in xylene held somewhat above 97 °C fibrous precipitate forms attached to the meshes of the grid even on *slow* rotation of the stirrer (20 rev/min). This procedure differs from that of the usual 'stirring experiment' in that no turbulence is involved with the slow stirring speeds. The elongational flow required for the nucleation of the crystals should arise in two ways at two, potentially different localities. (1) The holes in the grid will act as single jets producing acceleration and deceleration of flow at entry and exit respectively. (2) There will be localities of zero velocity behind the solid bars, hence there must be longitudinal velocity gradients acting downstream of the grid immediately behind each of the grid bars. The longitudinal component of the velocity gradient, such as present, proved to be sufficient to induce fibrous crystallization. In addition to its simplicity the method has the decisive practical advantage that the fibres are individually dispersed and are directly available for examination in the state as formed on the same grids which are to be used in the electron microscope.

Figure 74, plate 12, illustrates the most typical form of fibrous crystal obtained from the rotating grid experiment. Figure 75, plate 12, illustrates another form of morphology which was seen less frequently on the same grid as above but in a different region. Figure 76, plate 12, illustrates the morphology seen if the sample is not washed after crystallization.

DESCRIPTION OF PLATE 12

FIGURE 74. Electron micrograph of shish kebabs observed by grid flow.

FIGURE 75. Electron micrograph of shish kebabs observed by grid flow.

FIGURE 76. Electron micrograph of unwashed shish kebabs exhibiting extensive overgrowths.

(b) Discussion

Extensive morphological studies have been made on shish kebabs, for example Keller & Willmouth (1972) and Pennings, van der Mark & Kiel (1970). In figure 76 the dimensional hierarchy discussed in Keller & Willmouth (1972) is clearly demonstrated for unwashed samples; here large lamellar platelets ($\approx$ 1–10 μm) are seen attached to a backbone which itself is of a composite shish kebab nature. Solvent washing can readily remove a large part of this overgrowth as shown in figures 71, 73 and 74 leaving the intrinsic flow-induced shish kebab structure. In no case however was it found possible to remove all the lamellar platelets overgrowth from the fibrous backbone by washing; it was therefore concluded that the remaining lamellar overgrowth must in some way be molecularly connected to the backbone (a conclusion also reached by Krueger & Yeh (1972)).

It was also noted that in both crystal growth preparations shish kebab backbones could apparently grow indefinitely in length, however, their lateral growth was limited; in the case of Rigidex type 2 to a diameter of about 20 nm and in the case of Hostalen GUR to about 25 nm.

Finally, figures 74 and 75 illustrate two examples of different morphologies found on the same grid. Figure 74 illustrates the open shish kebab structure typically observed by Pennings *et al.* (1970) while figure 75 illustrates the more compact striated type fibre observed by Keller & Willmouth (1972).

Undoubtedly the most surprising result when considered with the conditions under which the fibres were grown is that shown in figures 71 and 73 where we see a crystal of a composite shish kebab structure which has been grown in an environment where according to the conclusions of § 7 the molecules are extended and parallel to one another. Also it appears remarkable that crystals grown in both the preparations discussed in this section should have the same basic appearance as shish kebabs grown in turbulent flow.

From these results we conclude that the basic morphological features of the shish kebab is rather insensitive to the nature of the external flow field in which it is grown which contrasts with the findings of the previous sections where the nucleation of fibrous crystals was found to be highly dependent on the applied flow field.

Concerning nucleation in the opposed jet experiment, we observe nucleation taking place in a region where molecules are both alined parallel to one another and extended; presumably if the supercooling is sufficiently large these alined molecules would aggregate forming a fibrous crystal nucleus. This would be the first part of the central backbone shown in figure 71. There will be a minimum stable diameter for this crystal governed by the criterion that the work required for the creation of a crystal surface has to be balanced by the decrease in free energy due to the formation of the corresponding volume of crystal. For a cylindrical thread which is very much longer than broad, so that the end surfaces can be neglected, this criterion will be satisfied for a radius r_x when $2\pi r_x \sigma = \pi r_x^2 \Delta f$, i.e., $r_x = 2\sigma/\Delta f$. Here σ is the lateral surface free energy and Δf the bulk free energy expressible to a good approximation as $(\Delta H)(\Delta T)/T_m^0$ (T_m^0 is the melting or dissolution temperature of the infinitely extended chain crystal, $\Delta T = T_m^0 - T_c$ is the supercooling, and ΔH the heat of fusion). Thus

$$r_x = 2\sigma T_m^0/(\Delta H)(\Delta T).$$

We may take $\sigma = 10^{-6}$ J/cm^2; $\Delta H = 280$ J/cm^3. As apparent from this work T_m^0 must be at least 112 °C, the highest temperature at which permanent crystallization could be achieved, but

claims of $T_m^0 = 118\,°C$ (in xylene) also exist (Jackson, Mandelkern & Long 1968). This uncertainty, while of negligible consequence through T_m^0 alone, significantly affects ΔT which for $T_c = 103\,°C$ (the value for figures 71–73) could encompass the range of 9–15 °C. We then obtain for the range of ΔT just quoted $r_x = 3$–$1.9\,nm$.

Typical values for the observed minimum central core radius are $r = 5$–$7.5\,nm$. This is well above the figure calculated above and the crystal fibres seen can thus be expected to be stable.

The above critical radius was calculated for crystallization from the quiescent state; however, for the experimental conditions used, when the fibres form, the chains are all alined. This means that the entropy (S) of the solution is reduced during flow, hence ΔS for crystallization will be correspondingly reduced. In this situation T_m^0 will be larger which will significantly enhance ΔT with ensuing reduction in r. Hence chain alinement increases the stability of the fibres; however it is to be expected by the same argument that crystals which are thinner than r_x for the quiescent solution will dissolve as flow ceases.

Concerning crystal growth we note that once the crystal has been nucleated by extensional flow, lateral growth of the backbone is limited in some way. Because this is quite general for shish kebabs grown under all conditions the mechanism controlling the growth cannot be due to the precise nature of the externally applied velocity gradient. One possible explanation for this limited lateral growth is that once the crystal has nucleated the dominant flow field affecting further crystal growth is the local flow field generated by streaming around the fibre and not the externally applied velocity gradient. In this way the local transverse velocity gradient developed on the side-surface of the crystal may prevent complete chain extension on the side-surface and hence prevent lateral growth. A quantitative treatment of the local flow field around the fibre is given in a separate publication (Mackley 1974).

To conclude: we have seen from the previous sections that factors affecting the nucleation of fibrous crystals are sensitive to the nature and magnitude of the applied velocity gradient, and also that nucleation is highly dependent on the amount of high molecular weight material present. From morphological observations we have established that chain extended crystallization by flow is a self-limiting process in the lateral direction even when the crystals are grown in a situation where all molecules are alined in the solution; also some chain folded platelets are necessarily an intrinsic part of the resulting structure. The proportion of the latter, however, can be reduced by increasing the molecular weight. Obviously these recognitions should be relevant to all efforts for obtaining fully extended chains by means of a flow field, an issue with many practical implications.

We would like to thank Professor F. C. Frank, F.R.S. for many useful suggestions on the work. One of us (M.R.M.) would like to thank the Science Research Council and later the Courtalds educational trust for financial support

References

Blundell, D. J. & Keller, A. 1968 *J. Macromol. Sci.* (*Phys.*) B 2 (**2**), 301–336.
Blundell, D. J., Keller, A. & Kovacs, A. J. 1966 *J. Polymer Sci.* B **4**, 481–486.
Bunn, C. W. & Daubeny, R. de P. 1954 *Trans. Farad. Soc.* **50**, 1173–1177.
Denbigh, K. G. 1940 *Trans. Farad. Soc.* **36**, 936–948.
Frank, F. C. 1970 *Proc. R. Soc. Lond.* A **319**, 127–136.
Frank, F. C., Keller, A. & Mackley, M. R. 1971 *Polymer* **12**, 467–473.
Hermans, J. J. 1944 *Physica* **10**, 777–789.
Hlavacek, B. & Seyer, F. A. 1971 *Kolloid Z. u. Z. Polymere* **243**, 32–41.
Jackson, J. F., Mandelkern, L. & Long, O. C. 1968 *Macromolecules* **1**, 218–223.
Katayama, K., Amano, T. & Nakamara, K. 1968 *Kolloid Z. u. Z. Polymere* **226**, 125–134.
Keller, A. 1958 Growth and perfection of crystals. *Proc. Int. Conf. on Crystal Growth, Cooperstown*, 499–528. New York: John Wiley.
Keller, A. 1968 *Rep. Prog. Phys.* **31**, part 2, 623–705.
Keller, A. & Machin. M. R. 1967 *J. macromol. Sci.* (*Phys.*) B **1**, 41–89.
Keller, A. & Willmouth, F. M. 1972 *J. macromol. Sci.* (*Phys.*) B **6**, 493–537.
Krueger, D. & Yeh, G. S. Y. 1972 *J. macromol. Sci.* (*Phys.*) B **6**, 3, 431–450.
Kuhn, W. & Kuhn, H. 1943 *Helv. Chim. Acta* **26**, 1394–1465.
Loitsyanski, L. G. 1966 Mech. of liquids and gases. Int. Series of monographs in *Aeronautics and astronautics*, div. II, *Aerodynamics*, vol. 6, 410–417. London: Pergamon Press.
Mackley, M. R. 1974 *Kolloid Z. u. Z. Polymere.* (In the press.)
McHugh, A. J. & Schultz, J. M. 1973 *Kolloid Z. u. Z. Polymere* **251**, 193–213.
Metzner, A. B. & Metzner, A. P 1970 *Rheol. Acta* **9**, 174–181.
Pechold, W. 1971 *J. Polymer Sci.* C **32**, 123–147.
Pennings, A. J. 1966 *Crystal growth, Proc. Int. Conf. Boston*, 389–393. Oxford: Pergamon Press.
Pennings, A. J. & Kiel, A. M. 1965 *Kolloid Z. u. Z. Polymere*, **205**, 160–162.
Pennings, A. J., van der Mark, J. M. A. A. & Booij, H. C. 1970 *Kolloid Z. u. Z. Polymere* **236**, 99–111.
Pennings, A. J., van der Mark, J. M. A. A. & Kiel, A. M. 1970 *Kolloid Z. u. Z. Polymere* **237**, 336–358.
Peterlin, A. 1967 *Polymer* **2**, 257–264.
Peterlin, A. 1966 *J. Polymer Sci.* B **4**, 287–290.
Taylor, G. I. 1934 *Proc. R. Soc. Lond.* A **146**, 501–523.
Treloar, L. R. G. 1949 *Physics of rubber elasticity*, 54. Oxford University Press.
Volkenstein, M. V. 1963 *Configurational statistics of polymeric chains*, 391–398. New York: Interscience.
Ziabicki, A. 1959 *J. appl. Polymer Sci.* **11** (4), 14–23.

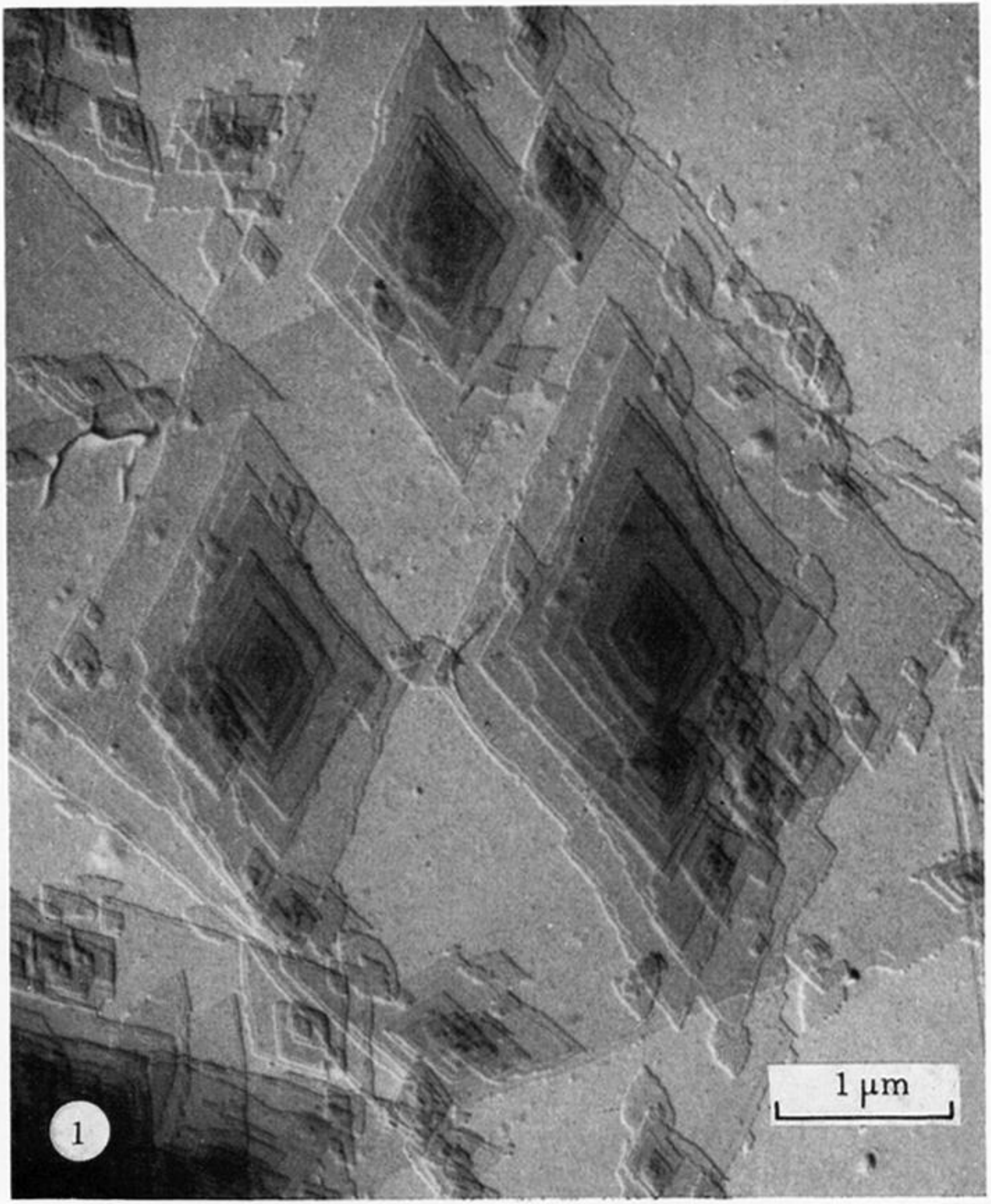

FIGURE 1. Typical chain folded crystal (Keller 1958).

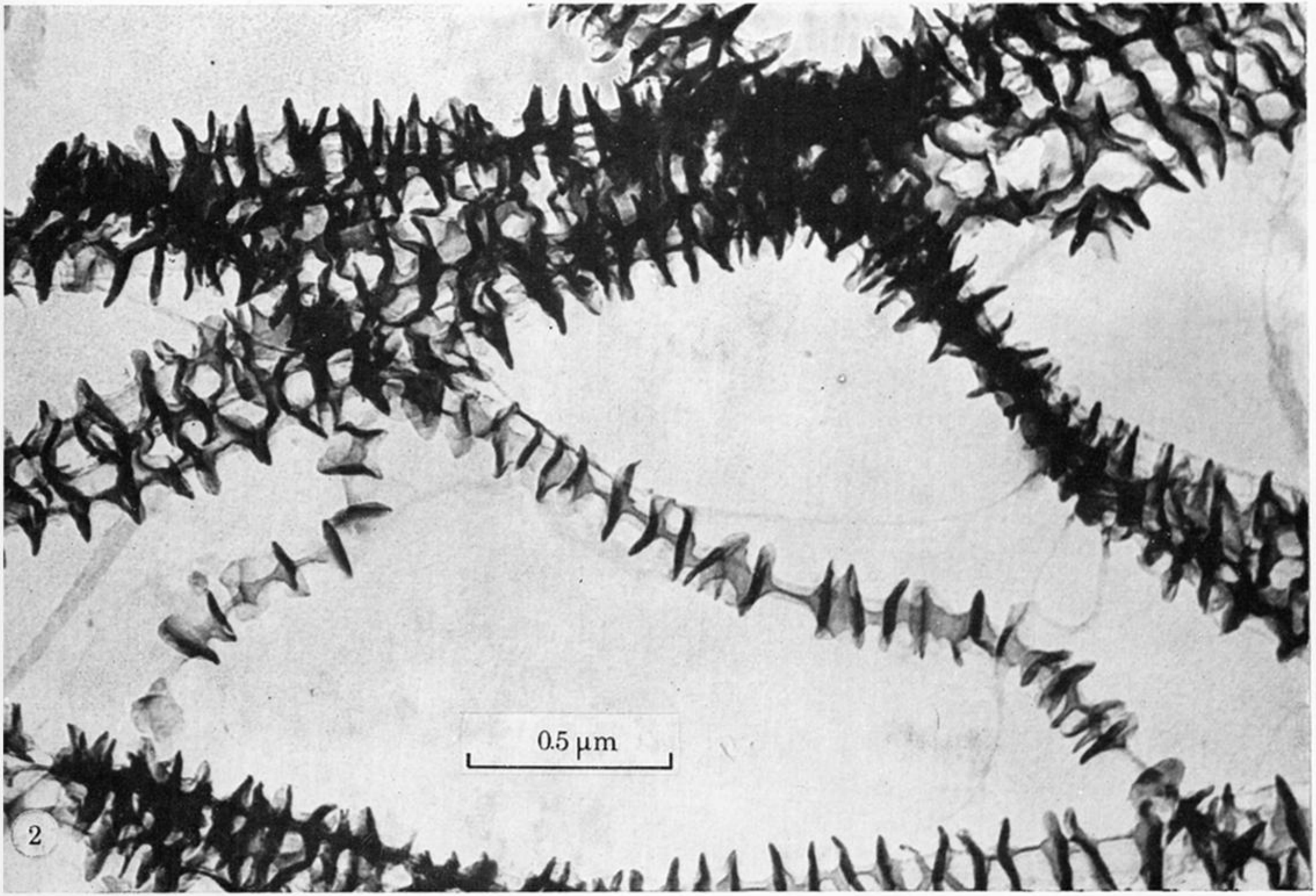

FIGURE 2. A standard shish kebab (after Pennings 1966).

FIGURE 4. Sectional view of Taylor vortices illuminated by a planar radial light beam. (Gap between cylinders, 1 cm.)

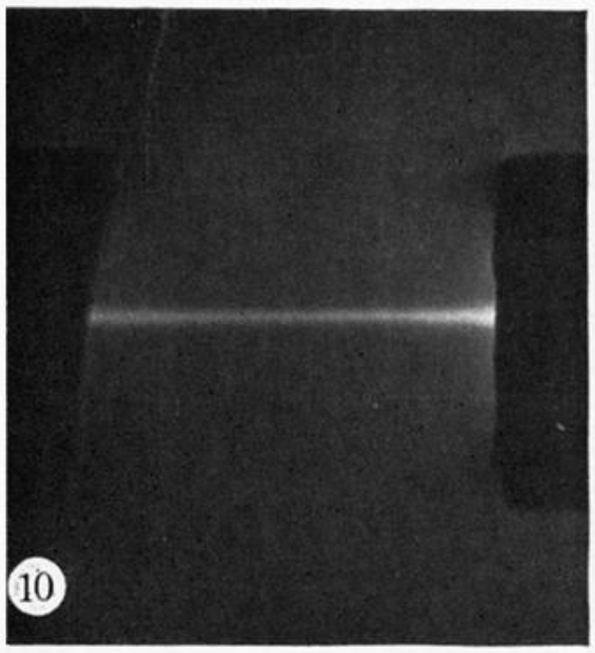

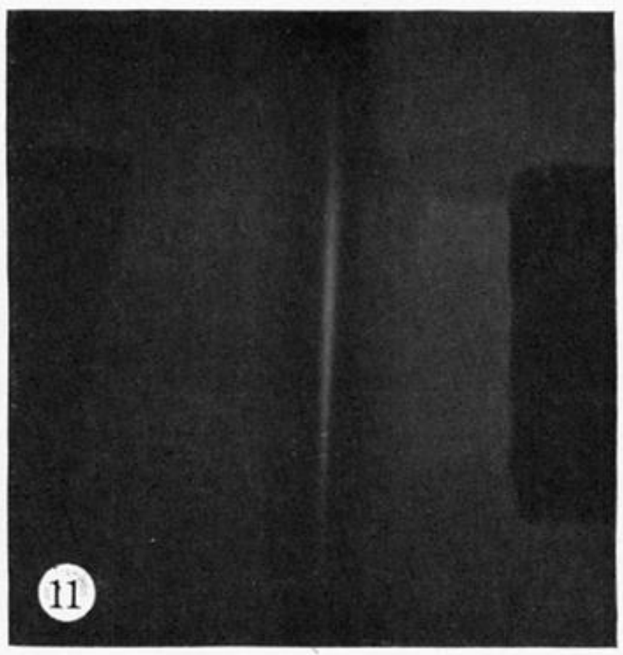

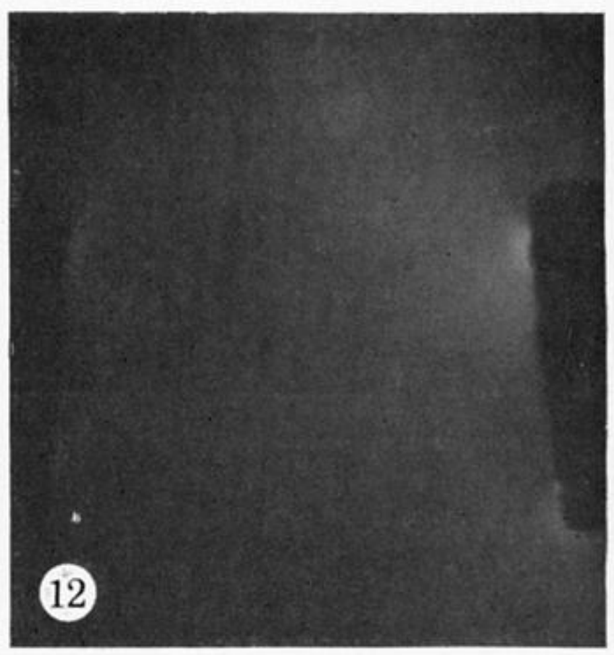

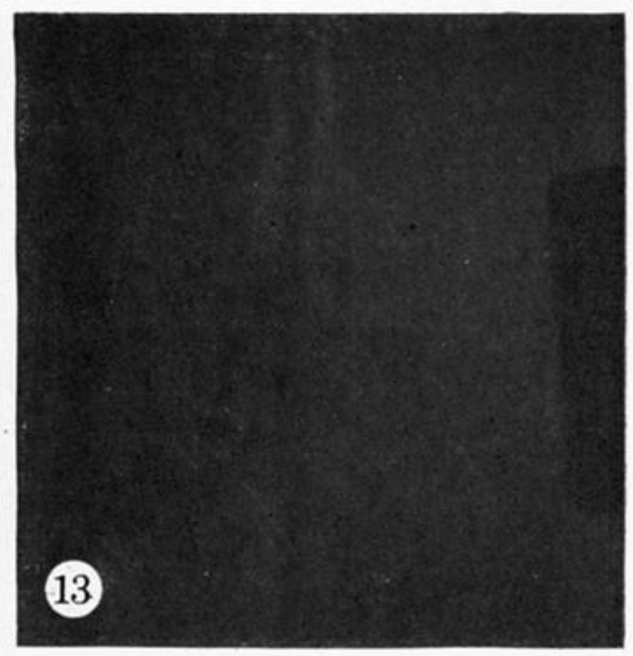

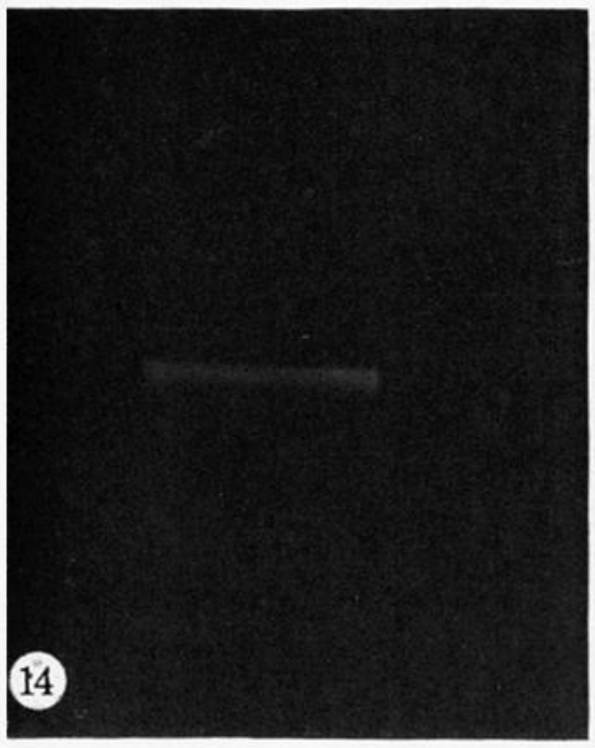

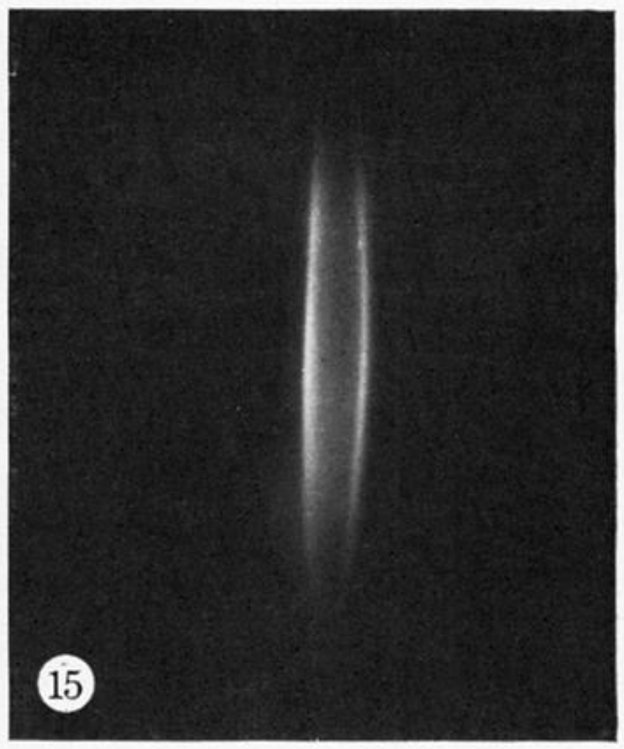

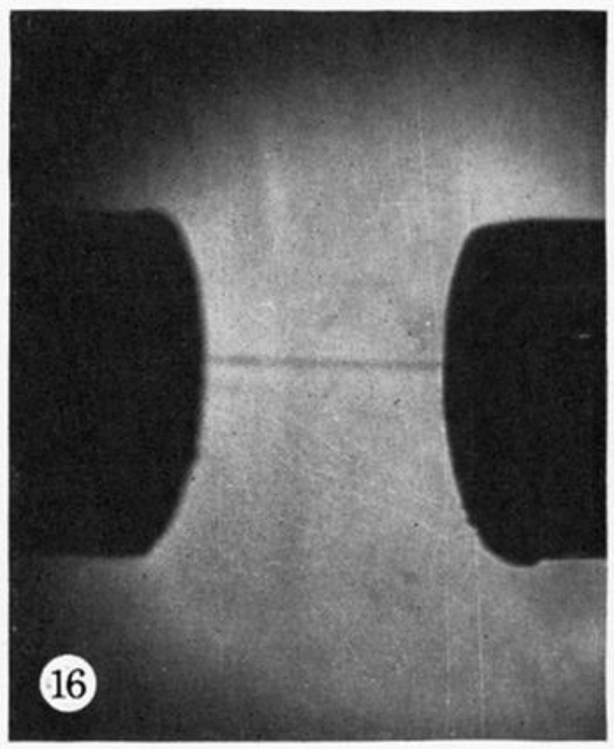

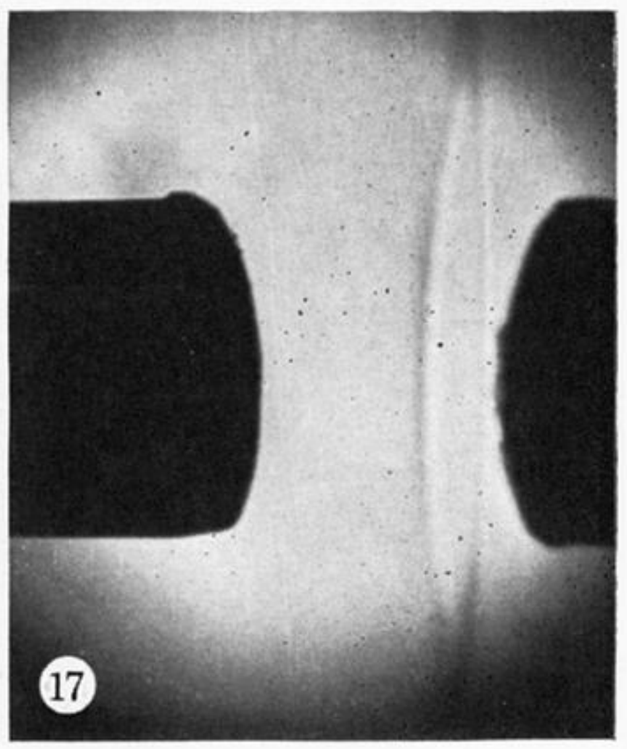

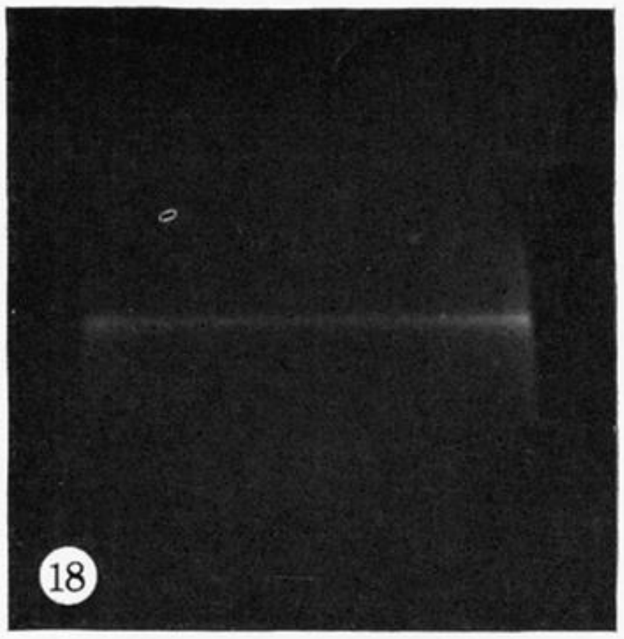

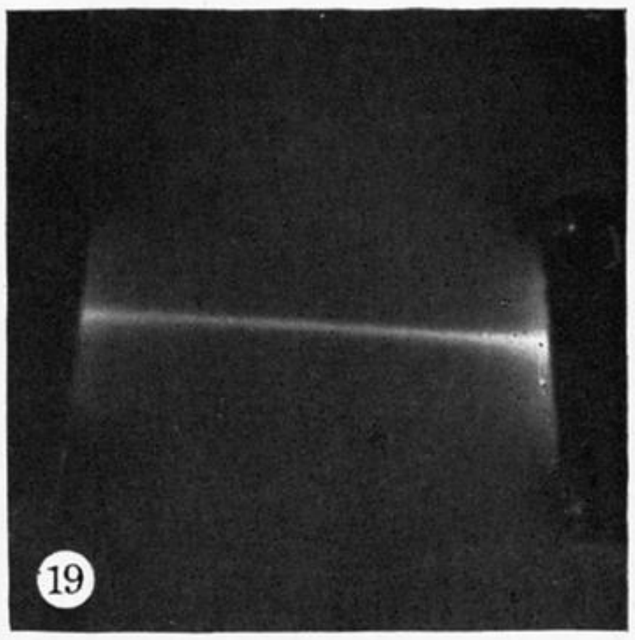

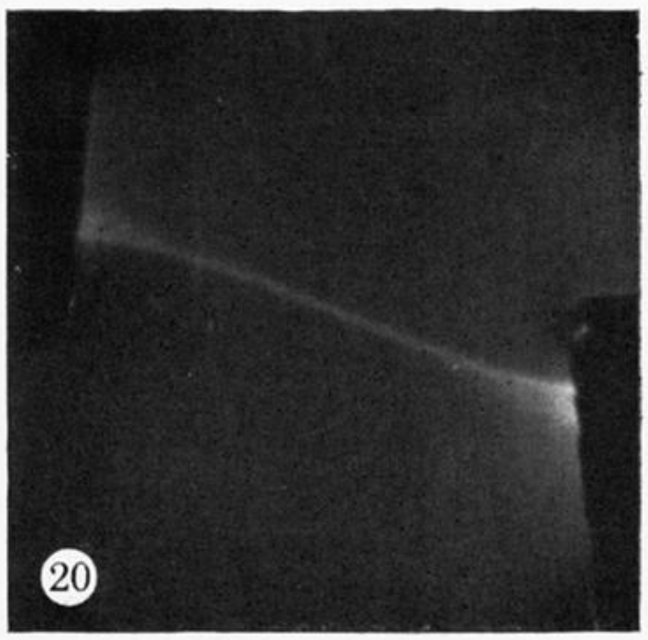

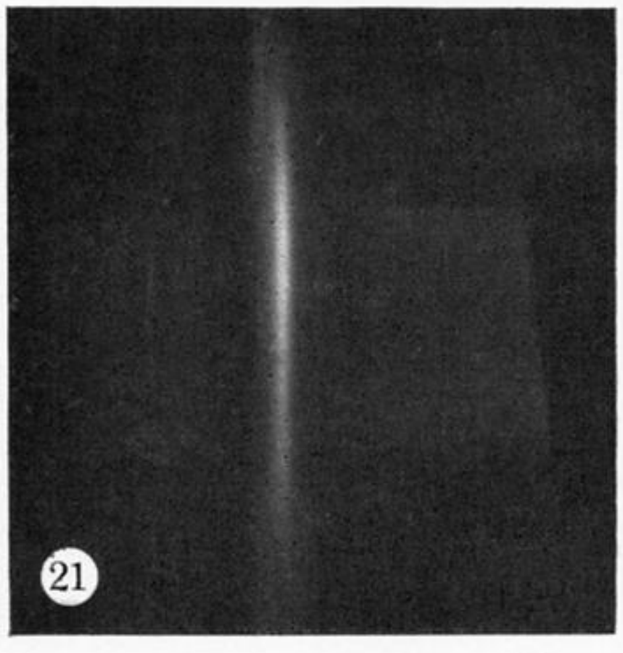

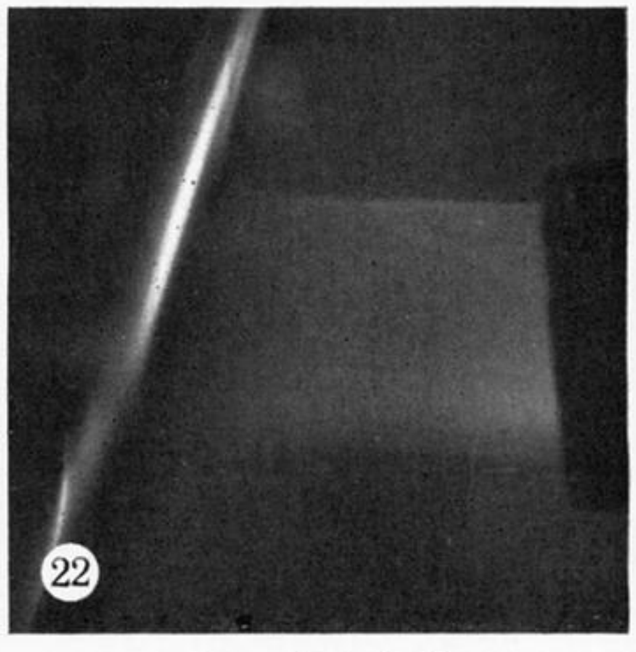

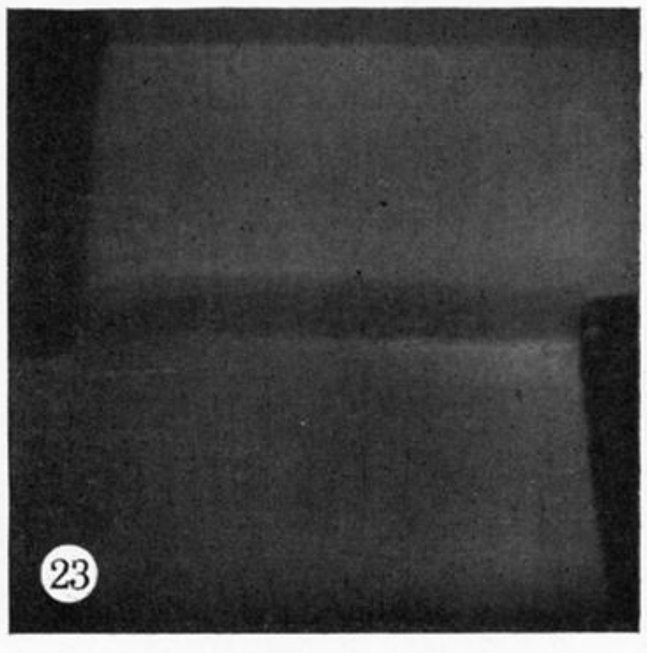

FIGURES 10–23. For description see opposite.

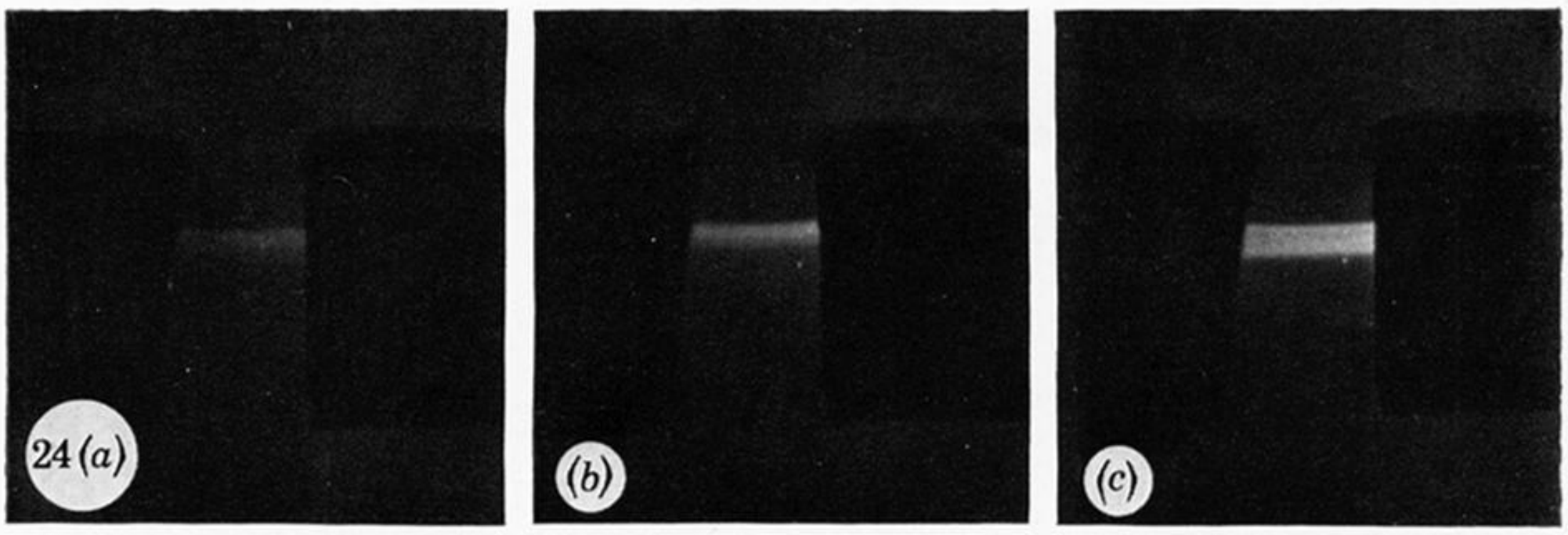

FIGURES 24–26. The development of birefringence for increasing jet velocity and jet separation. See table 1 for details.

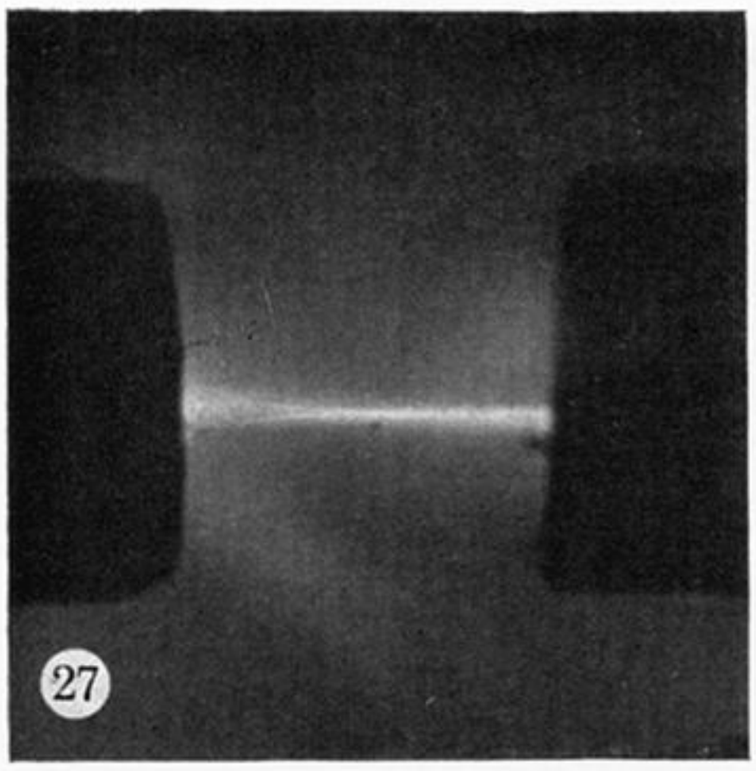

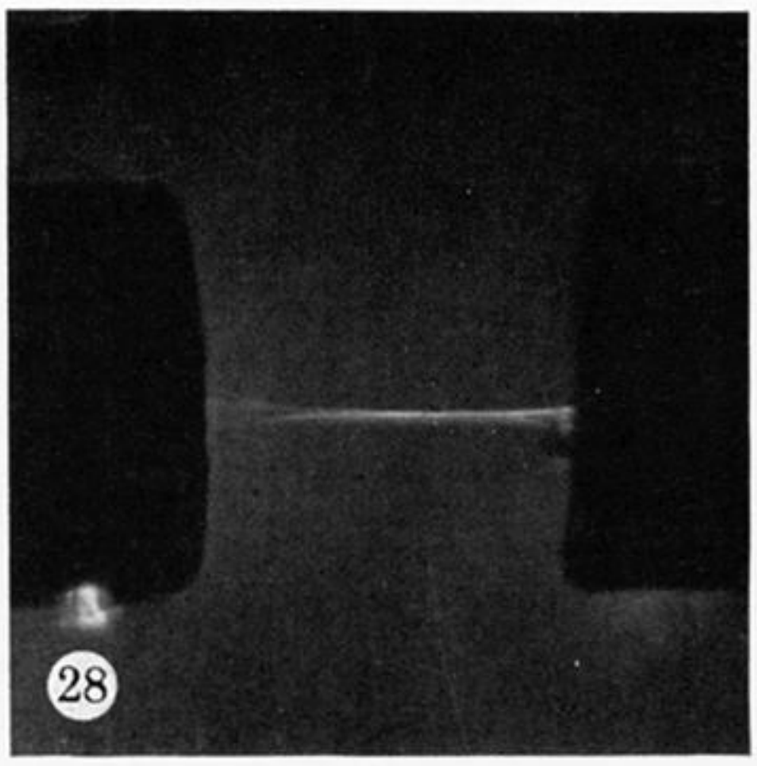

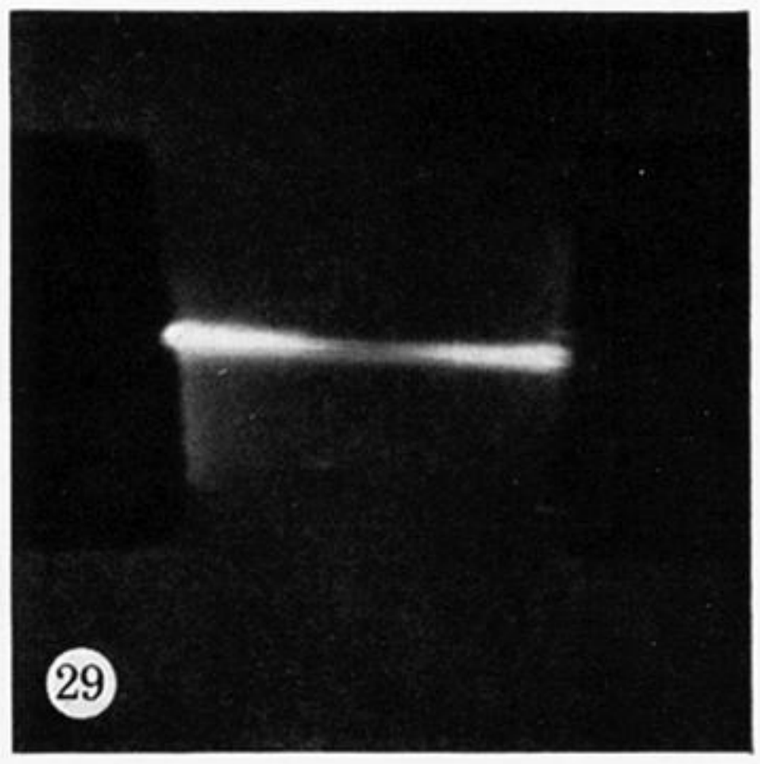

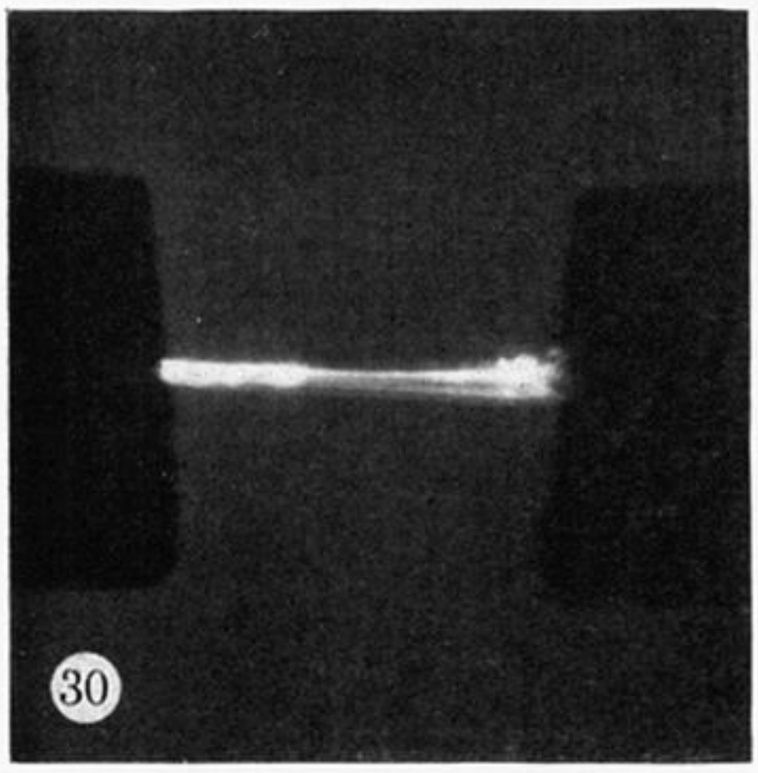

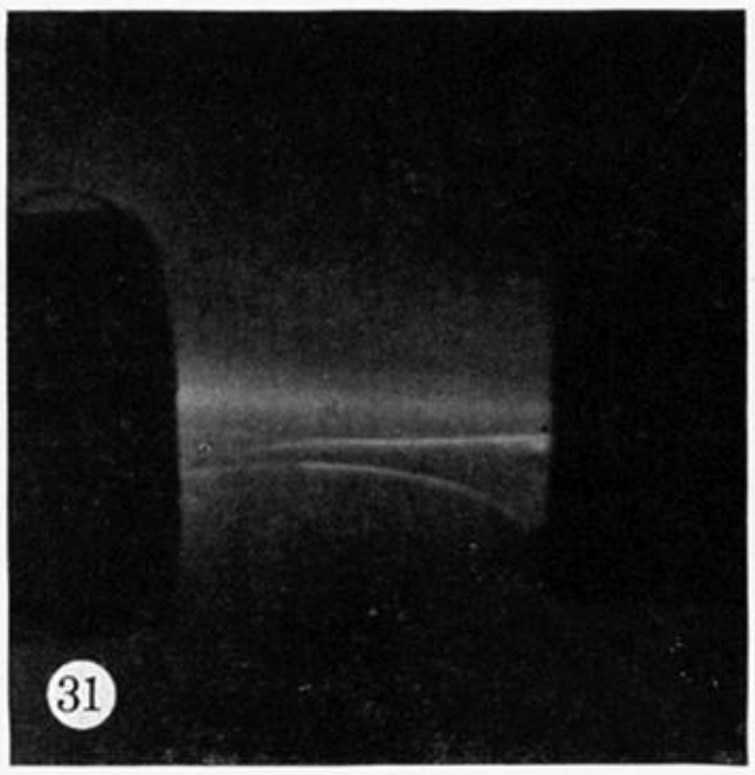

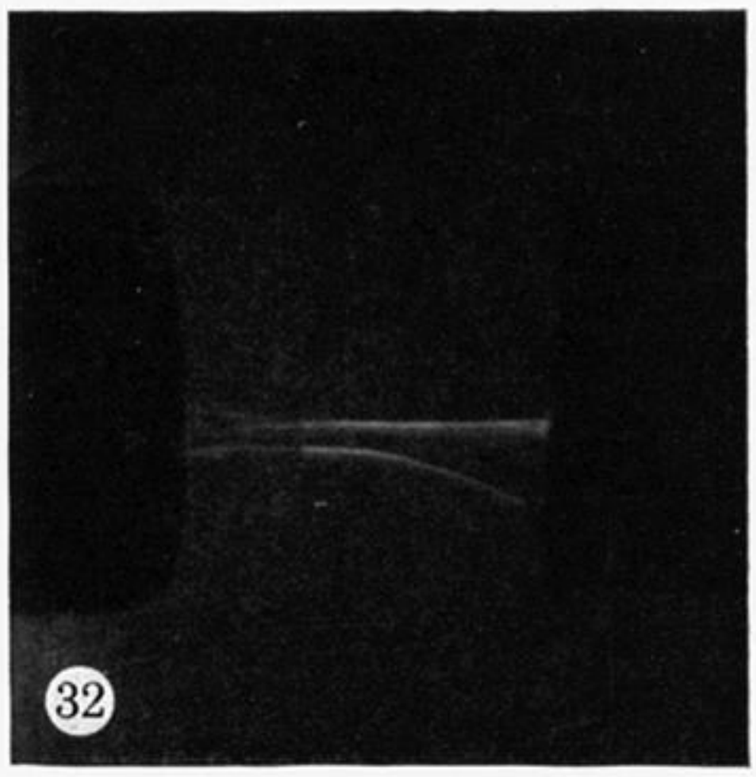

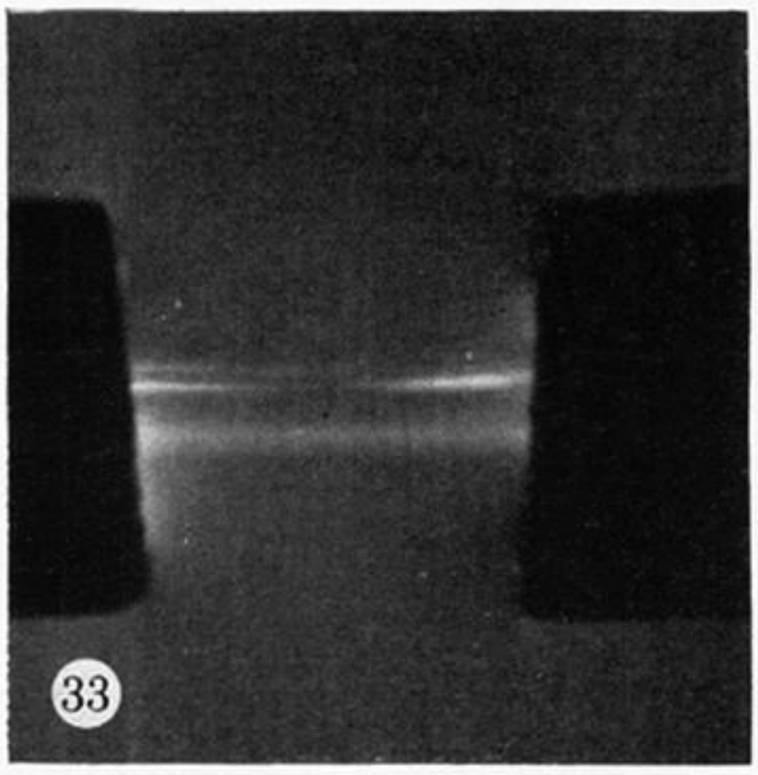

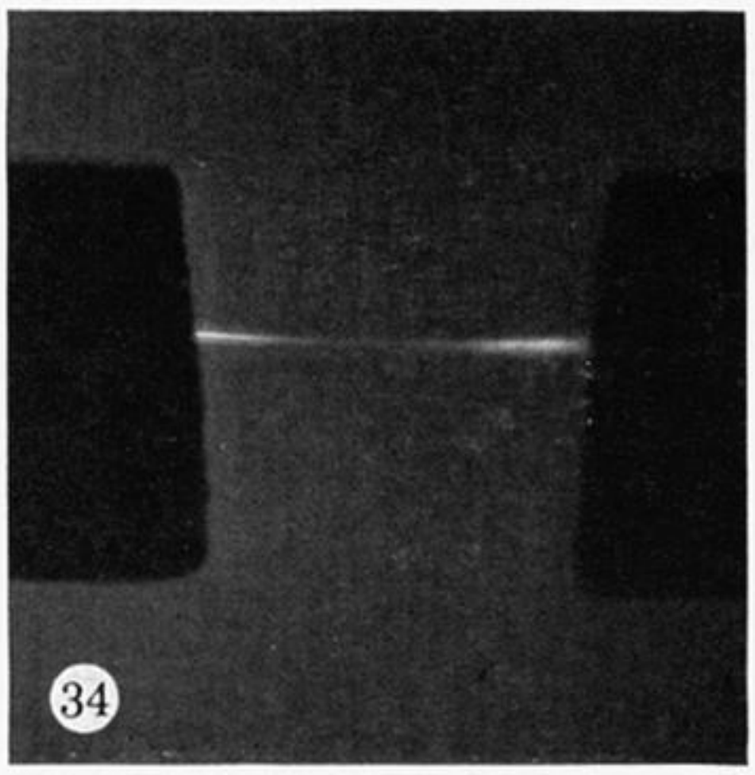

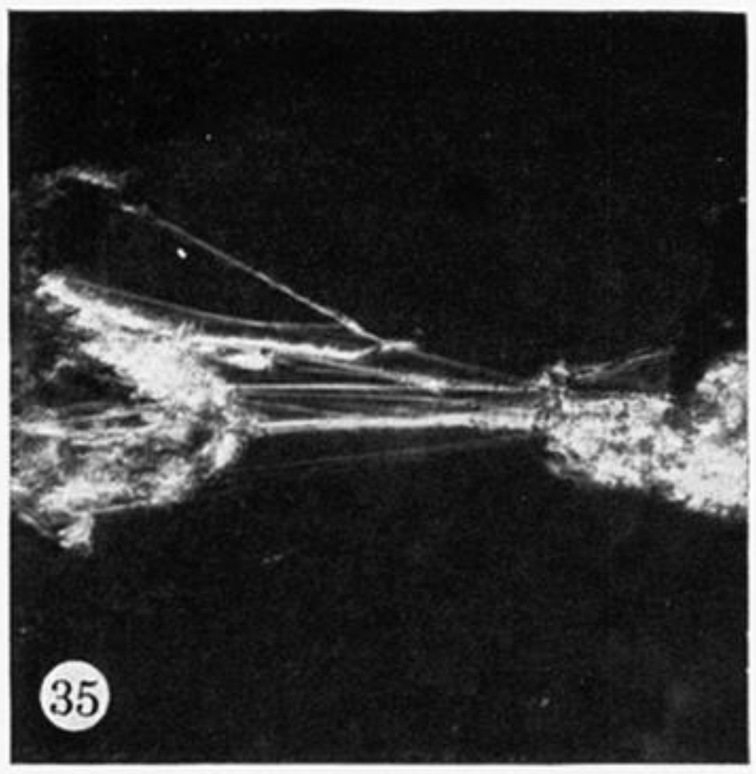

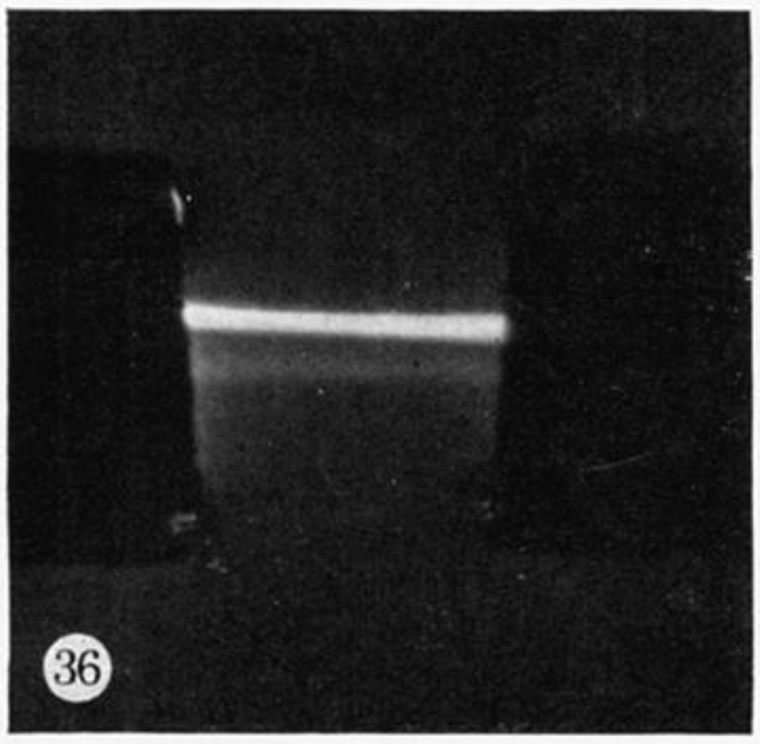

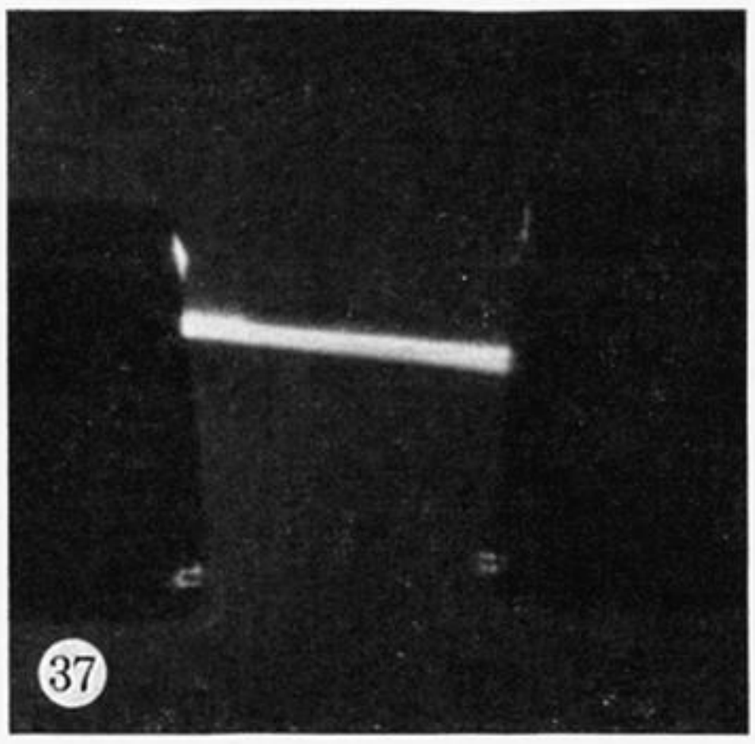

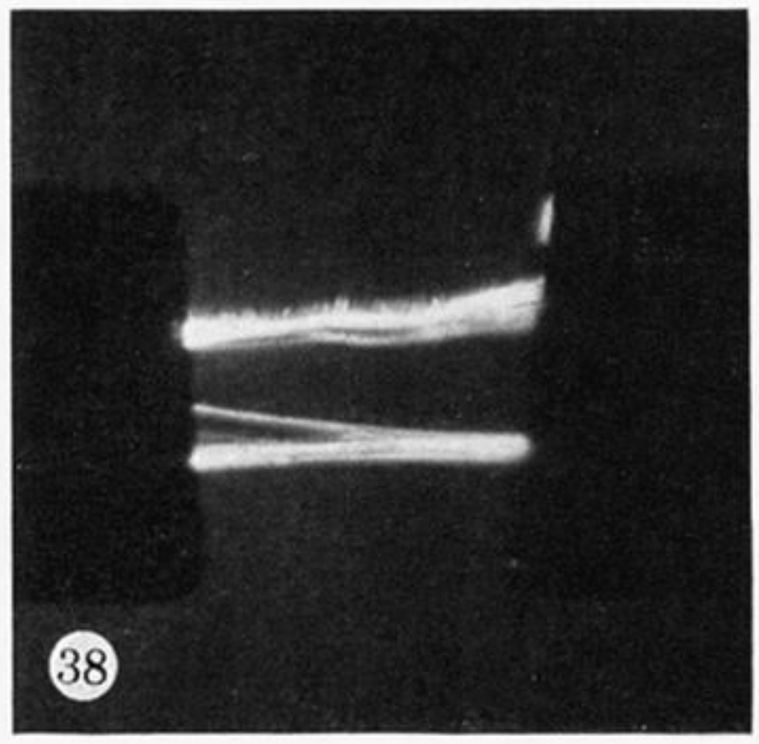

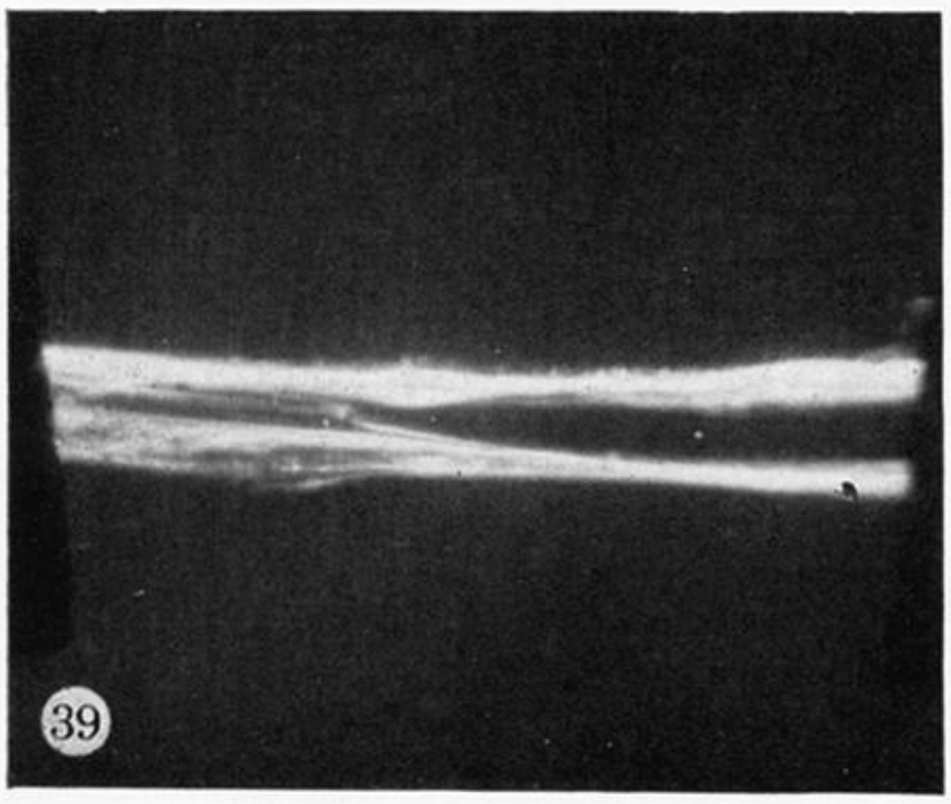

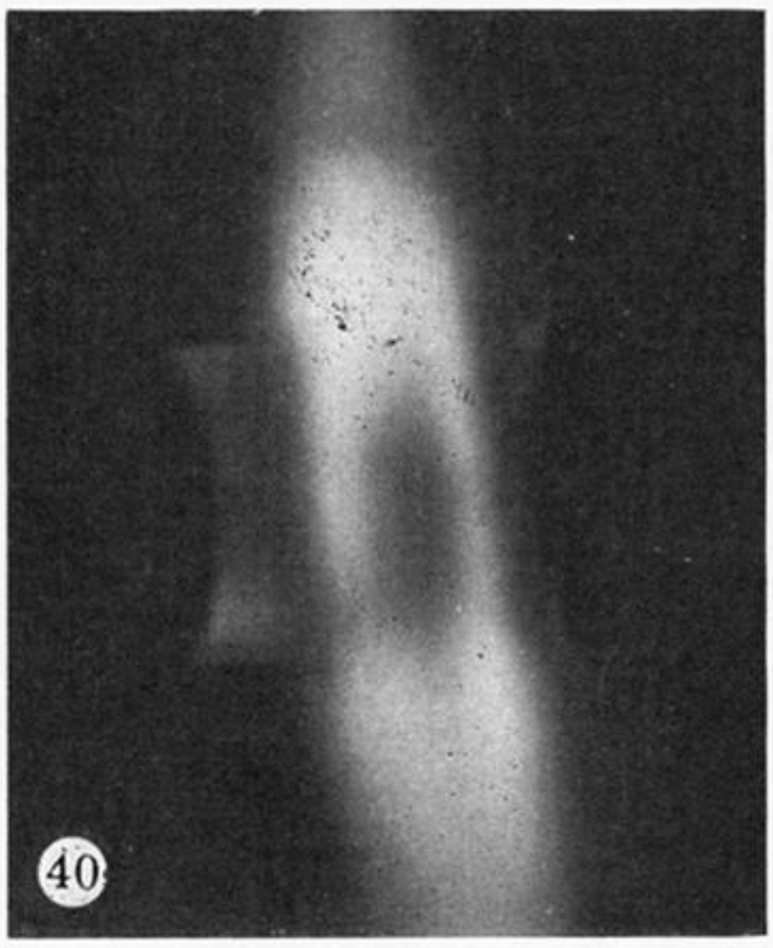

FIGURES 27–41. For description see opposite.

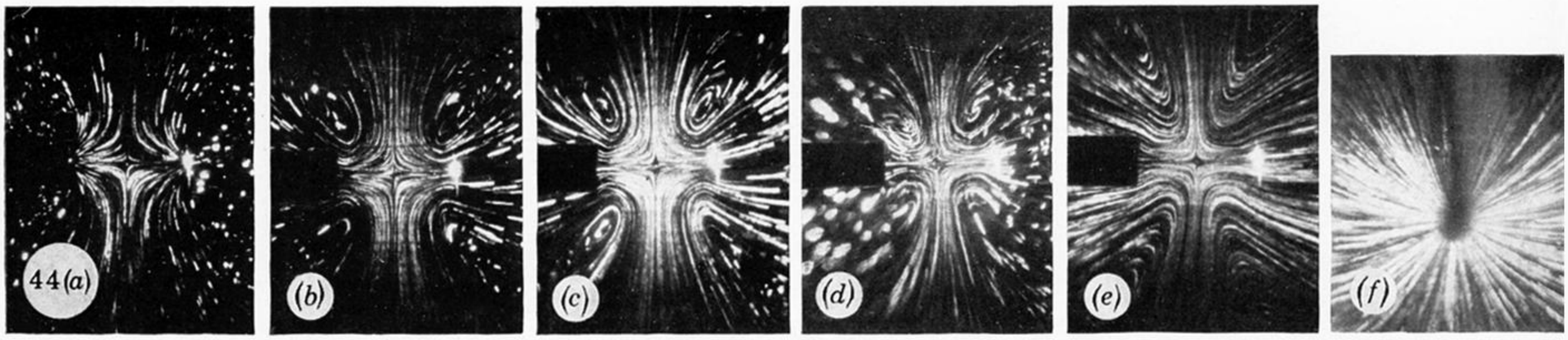

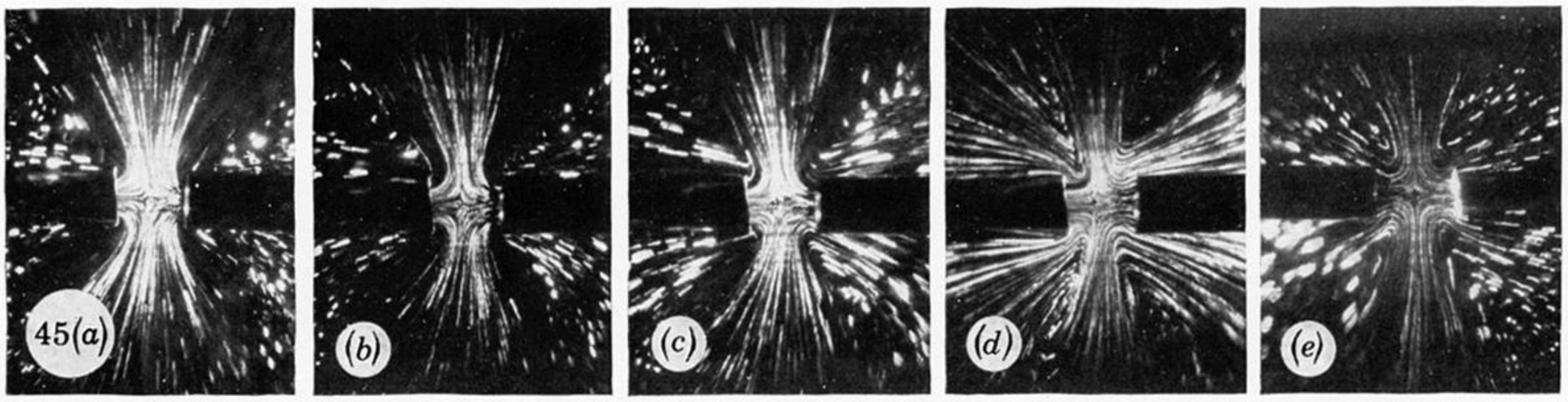

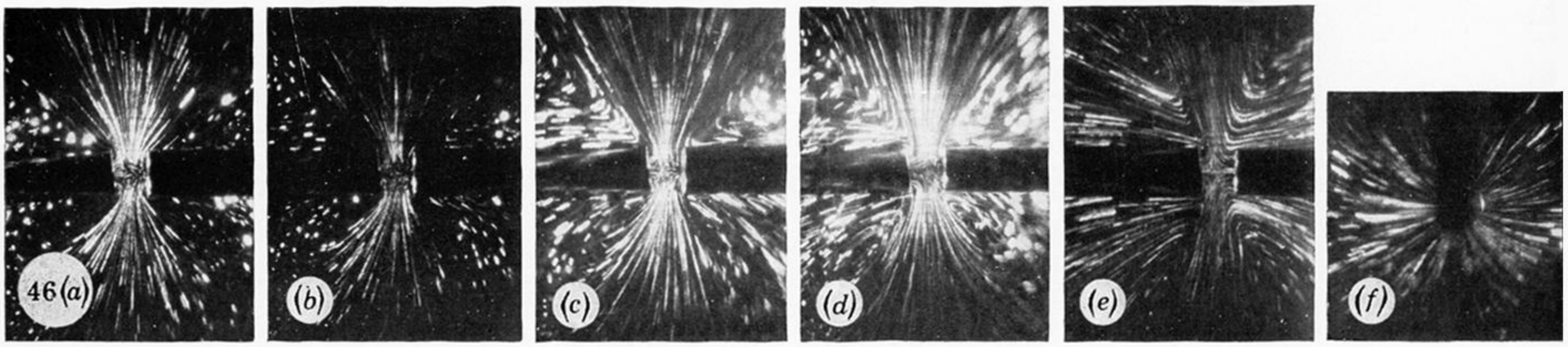

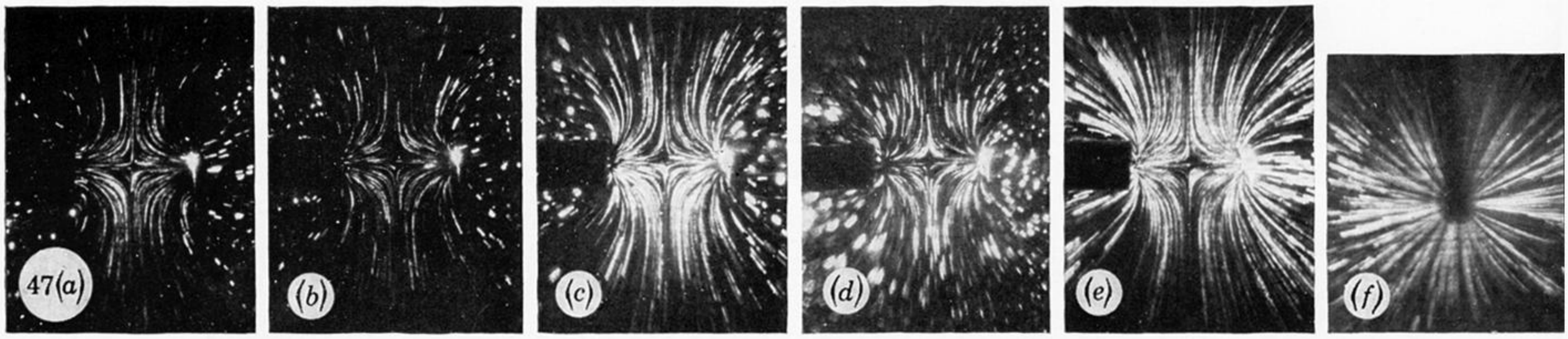

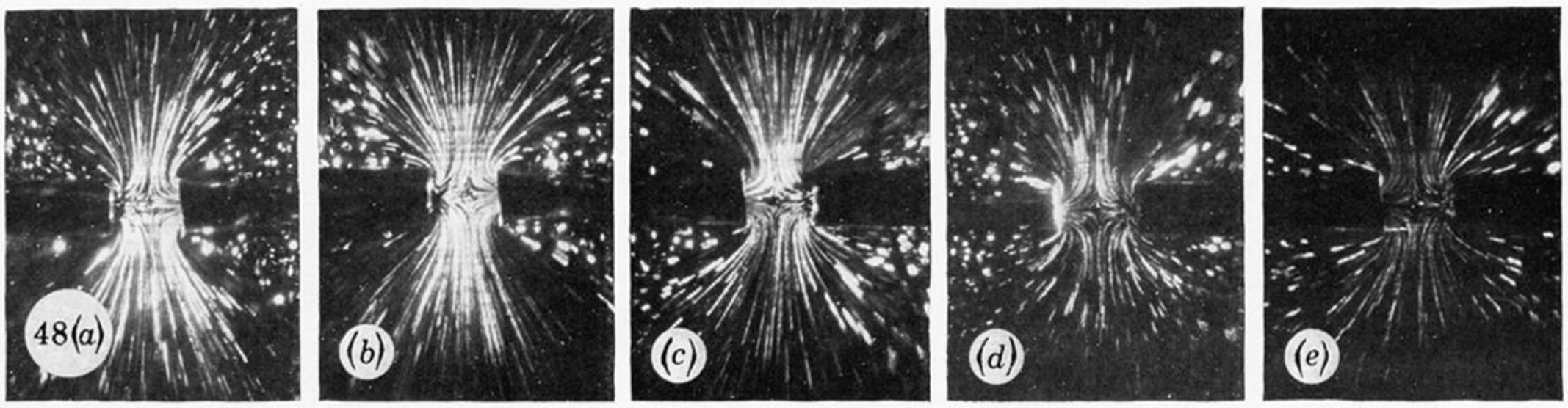

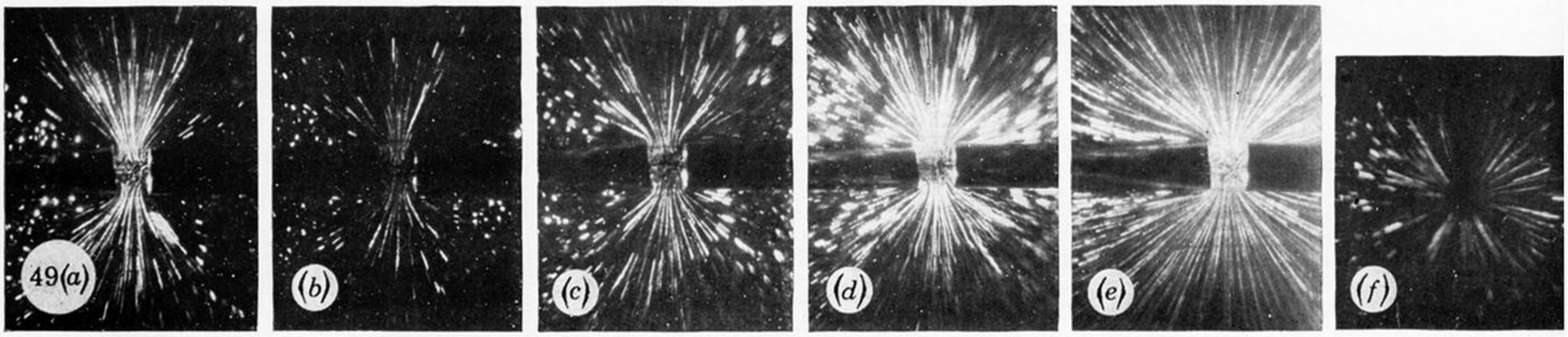

FIGURES 44–46. Streamline photographs for case of blowing (see table 2).

FIGURES 47–49. Streamline photographs for case of suction (see table 3).

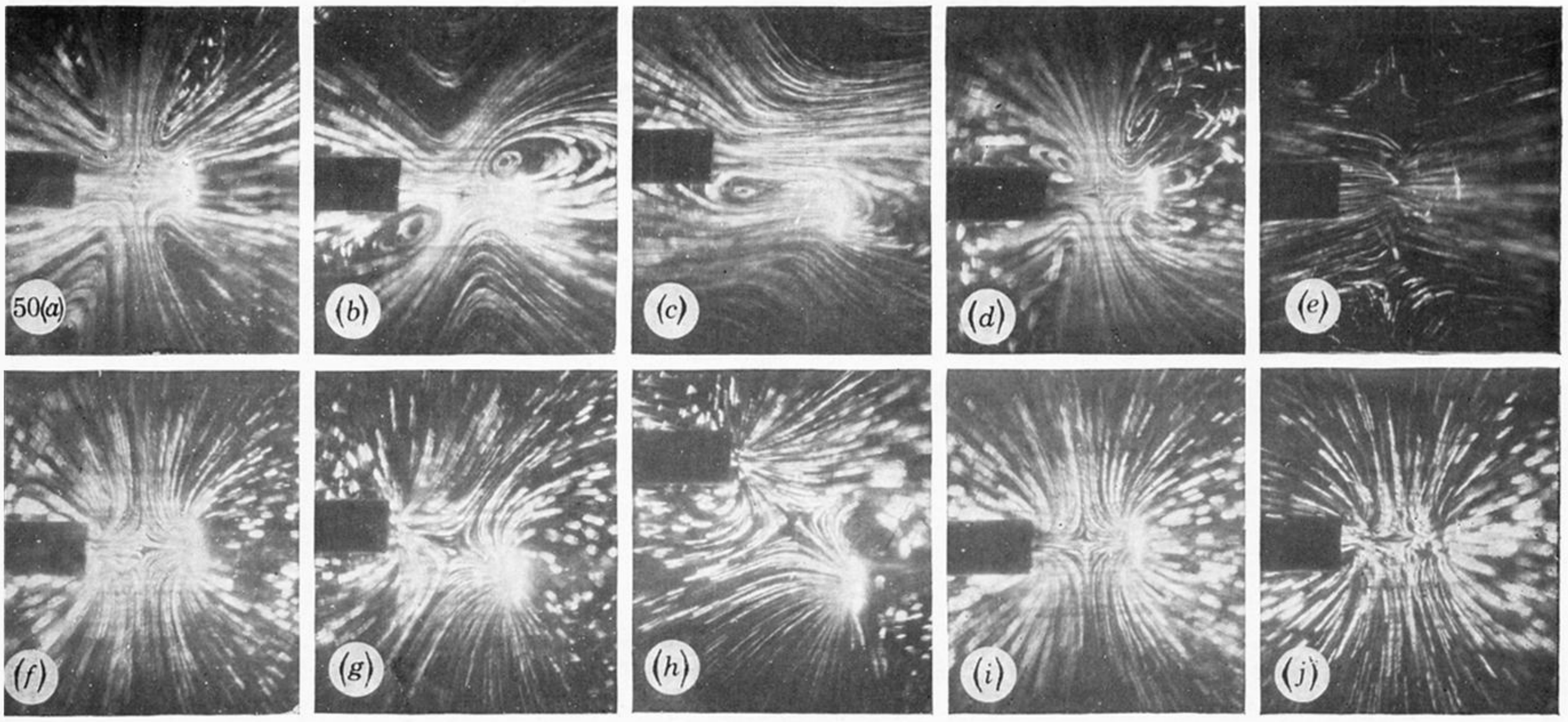

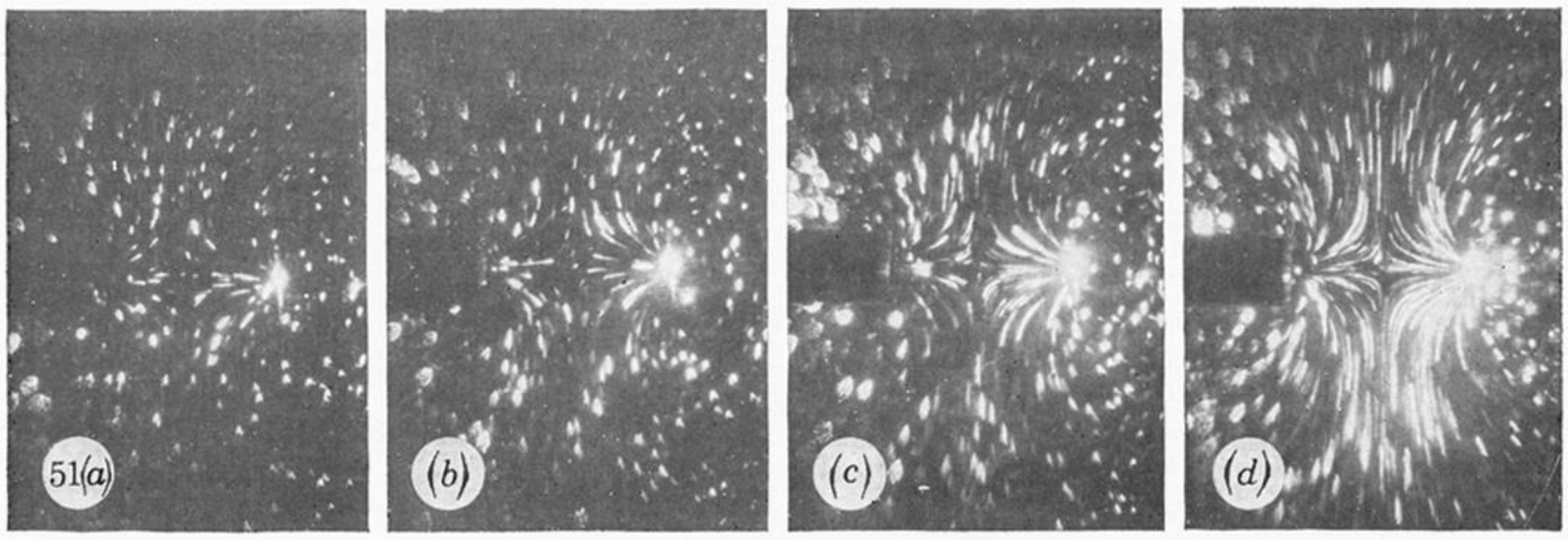

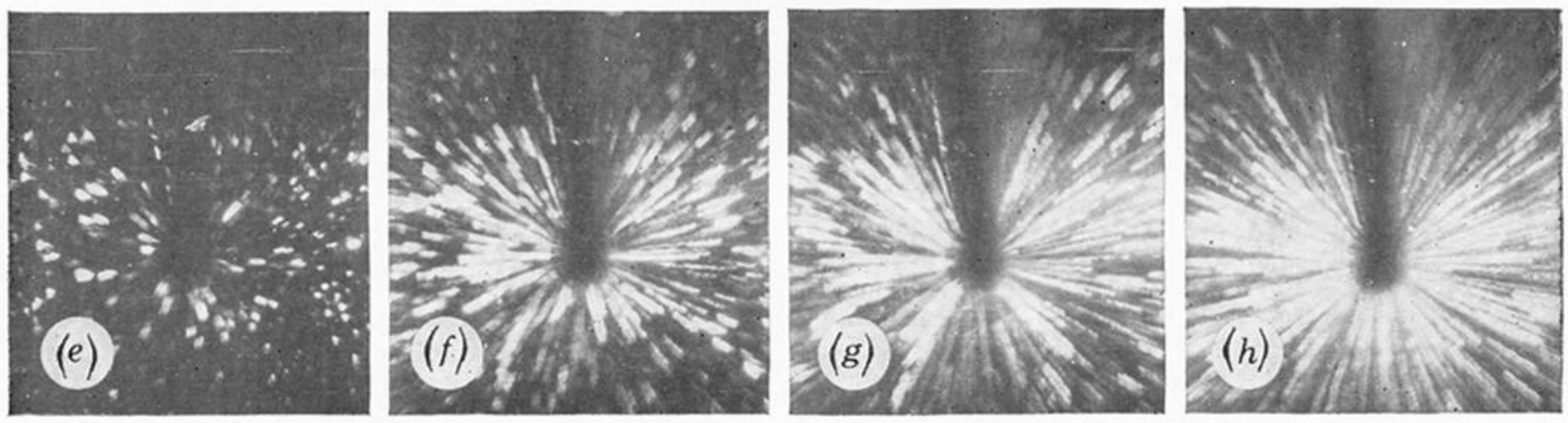

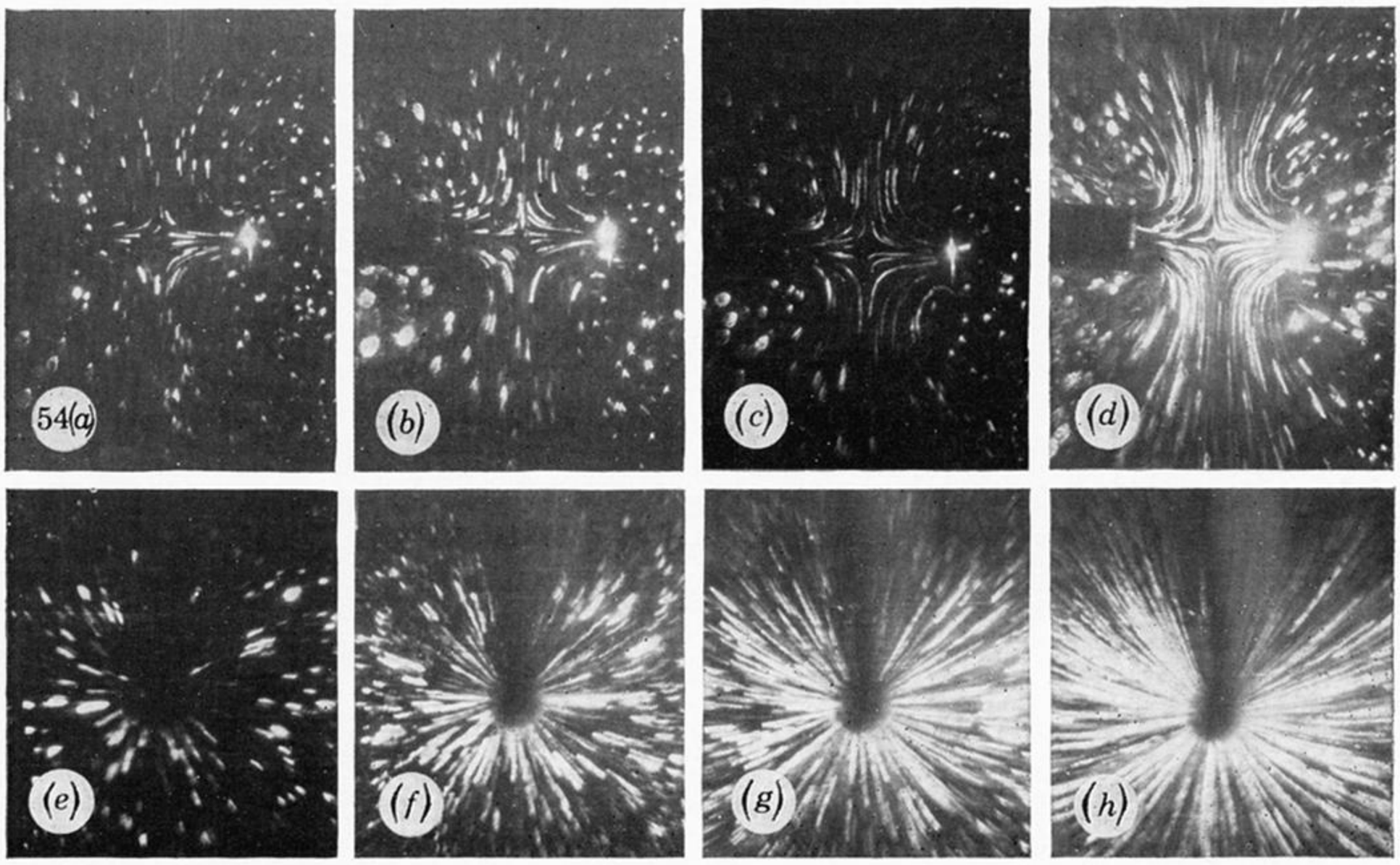

FIGURE 50. Photographs showing the effect of misalinement for sucking and blowing (see table 4).

FIGURE 51. Point velocity photographs for the case of blowing (see table 5).

FIGURE 54. Point velocity photographs for the case of sucking (see table 6).

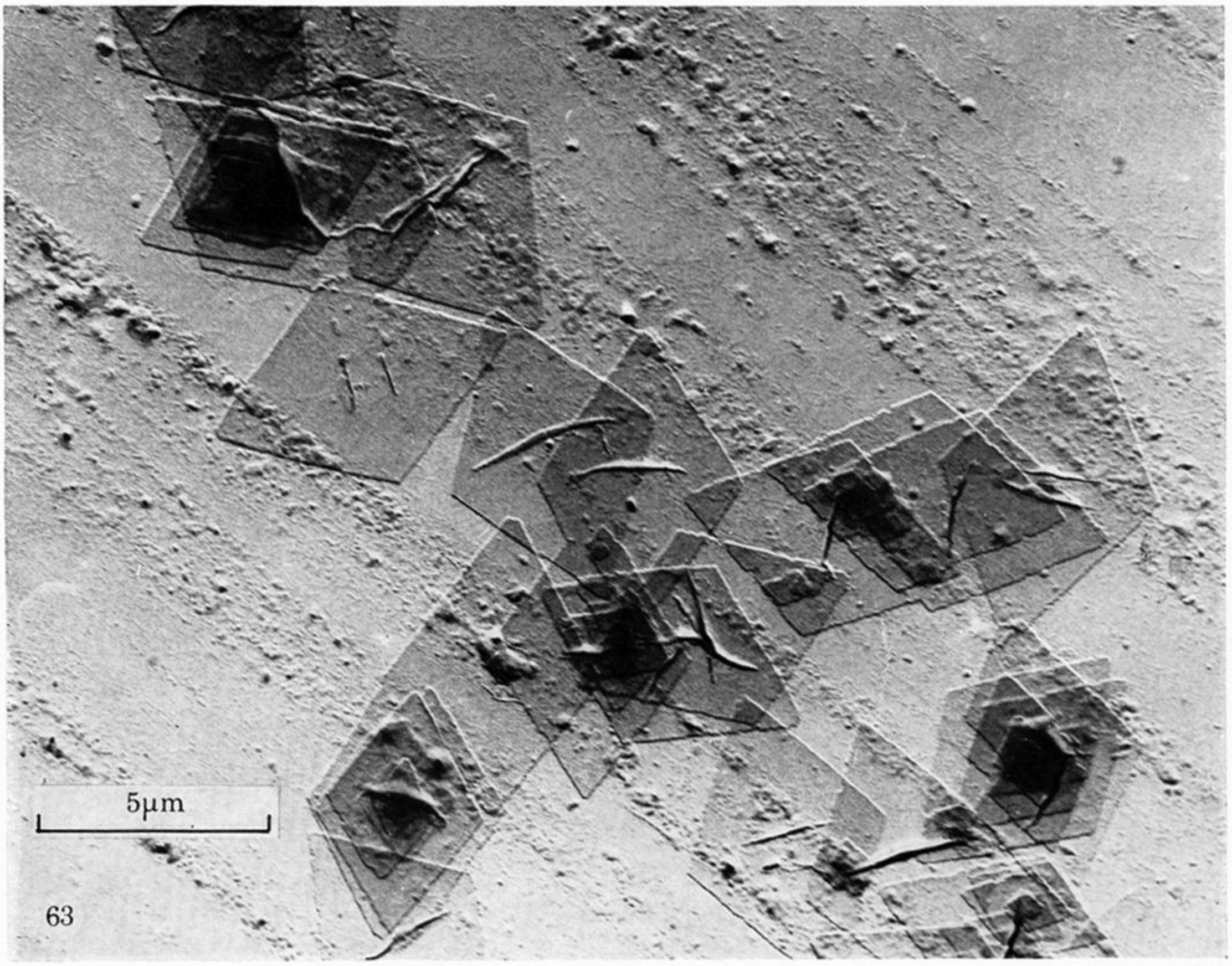

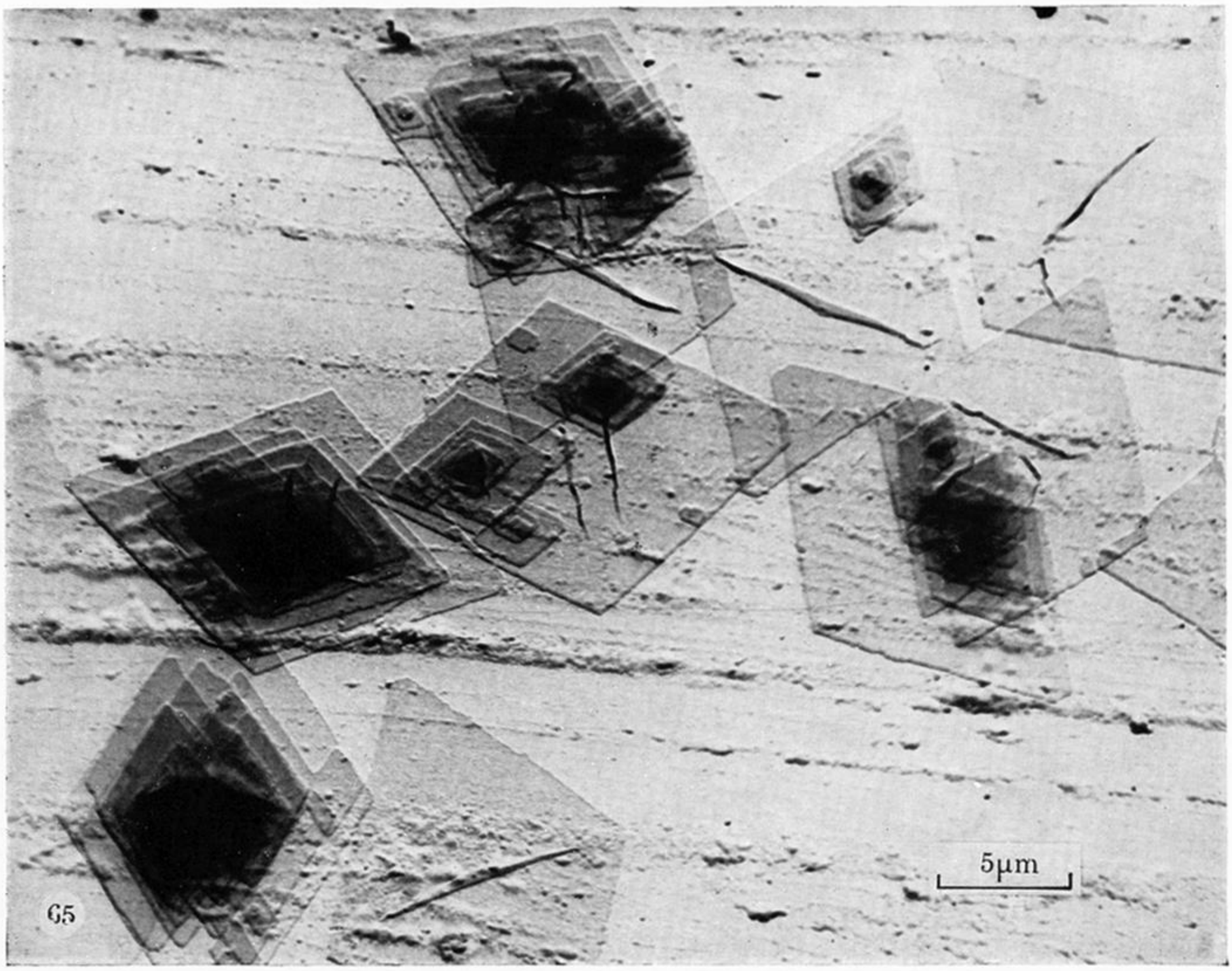

FIGURE 63. Electron micrograph of seeded single crystals; T_c = 100 °C.

FIGURE 65. Electron micrograph of seeded single crystals; T_c = 100 °C. Starting solution had been degraded for 2 h without antioxidant.

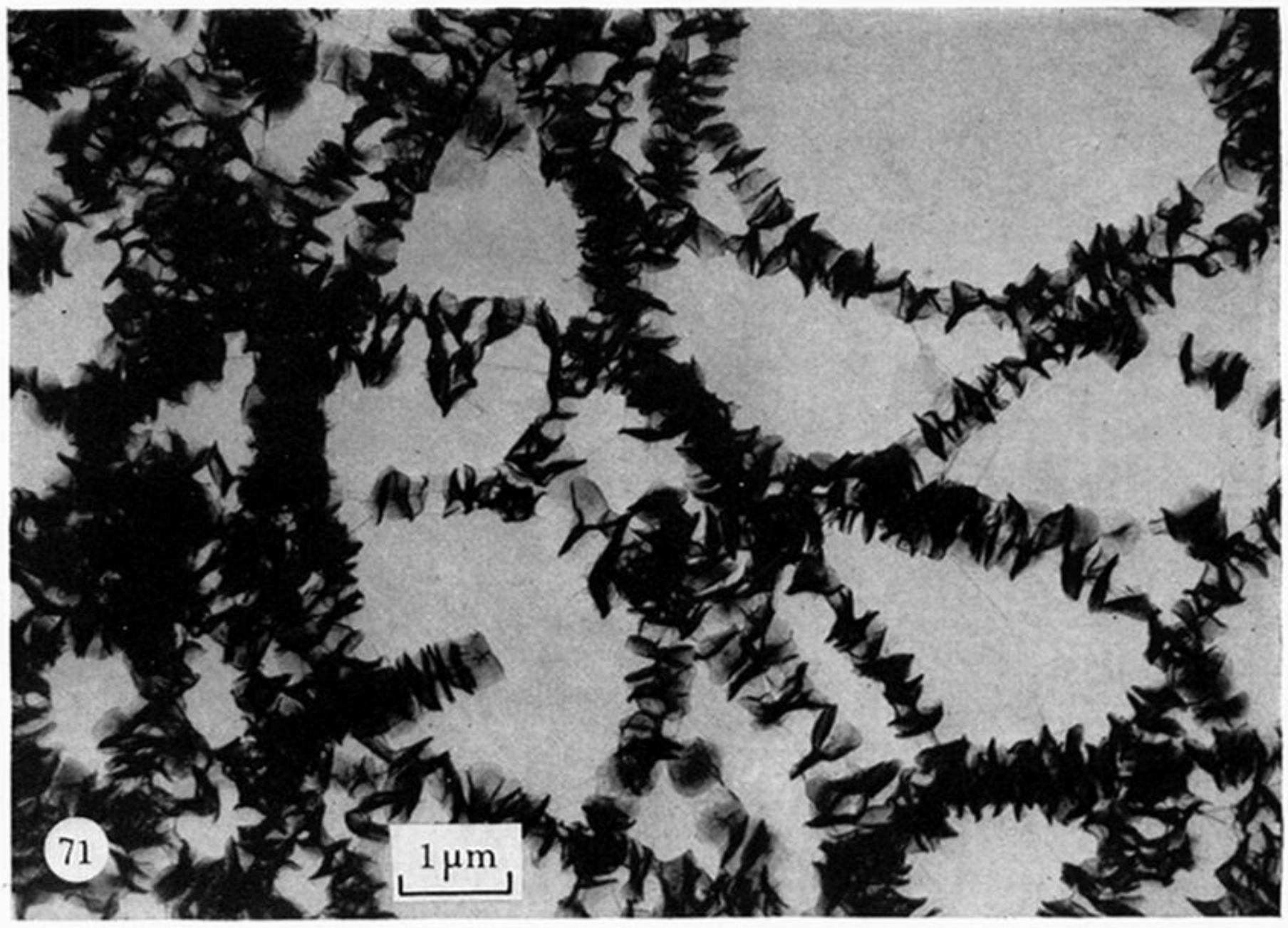

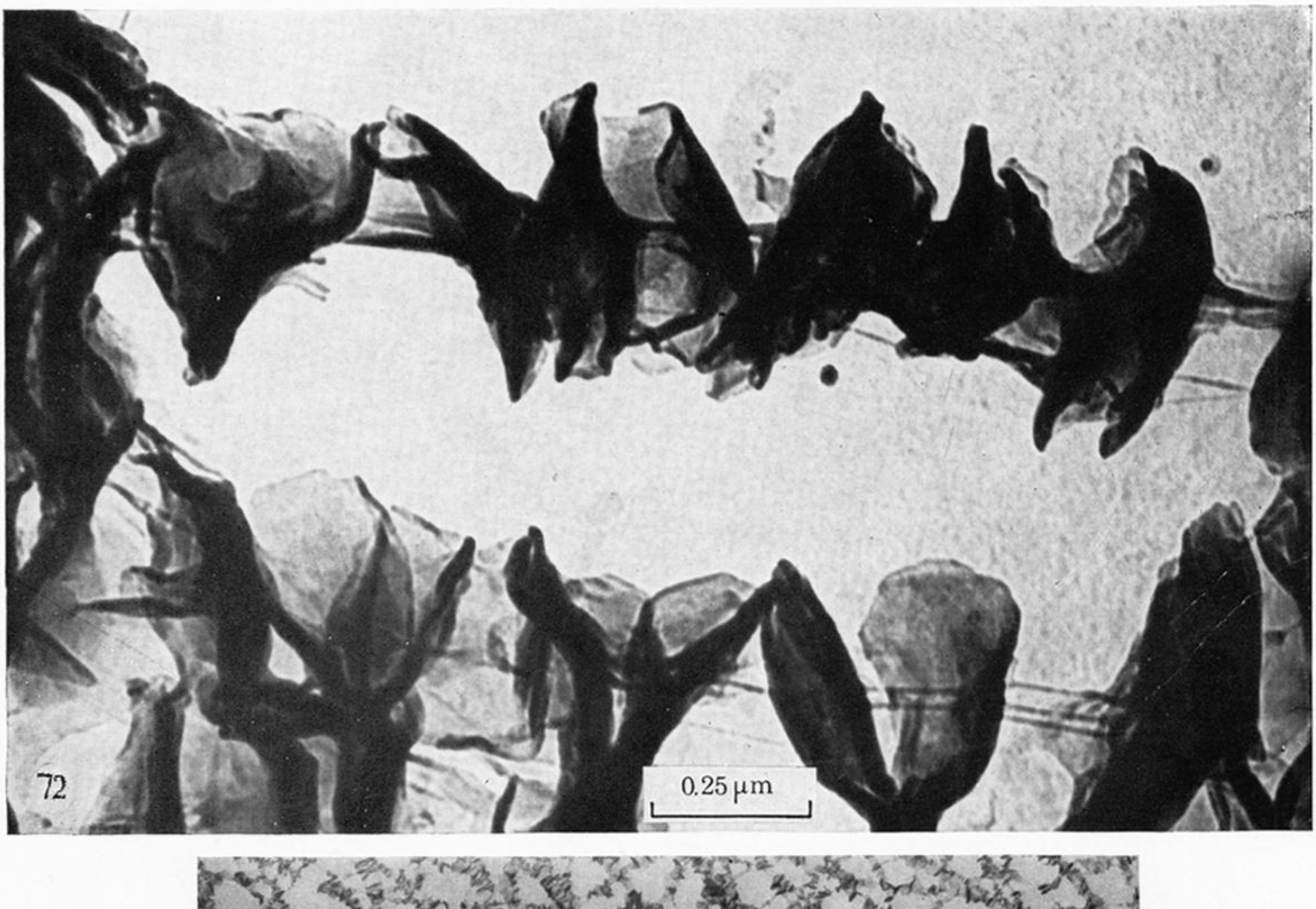

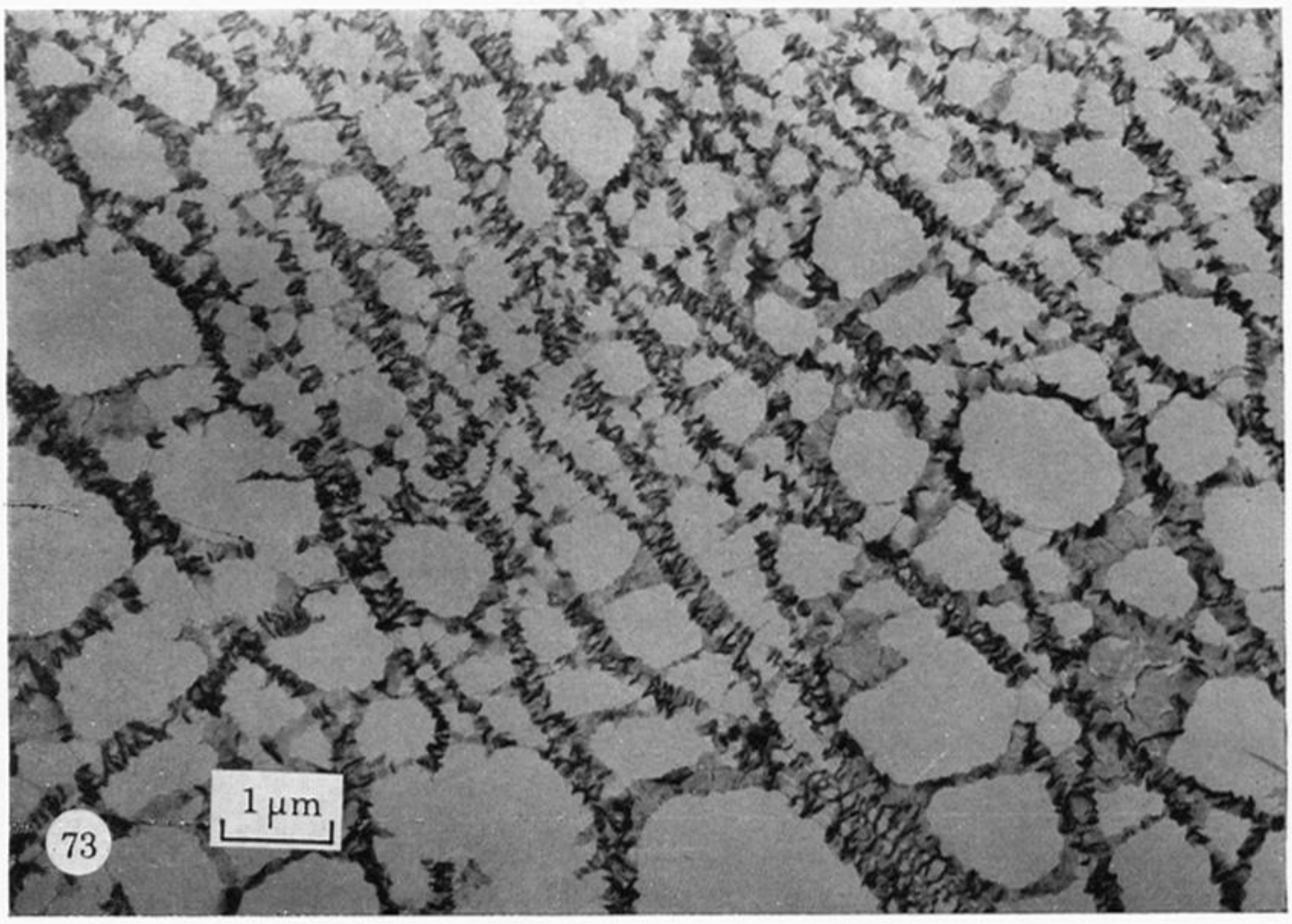

FIGURES 71–73. For description see opposite.

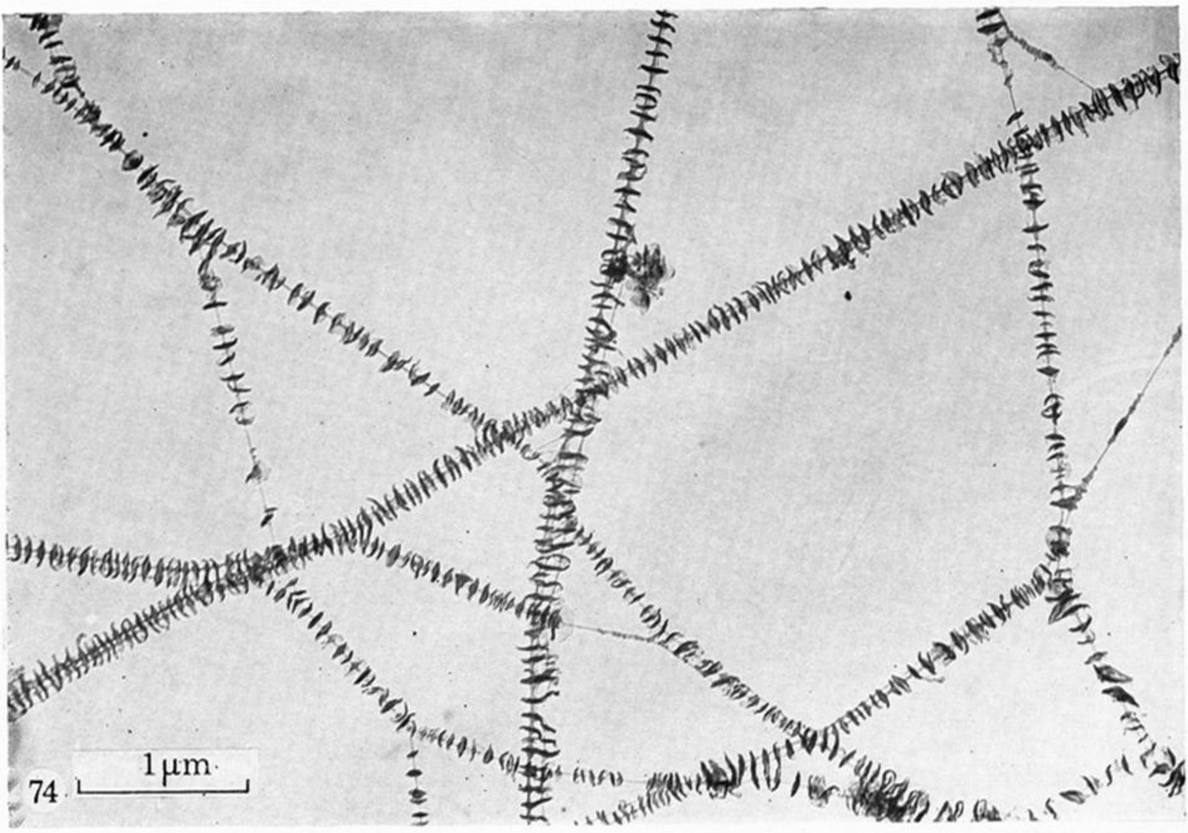

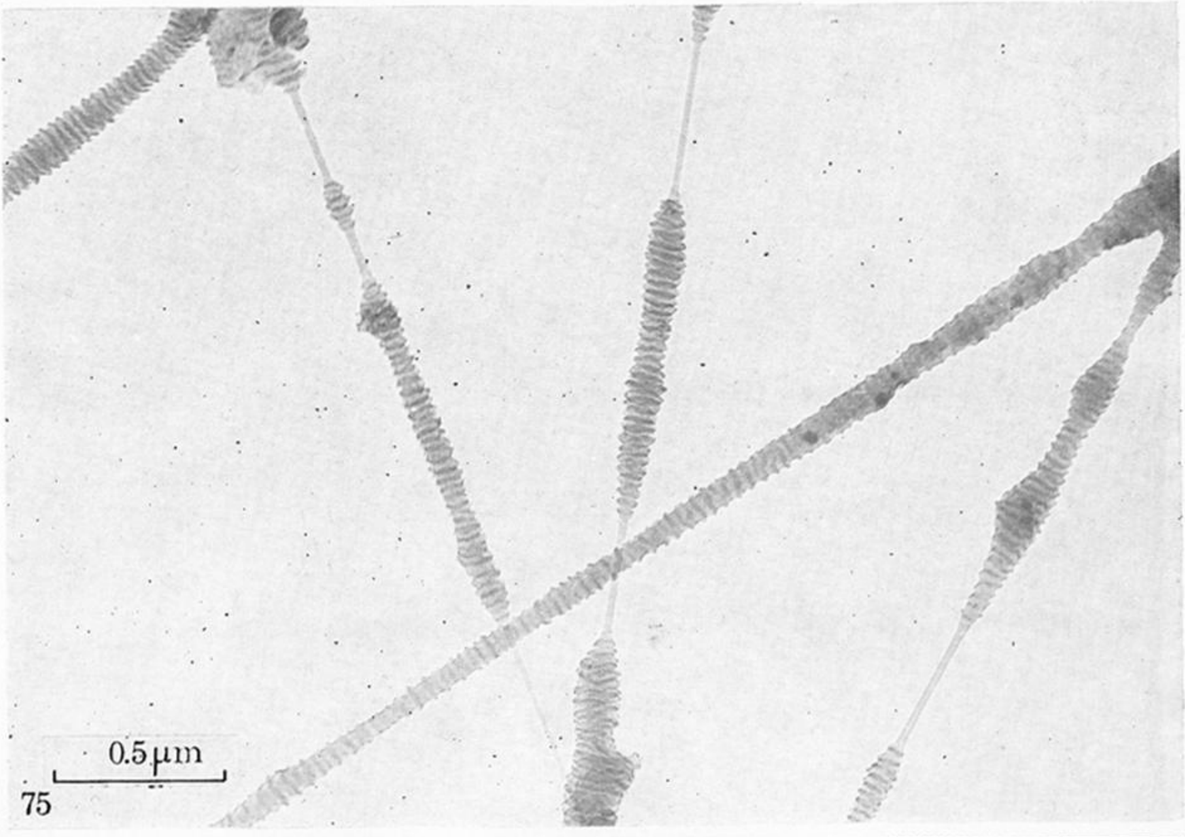

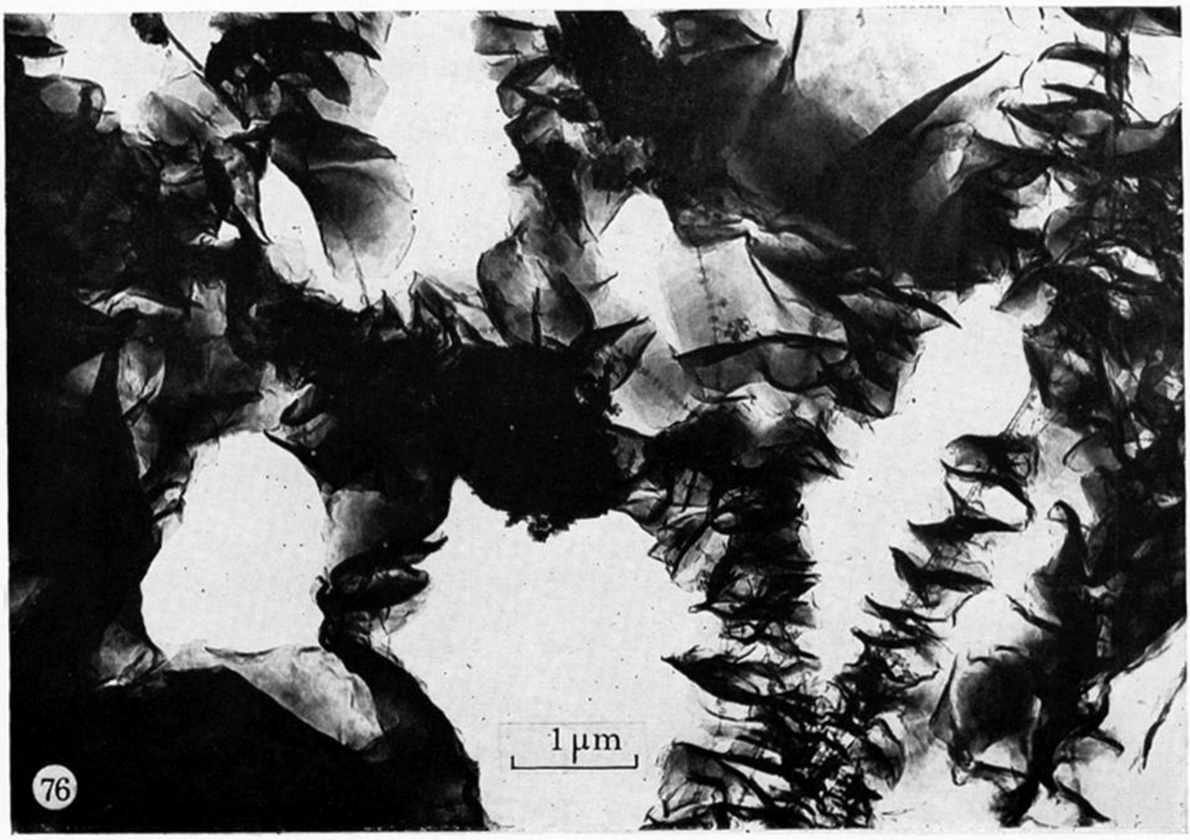

FIGURES 74–76. For description see opposite.